Tailor Synthesis of 0D, 1D and 2D

Transition Metal Dichalcogenide

Nanostructures

Dissertation
zur Erlangung des Grades
“Doktor der Naturwissenschaften”
im Promotionsfach Chemie

am Fachbereich Chemie, Pharmazie und Geowissenschaften
der Johannes-Gutenberg-Universität Mainz

vorgelegt von

Faegheh Hoshyargar, M. Sc.

geb. in Teheran, Iran

Mainz, 2012

ABSTRACT

The work presented in this doctoral thesis is a compilation of different approaches on the synthesis of transition metal dichalcogenides (TMDs) and the discussion on their probable formation mechanism. As the first step, a combination of metal organic chemical vapor deposition and chemical vapor transport approaches was taken to synthesize MoS_2 nanotube bundles and iodine was used as a mineralizing agent. The reaction was carried out in a horizontal tube furnace. In the absence of iodine, no nanotubes were formed. Therefore, it is demonstrated that the iodine content of the precursors led to the enhanced mobility of the Mo and S constituents, the formation of point defects within the MoS_2 layers and finally scrolling of MoS_2 nanosheets.

This synthetic method was further extended to synthesize WS_2 nested fullerenes and the formation of core-shell 2H-WS_2@IF-WS_2. Intermediate nanoparticles were studied using different electron microscopy techniques. The internal volume of the nested fullerenes was studied using a combined scanning electron microscopy/focused ion beam technique by cutting the cross sections of the core-shell nanoparticles. The lamellar reaction intermediates were found occluded in the fullerene particles. The role of the reaction and annealing temperature on the composition and morphology of the final product were also investigated. The stiffness of the WS_2 shell was measured using intermittent contact-mode AFM.

In addition, a facile route for the synthesis of WS_2 nanotubes starting from solvothermally derived tungsten oxide nanowires was demonstrated. Defect-rich multiwalled WS_2 nanotubes were made by reductive sulfidization of $W_{18}O_{49}$ nanowires that were obtained solvothermally from WCl_6 in different alcohols. $W_{18}O_{49}$ nanowires were also synthesized using a hot injection method, but these nanowires failed to form WS_2 nanotubes. The defect-rich nanotubes were highly dispersible in organic solvents and were easily functionalized by Au, MnO and Pt@Fe_3O_4 Janus nanoparticles on the basis of Pearson's HSAB principle which proved the direct transfer of defects from the precursor to the end product.

In order to investigate whether the preservation of the morphology applies for any other structures rather than 0D and 1D precursors, the oxide to sulfide conversion method was utilized to convert WO_3 low aspect ratio nanorods to corresponding sulfides. In this case, nested tungsten sulfide geometrical nanoparticles with 90° apex described as "nanocoffins" were obtained and the automated diffraction tomography was used to investigate the effect of the oxide precursor crystal structure on the final morphology of the sulfide product. The box-like morphology was shown to originate through topotactival dehydration reaction of the precursor, i.e. a $WO_3 \cdot {}^1/_3H_2O$ crust on WO_3, followed by epitactic induction of intermediate hexagonal WO_3 which serves as a template to maintain the particle shape in final product. In fact, a cascade of topotactic reaction leading to epitactic induction leads to the formation of closed rectangular boxes made from hexagonal layers.

As a step further, a lithiation/exfoliation approach was taken to synthesize a new class of TMDs in 2D form. Here, the restriction of convenient layered chalcogenide nanoparticles toward the intercalation was overwhelmed by selecting $Nb_{1-x}W_xS_2$ coin-roll nanowires (CRNWs) as appropriate intercalation host. CRNWs were intercalated using n-BuLi in an inert atmosphere and the exfoliation of the Li-intercalated CRNWs using H_2O led to the formation of graphene-type sheets of $Nb_{1-x}W_xS_2$. It was demonstrated that the *in situ* functionalization of the graphene-type sheets using gold nanoparticles enhanced the stabilization of these sheets in the aquatic solution.

TABLE OF CONTENTS

INTRODUCTION

1.1. Overview

The development of novel materials is a fundamental focal point of chemical research; and this interest is mandated by advancements in all areas of industry and technology.

The ability to visualize and manipulate structures with dimensions that are on the order of nanometers, or billionths of a meter, forms the basis of the field of nanotechnology, a world of miniaturization that has long captured the scientific imagination (Figure 1-1). One of the foremost visionaries in nanotechnology was American physicist and Nobelist Richard P. Feynman. As a researcher entering the nanoscience arena anyone should read Feynman's 1959 "*There's Plenty of Room at the Bottom*" speech [1], in which he presented an extraordinary vision of what could be done with extreme miniaturization.

With the development of the scanning tunneling microscope in 1981 by Gerd Binnig and Heinrich Rohrer, who received the 1986 Nobel Prize for Physics for their work, scientists finally had the power to image individual atoms on the surfaces of conducting or semiconducting materials. Numerous observations of nanoscale phenomena followed, including the 1985 discovery by Robert F. Curl, Harold W. Kroto, and Richard E. Smalley of nanometer-sized carbon structures known as fullerenes [2]. This discovery, which resulted in the 1996 Nobel Prize for Physics, opened a new chapter in nanotechnology, particularly because of the potential applications for fullerenes in electronics, materials science, and even medicine.

Despite the continued advances in nanoscience, much remains to be understood about nanomaterials and their behavior. Of notable concern in the manufacture of nanosized entities is the ability to control their atomic structure. But improvements in technologies and tools used in nanomaterial assembly have enabled the production of nanoscale products and product prototypes, such as electronic, magnetic, and mechanical nanoscale devices. Nanocoatings that render surfaces resistant to corrosion and nanoparticles with applications in medicine (e.g. drug delivery) and environmental remediation have also been developed or investigated. The current applications of nanotechnology and its speculating impact on the future have been widely outlined [3-5] and the impact of nanotechnology in fields ranging from automotive technology [6] to medicine [7-9] to earth science [10] to chemistry [11-13] are also hypothesized.

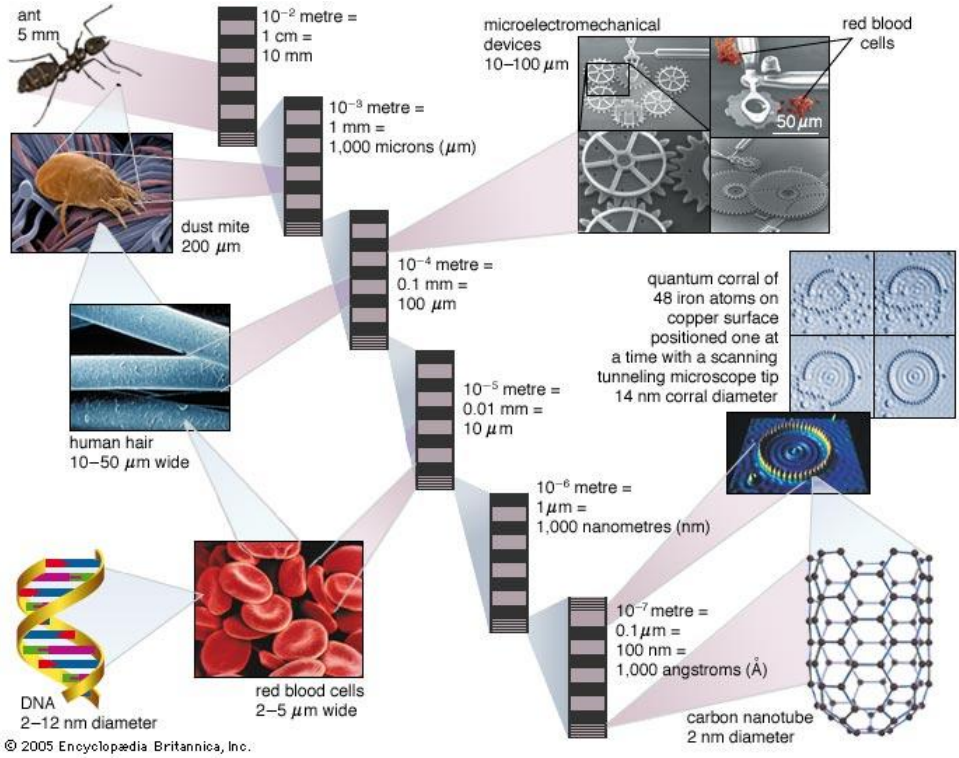

Figure 1-1. A comparison between natural and artificial structures from micrometer to nanometer dimensions.

1.2. Carbon Nanostructures

Nanomaterials is a new field of material science devoted to the study of materials with at least one dimension in the nanometer scale [14]. At this scale, qualitative changes in physicochemical properties and reactivity are connected to the number of atoms or molecules forming the material. For instance, size-effect properties can be observed, such as surface plasmon resonance in metal nanoparticles, quantum confinement in semiconductor particles and superparamagnetism in magnetic nanomaterials.

If only one dimension is restricted, we will have a layered shape or **2D material**; if two dimensions are limited in size, we will have a wire or **1D material**; if all dimensions are in the range of a few nanometres we usually talk of **0D materials**.

Therefore, it is not only size but also dimensionality that is one of the most defining parameters when determining material properties. This particularly applies to the case of sp^2 carbon materials (Figure 1-2), where 0D fullerenes, 1D nanotubes, 2D graphene and 3D graphite exhibit very different properties. The discovery of fullerenes greatly expanded the number of known carbon allotropes and furthermore suggested the existence of its 1D form, carbon nanotubes, first demonstrated in 1991 [15]. Although the theoretical studies of

graphite, fullerenes and nanotubes were performed using a single layer of graphite as starting material, a monolayer graphene sheet was isolated for the first time in 2004 [16]. Two dimensional materials are anticipated to have a significant impact on a large variety of applications, such as electronics, gas separation or storage, catalysis, high performance sensors, support membranes and inert coatings, just to mention a few of them.

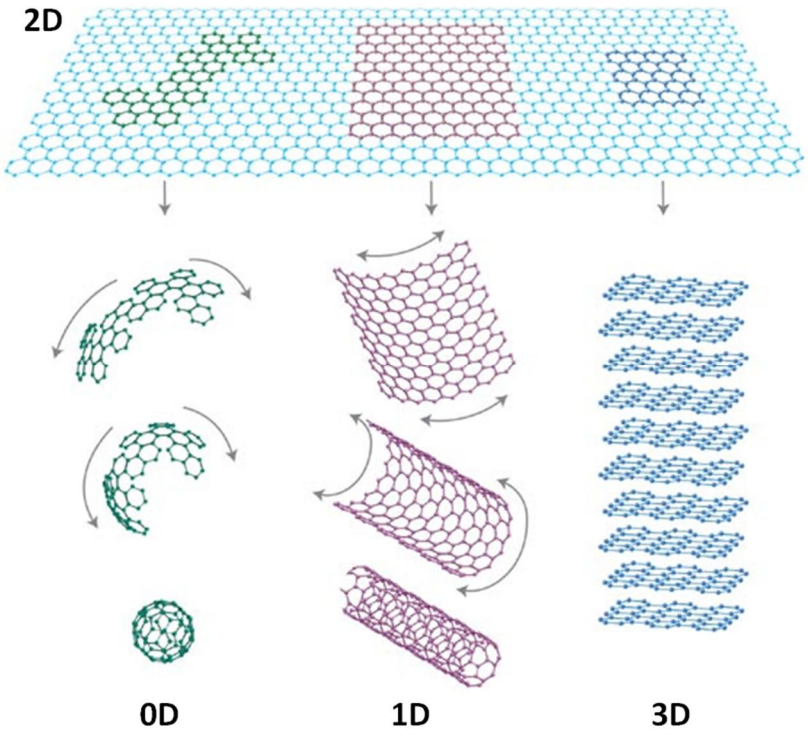

Figure 1-2. Graphene can be envisaged as a 2D material for carbon materials among all other dimensionalities. It can be wrapped up into 0D buckyballs, rolled into 1D nanotube or stacked into 3D graphite [104].

1.3. Transition Metal Dichalcogenide (TMD) Nanostructures

1.3.1. Inorganic Nanotubes (INTs) and Fullerene-like Nanoparticles (IFs)

Following the discovery of carbon nanotubes, nanostructured materials and their syntheses have attracted tremendous attention due to their superior mechanical and electronic properties and therefore, their high potential in making advanced nanodevices. Along with carbon nanotubes, many non-carbon nanostructures have been synthesized during the past few years. Due to their remarkable geometry and promising physical properties, the study of inorganic layered chalcogenide nanostructures has become one of the key topics in nanoscale research since the first report on WS_2 fullerenes by Tenne *et al.* in 1992 [17]. Various approaches to

other nanotubes, such as $NiCl_2$ [18], VS_2 [19], TiS_2 [20], and InS [21] have also been reported, which implies that many layer compounds may form fullerenes or nanotubes under favorable conditions.

Similar as their carbon congeners chalcogenide nanoparticles are not equilibrium but high-temperature and low-pressure phases that are obtained by quenching ‘‘hot’’ gas phase species. However, the synthesis of chalcogenide nanotubes and fullerenes (inorganic fullerenes, IF) is, in contrast to carbon, difficult owing to their wall thickness of three atom layers; considerable strain energy is required to achieve surface curvature [22]. Layered chalcogenides (MQ_2, M= Mo, W, Re, or Sn, Q= S, Se) are triple-layer structures in which one metal layer is sandwiched between two chalcogen layers with the metal in a trigonal pyramidal or octahedral coordination. The MQ_2 layers are stacked along the c-direction in an ABAB fashion (Figure 1-3) [23]. In contrast to carbon nanotubes no catalyst aids in their formation. The formation of curved MQ_2 morphologies commonly involves a considerable number of lattice defects and dislocations [24]. Since the first observation of single nanotubes, significant progress has been made, and today gram quantities of some metal chalcogenide nanotubes can be obtained in pure form.

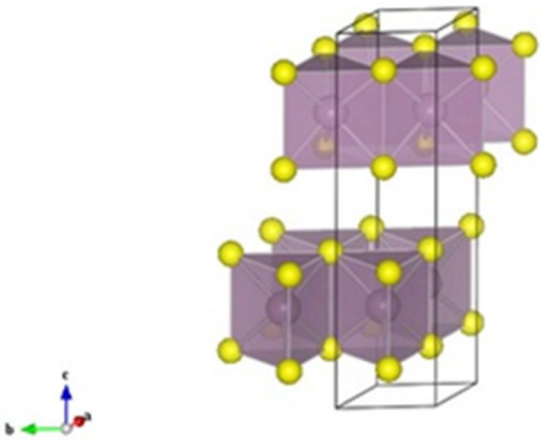

Figure 1-3. Layered structure of MoS_2 showing the unit cell and the triangular prisms where ABABAB packing is easy to spot.

1.4. Properties of Inorganic Nanotubes and Fullerene-like Nanoparticles

1.4.1. Thermodynamic and Topological Considerations

The formation mechanism of nested chalcogenide onions is still very poorly understood. Very early it was recognized that rhombi rather than pentagonal rings, which occur in carbon

fullerenes and nanotubes, are the building blocks in polyhedra of layered compounds [25]. The novel synthetic routes for hollow nanostructures such as high flux and far from equilibrium enlightened a number of unhandled issues, such as the smallest hollow MoS_2 nanoparticles. In order to clarify such complicated issues, a number of techniques such as laser ablation of MoS_2 targets, electron microscopy and *ab initio* calculations are combined. The density functional tight binding studies coupled with molecular dynamics (DFTB–MD) allowed a direct comparison with experimental data. Although the edges and corners of stable $Mo_{576}S_{1140}$ octahedron obtained by DFTB calculations at 0 K became distorted (based on a MD simulation at 300 K), it is noteworthy that the nanooctahedron's overall structure remained preserved. It is shown that these calculations could be extended to any size with a few simplifications, and the phase stability could be compared with that of MoS_2 nanoparticles with different morphologies. The similarity between experimental HRTEM data and the calculated images credits the theoretical analysis (Figure 1-4).

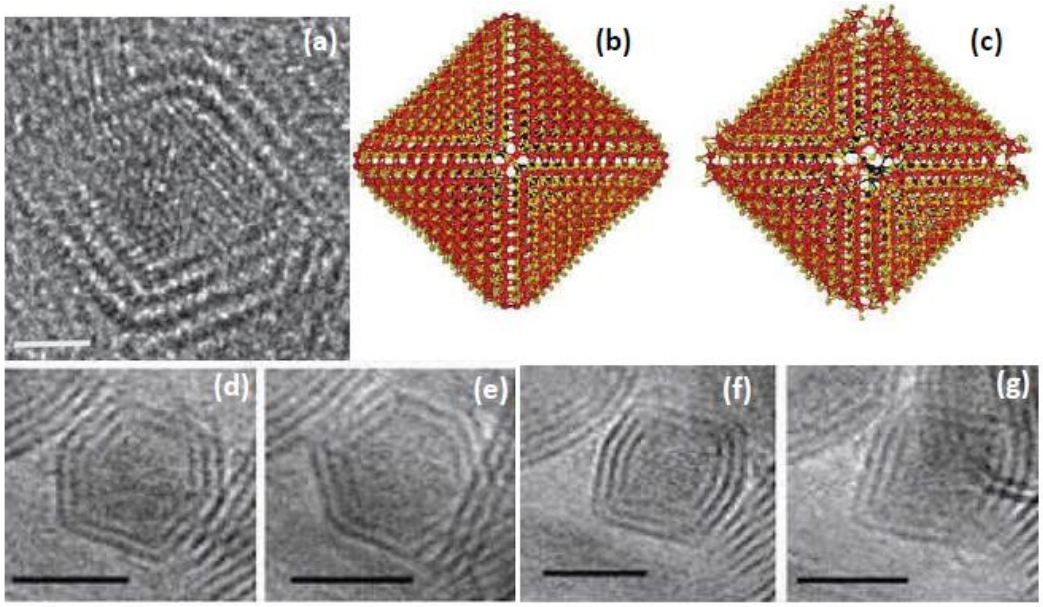

Figure 1-4. Hollow nano-octahedra, 3–6 nm in size and 2–5 layers thick were found in laser ablated samples of MoS_2. A typical HRTEM micrograph of an octahedral MoS_2 nanoparticle (a). The distance between each MoS_2 layer is 0.61 nm. A $Mo_{576}S_{1140}$ octahedron calculated from first principles using a density-functional tight-binding (DFTB) algorithm at 0 K (b) and after molecular dynamic (MD) simulation at 300 K (c). The starting model was $(MoS_2)_{576}$ (corner to corner distance of 3.8 nm), which relaxed by losing two sulfur atoms per corner (12 in total). (d-g). A TEM image of a three-layered nano-octahedron at tilt angles of 10, 20, 0 and -10º respectively [26].

As shown in Figure 1-5, the phase behavior of Mo and S in nano regime, which stated the origin of bulk MoS_2 from the elements, once clarified the phase behavior of small Mo–S clusters. It was clearly determined that below a few hundred atoms, the trigonal prismatic Mo–S bond is unstable. Rather clusters of the type Mo_4S_6 and Mo_6S_8 made of inner Mo polyhedra and surrounded by sulfur polyhedra are stable below ca. 100 atoms. Multiwall MoS_2 nanooctahedra, made of six symmetrically disposed rhombi (and two missing sulfur atoms) in the corners become stable between 10^3–10^5 atoms (3–7 nm in size) and are indeed the smallest hollow closed structures, *i.e.* the true MoS_2 fullerenes [27-29].
Further than this size and probably up to about 10^7 atoms (ca. 20–200 nm), the nanotubes (INT) and fullerene-like (IF) MoS_2 nanoparticles become stable. Bulk 2H-MoS_2 platelets become the most stable species at still larger sizes (>0.3 micron).

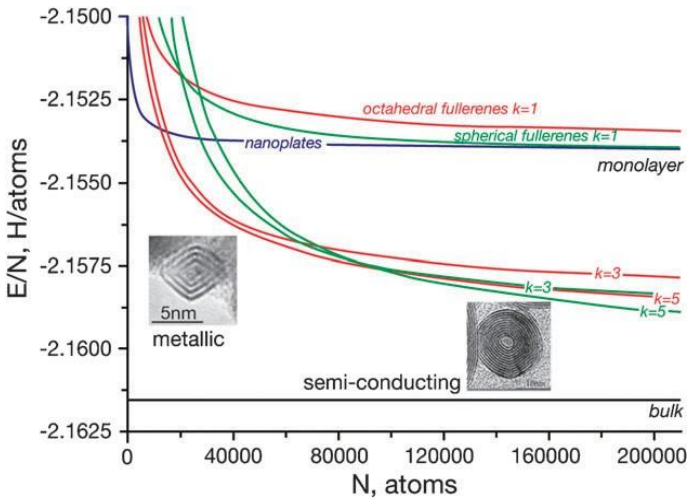

Figure 1-5. The dependence of the energy per atom E_t/N on the total number of atoms N for various MoS_2 nanostructures: triangular nanoplatelets (blue); octahedral fullerenes with k shells (red), and spherical fullerene-like nanoparticles (green) with k shells [28].

The strain energy/atom varies usually as $1 / R^2$, where R is the radius of the nanotube. For a given diameter, the strain in MoS_2 nanotubes is about one order of magnitude larger than that for carbon nanotubes (see Figure 1-6). Normally, the strain effects promotes the formation of MoS_2 nanotubes in larger diameter (>15 nm) as compared with carbon nanotubes (typically 1.5 nm). Moreover, it has been shown that the van der Waals interaction between the molecular sheets enhances the stability of multiwall (5–10 layers) nanotubes.

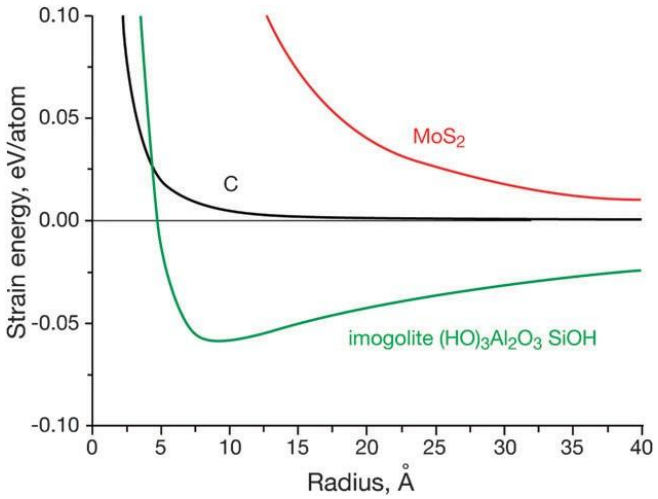

Figure 1-6. Graph showing the calculated elastic energy/atom as a function of (zig-zag) nanotube diameter for carbon, MoS_2 and imogolite nanotubes.

The main conclusions from that combined theoretical–experimental study are:

(i) the nanooctahedra are stable over a limited range of about 5000–100000 atoms (3–6 nm). Below this size, MoS_2 nanoplatelets are more stable, whereas quasispherical closed cage (fullerene-like) nanoparticles become the most stable species above the higher limit. At even larger sizes (approximately 107 atoms) macroscopic MoS_2 platelets become the most stable structure.

(ii) among the possible stable nanooctahedra structures those with the formula Mo_nS_{2n-12} are the most stable.

(iii) whereas MoS_2 platelets and the quasi-spherical nested structures are semiconductors, the nanooctahedra are metallic. This seems to be related to the enhanced density of states at the rim of the facets [30].

1.4.2. Mechanical Properties

The mechanical properties of inorganic nanotubes have been shown to be remarkably different from the bulk materials. The mechanical behavior of bulk materials is dictated by the nature of the chemical bond holding the atoms together as well as structural and chemical defects. Intrinsic defects, like vacancies, interstitial or antisites, are dictated by the thermodynamics of finite temperature systems whereas extrinsic defects, such as grain boundaries and dislocations, are induced by the processing of the material. Therefore, most bulk materials are appreciably weaker than what would be predicted by considering the strength of their respective chemical bonds.

In comparison, a series of experiments with individual multiwall WS_2 nanotubes [31] have pointed out that their mechanical properties are predictable from first principle calculations, *i.e.* they can be referred to the strength of the chemical bond. Figure 1-7 shows a snapshot taken during a tensile test of an individual WS_2 nanotube along with the stress–strain curve of this nanotube. The nanotube showed elastic (linear) behavior almost to failure. The Young's modulus calculated from the slope of the curve; strength and strain at yielding are 160 GPa, 17 and 10%, respectively. Nearly the half of the measured nanotubes showed strength in excess of 13 GPa showing that they are basically free of critical defects. DFTB calculations of single-wall MoS_2 nanotubes were carried out and were compared to the experimental data of WS_2 nanotubes. The calculated data (after normalization from MoS_2 to WS_2) was about 30% higher than the experimentally observed strength and strain to failure. Furthermore, the theoretical calculations clearly show that under extreme strain one of the Mo–S bonds in the middle of the nanotube fails, which leads to stress concentration on the neighboring bonds and to their rapid failure. This mode of failure does not involve any intrinsic or extrinsic defect.

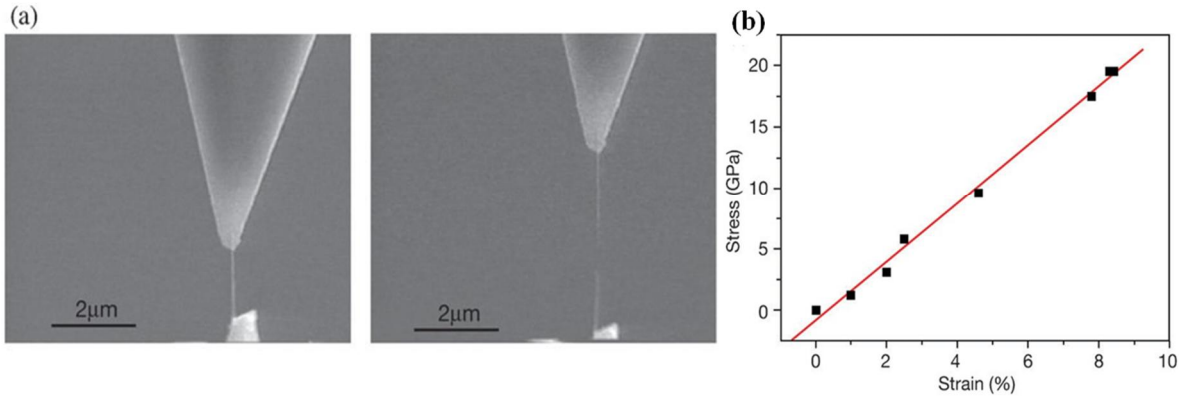

Figure 1-7. (a) SEM images of a WS_2 nanotube during a tensile test before (left) and after (right) failure; (b) Strain–stress curve of such a nanotube [31].

The bending test was also performed on individual WS_2 nanotubes [32], by suspending the nanotube on an empty channel and pushing them sideways in the middle. The sliding of one nanotube layer with respect to its neighbors could be calculated from the modified Timoshenko's bending equation. In bulk materials the ratio between the Young's (E) and shear (G) moduli is high (about 0.3). Consequently the contribution of the shear mode to the bending energy is rather small. The relatively free sliding, *i.e.* the low sliding modulus ($G/E \sim 0.01$) of neighboring walls with respect to each other in the nanotube, allows this mode to take a relatively significant share (>10%) of the bending energy. These magnificent properties together with the advent of the large-scale synthesis of WS_2 fullerene-like

nanoparticles and nanotubes [33] lead to development of IF- and INT-based ultra-high strength nanocomposites.

1.4.3. Optical Behavior

Recently, resonance Raman (λ_{exc} = 632.8 nm) spectra of individual MoS_2 and WS_2 nanotubes were measured and compared to the bulk materials [34]. For both the original A_{1g} (408, 421 cm^{-1}) and E^1_{2g} (383, 356 cm^{-1}) Raman modes an up-shift of the peaks (3–10 cm^{-1}) was observed which was attributed to the built-in strain in the nanotubes. Indeed, collapsed MoS_2 nanotubes (ribbons) showed no such shift. Furthermore, electron diffraction analysis showed that locally the nanotubes crystallized in the high-pressure rhombohedral (3R) symmetry rather than the hexagonal symmetry, which is the stable polymorph in ambient conditions. The Raman lines of core–shell W/IF-WS_2 nanoparticles were studied as a function of the hydrostatic pressure in a diamond anvil cell [35]. The A_{1g} line at 420 cm^{-1} was shown to contain a new low-energy shoulder at 416 cm^{-1} due to two-phonon coupling originating from longitudinal acoustic (LA) and transverse acoustic (TA) phonons at the K-point of the Brillouin zone. This low energy shoulder is enhanced by the curvature of the nanoparticles. The Raman spectra of the core–shell W/IF-WS_2 nanoparticles under different pressures are shown in Figure 1-8. The intensity ratio of the LA + TA and A1g modes varies clearly with increasing pressure. This ratio first increases and then reaches a maximum and decreases with the application of a higher pressure. Upon releasing the pressure, the original lineshape is restored indicating that the nanotubes are stable under hydrostatic pressure of up to 18 GPa and could therefore serve to reinforce ultra-high strength nanocomposites.

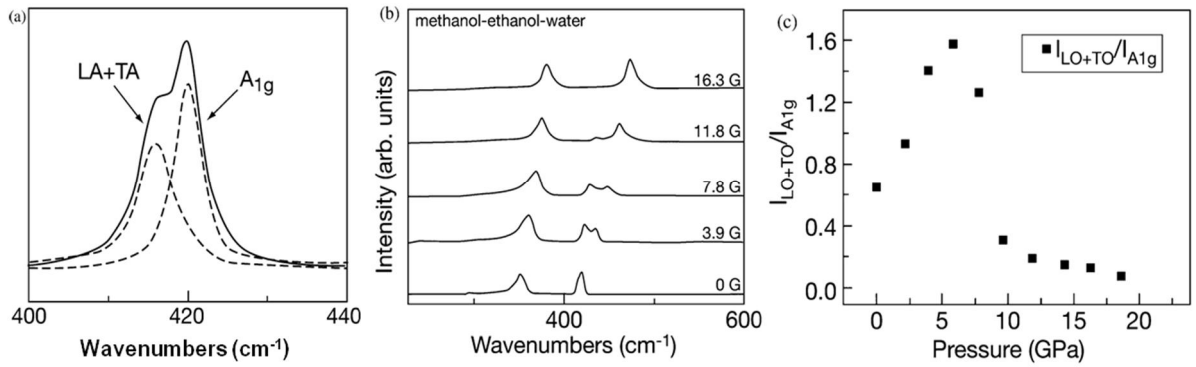

Figure 1-8. (a and b) the evolution of the Raman spectrum of IF-MoS_2 nanoparticles under pressure; (c) Intensity ratio of the LA + TA/A_{1g} peaks [35].

1.4.4. Electronic Structure and Transport

A phototransistor based on individual WS_2 nanotubes, which is sensitive to visible light was recently fabricated and tested [36].The maximal sensitivity of the phototransistor was obtained when the visible light for a halogen lamp was polarized in parallel to the nanotube axis and the minimum sensitivity occurred when the light was polarized perpendicular to the nanotube axis. The carrier mobility and carrier density increased from 4.1×10^{-4} and 1.54×10^{6} in the dark to 1.3×10^{-3} and 2.57×10^{7} V cm^2 s^{-1}, respectively, under illumination. Transistors capable of detecting visible light would have a wide range of applications in consumer and medical electronics.

1.4.5. Surface Modification of INTs and IFs

The embryonic stage of nanotechnology is atomic assembly whereas the mature form of nanotechnology will be molecular assembly to make nano-building blocks for the design of nanocomposites or self-organizing nanodevices. Tailoring of the surface chemical bonds might lead to an optimized interaction of the nanoparticles with solvent molecules, polymer matrices, or biomolecules. Moreover, the surface characteristics of nanomaterials influence the broad range of properties and the performance of a large variety of devices.

Surface modification of nanomaterials can be achieved by two methods: grafting of organic groups to surface of nanomaterials after synthesis (*post* functionalization) or in situ modification of nanomaterials by organic compounds (*in situ* functionalization).

In *post* functionalization, the strategy is attaching of certain bifunctional organic linkers to pre-synthesized nanoparticles and then linking of the nanoparticles to the nanomaterials [37-39]. An alternative strategy is to grow nanoparticles directly on the nanotubes by using colloidal nanoparticle synthesis methods [40-43]. This approach to functionalization preserves the electronic and structural integrity of nanotubes and nanoparticles and – due to the cooperative effect of hybrid materials – the efficiencies of devices may be enhanced.

In analogy to quantum dots and carbon nanotubes, the chemical modifications of IF and INT surfaces is a key step in affording stable suspensions of these nanoparticles and blending them in different polymers. The functional ligand consists of an anchor group that attaches to the nanoparticle surface and a tail which renders them soluble in various solvents. Also, the tethered molecules allow the nanoparticles to disperse well in polymer blends or oil suspensions. Tahir *et al.* used a nitrilotriacetic acid (NTA) group to chelate Ni^{3+} ions from above [44]. The partially empty coordination sites of the nickel ions were shown to bind to the outermost sulfur atoms on the surface of the IF (INT)-WS_2 nanoparticles. On its opposite side,

the NTA moiety was linked to a polymer [poly(pentafluorophenyl acrylate)] which terminates with polar groups such as catechol (1,2-dihydroxybenzene) (see Figure 1-9). Such surface-functionalized IF-WS_2 nanoparticles formed stable suspensions with water.

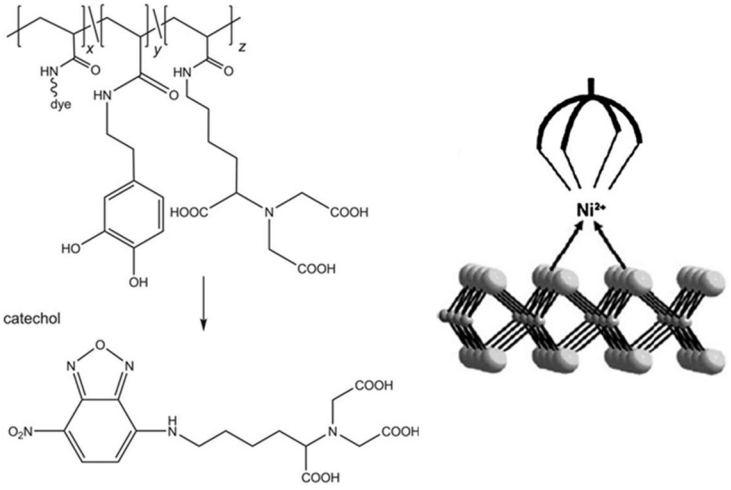

Figure 1-9. Synthesis of the fluorescent ligand containing nitrilotriacetic acid (NTA) and binding of the ligand to the WS_2 surface by complexion through the NTA group.

In a different vein, Sahoo *et al.* functionalized WS_2 nanotubes using Pt@Fe_3O_4 Janus nanoparticles on the basis of the Pearson HSAB (hard–soft acid–base) principle [45]. They demonstrated that the hierarchical assembly of Pt@Fe_3O_4 Janus particles on WS_2 nanotubes is dictated by the principles of Pearson's concept, that is, Pt is the preferred binding partner over Fe_3O_4. However, the preferential binding of Fe_3O_4 domains can be enhanced by protecting the Pt face of the Janus particle with an organic ligand (see Figure 1-10). The assembly of the Pt@Fe_3O_4 particles onto WS_2 nanotubes in $CHCl_3$ solution can be quantitatively controlled by varying the particle concentration below a critical value. They also showed that owing to the magnetism of the magnetite domain, Pt@Fe_3O_4/NT-WS_2 can be retrieved from solution with a permanent magnet.

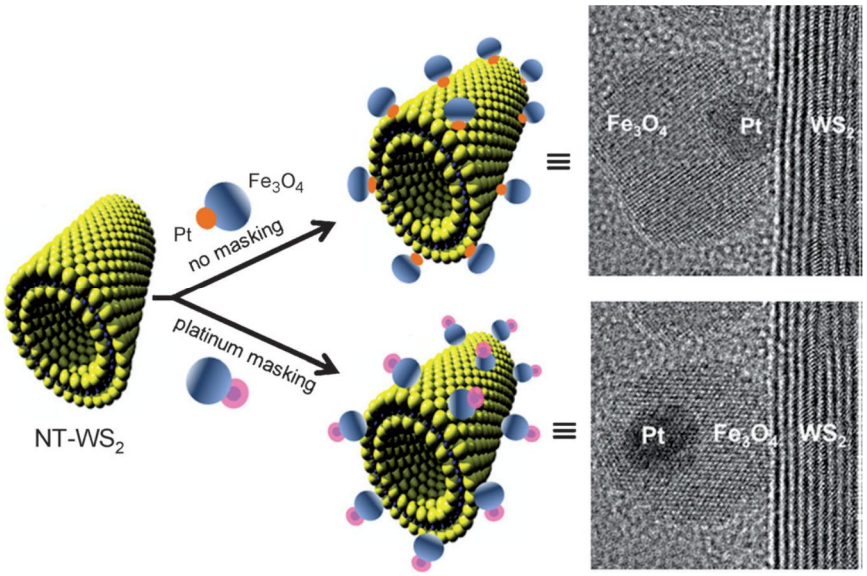

Figure 1-10. Customized binding of Pt@Fe_3O_4 Janus particles onto NT-WS_2 through their Pt and Fe_3O_4 faces.

1.5. Applications

Numerous applications have been demonstrated for the IF-MS_2 nanoparticles (M= Mo, W, Ti, Nb etc.), the most prominent applications being their use as solid lubricants, heterogeneous catalysts, super shock absorbers, or battery materials. The nanotubes and fullerenes of layered metal chalcogenides are akin to carbon nanotubes in that they exhibit analogous electronic properties but these nanomaterials find excellent mechanical properties related to their crystal structures which are characterized by weak van der Waals forces between the individual MQ_2 slabs containing metal atoms sandwiched between two inert chalcogen layers. The physical properties of inorganic nanotubes are still little explored. A composite made of layered metal chalcogenide fullerenes could withstand the shock pressure generated by the impacts of 250 tons per centimetre square. IsraCast has reported that these materials are the most shock-resistant materials known to man and is five times stronger than steel [46].

1.5.1. Tribology

While some potential applications of IF and INT have already been discussed for some time, commercial realization of IF-WS_2 as a solid lubricant only started during 2008. There are many issues remaining to be resolved in this context. First, it would be desirable to have the size of typical IF nanoparticles (currently >80 nm) as small as possible. The size of the nanoparticles is important for a number of reasons. First, smaller nanoparticles could make a

more homogenous and stable oil suspension; secondly, access into the contact area between the two metal pieces could become easier. Finally, the flow of the nanoparticles in the oil could become more homogenous, too, especially near the surfaces. However, given the built-in strain of the folded structures [47], it is not easy to foresee a simple solution to this issue. One way to accommodate the strain and reduce the size of the nanoparticles is by producing less than perfect nanoparticles which contain defects, especially in the corners where the strain is highest. However, introducing defects into the nanostructures may compromise their mechanical behavior and therefore their long-term durability. Another possible solution is to synthesize nanoparticles with smaller numbers (<10) of MS_2 layers. Since the elastic energy of folding depends on the thickness to the power of three, nanoparticles with fewer than 10 layers may have smaller (<50 nm) radii.

The agglomeration of the nanoparticles generally influences the tribological characteristics and the shelf-life of the suspensions. Recently, a number of synthetic procedures were proposed to minimize the agglomeration of the IF and INT. In one such strategy [48], alkyl silane groups were tethered to the IF-WS_2 nanoparticle surface, probably through surface defects which adsorb water molecules or OH groups. Although the coverage of the nanoparticles surface is less than half, it was clearly observed that the degree of agglomeration has been reduced from a mean size of about a thousand nanoparticles to two hundreds and fewer. The reduced agglomerate size favorably influenced the stability of oil suspensions and the long-term tribological behavior of oils formulated with these surface-functionalized IF nanoparticles. The surface-functionalized IF nanoparticles can be further manipulated in order to endow them with specific chemistries which will allow them to serve in, *e.g.* drug delivery, or photostimulated tumor therapy.

While numerous applications for the nanoparticles suspended in lubricating fluids have been proposed and some are already in use, a variety of other uses could be also envisaged. One such example is self-lubricating surfaces obtained by impregnating the IF nanoparticles into various coatings. Thus, electroless/electrodeposition coatings of metallic substrates with nickel–phosphorous and cobalt films impregnated with IF-WS_2 nanoparticles (see Figure 1-11) have been demonstrated [49,50]. Here a remarkable reduction in the friction coefficient, as compared to the pure metallic films, was observed. Unexpectedly, the IF nanoparticles seem to also play the role of cathodic protector on the film, by slowing down the oxidation of the topmost metallic layer during the tribological tests.

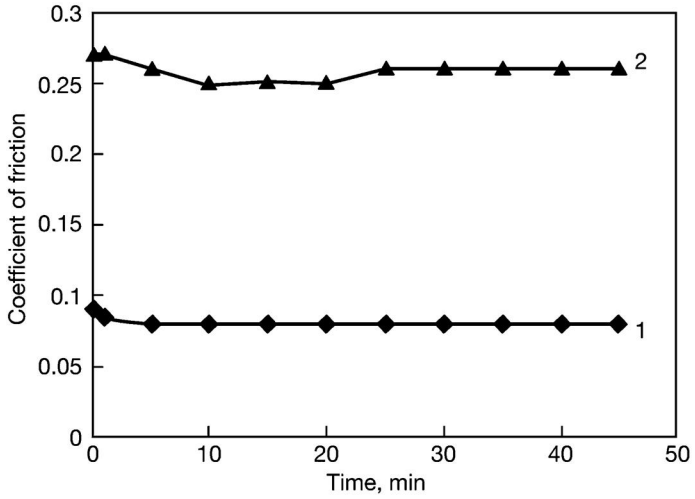

Figure 1-11. Comparison between the friction coefficient behaviors of NiTi foil coated with electrodeposited cobalt film impregnated with IF-WS_2 nanoparticles (1); and the bare NiTi substrate (2). The tribological tests were performed using a ball-on-flat set-up at a Hertzian pressure of 1.5 GPa and velocity of 0.2 mm s^{-1} [50].

The materials such as nickel titanium alloys and stainless steel are extensively used in various medical disciplines such as orthopedics, urology, dentistry, cardiovascular therapy etc. Orthodontics is a dental specialty that diagnoses, prevents and treats teeth which are not properly located in the jaws. This is done by application of a mechanical load (orthodontic force) on the teeth. This force affects the tissues surrounding the teeth, thereafter enabling their movement. Teeth movement is entirely regulated by nickel titanium or stainless steel wires.

The wires are inserted into brackets, which are bonded onto the teeth surface. Unfortunately, the friction between the wire and the bracket leads to the application of an excessive force (>50%). This situation leads to undesirable teeth movement; elongating the treatment period; irreversible shortening of the roots of the teeth (root resorption) all causing discomfort to the patients. IF coating of the orthodontic wires brought about a significant reduction of the mechanical force (see Table 1-1 [49]) required for moving the teeth. This approach is indeed not unique to orthodontic wires and recent efforts focused on a number of other medical technologies. One of the main concerns in the ongoing use of NiTi alloys for biomedical purposes is the fatigue behavior of the material.Considering the protective role of the IF nanoparticles impregnated into metallic films, it is likely that such coatings will increase the fatigue resistance of the NiTi devices.

Table 1-1. Testing of stainless-steel orthodontic wires inserted in a bracket in different angulations. Comparison between uncoated and wires coated with Ni–P film impregnated with IF-WS_2 nanoparticles.

Angle Coating	0º (N)	5º (N)	10º (N)
Uncoated wire	1.32 ± 0.12	2.95 ± 0.09	4.00 ± 0.19 dry 3.35 ± 0.21 wet
Ni-P + IF coated wire	1.10 ± 0.06	1.58 ± 0.25	1.85 ± 0.21 dry 1.57 ± 0.23 wet

Many tribological surfaces cannot be coated in wet processes, and vacuum-based techniques are desirable for these cases. The main difficulty in applying such techniques is that they should permit the pristine IF nanoparticles to be co-deposited on the underlying surface with as little damage as possible. In a recent work [51], IF nanoparticles were evaporated onto a substrate by using a cluster evaporation chamber and electromagnetic injector mounted into a magnetron sputtering set-up. Quite uniform films of TiN impregnated with IF-WS_2 nanoparticles were obtained using this technique, as well as films containing other nanoparticles. It is likely that in the future such technologies will be used to manufacture self-lubricating surfaces for a variety of applications in the aerospace; medical and automotive industries.

1.5.2. Nanocomposites

Blending of various nanoparticles in polymeric matrices has been studied for more than a decade. Later on, much work was focused on improving the electrical characteristics of polymer matrices. In particular, carbon nanotube nanocomposites have been studied very extensively for variety of applications. Similar studies were extended to IF-WS_2 nanoparticles and more recently INT-WS_2 once they became available in substantial quantities. The effect of minute amounts of IF-WS_2 nanoparticles on the thermal stability; crystallinity and the mechanical properties of variety of thermoplastic polymer nanocomposites have been reported [52,53].

For instance, it was demonstrated that adding a few percent IF-WS_2 nanoparticles to poly(propylene) had a remarkable effect on the thermal stability of the nanocomposite, *i.e.* 60 degrees increase in the initial degradation temperature of this polymer [53]. As another example, polyether–ether–ketone (PEEK), an important thermoplastic polymer, was formulated with IF-WS_2 nanoparticles [54]. The nanoparticles were shown to endow

enhanced mechanical and tribological behavior to this nanocomposite. Furthermore, addition of just 0.5 wt% of the nanoparticles to an epoxy resin (D.E.R. 331 with Versamide 140 as curing agent) brought about an almost factor of three enhancement in the peel and shear strength of the contact (see Figure 1-12) [55]. Clear evidence for the formation of C–O–S bonds between the epoxy resin and the outermost sulfide layer was obtained from IR measurements. The formation of this bond was responsible for crack-bowing and deflection which were clearly observed in the fractured surfaces of the nanocomposite.

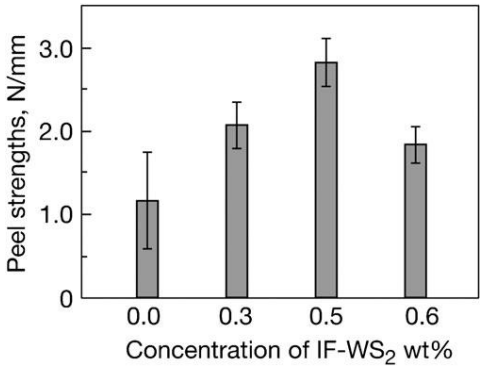

Figure 1-12. Peel strength of aluminum joints glued with epoxy resin formulated with different concentrations of IF-WS_2 nanoparticles [55].

1.5.3. Catalysis

There has been much discussion about the use of nanomaterials including IF and INT to mitigate the anthropogenic effects caused by human activity on the energy supply and its environmental impact. For instance, the catalytic effect of MoS_2 nanotubes on the hydrodesulfurization of oil is well known [56,57]. These nanoparticles, used in catalysis for the hydrodesulfurization of thiophene, were first obtained by reaction of $Mo(CO)_6$ with sulfur in an aprotic solvent using an ultrasonic probe and silica nanoparticles as a template and was removed by HF etching to result hollow nanoparticles of MoS_2. Although the nanoparticles were not well crystalline, they revealed high reactivity and selectivity toward the hydrodesulfurization of thiophene [58]. In another study, Ni nanoparticles were deposited onto a MoS_2 nanotube support. This nanocomposite was found to serve as a very potent and selective catalyst for the hydrodesulfurization of thiophene and a few of its derivatives. These few examples demonstrate the remarkable potential of inorganic nanotubes and fullerene-like nanoparticles in mitigating the environmental impact of sulfur rich gasoline and in green chemistry [59].

1.6. Synthesis Methods for TMDs

Concerning their high potential applications, various strategies have been developed to prepare nanostructured metal sulfides and selenides through different growth mechanisms. A characteristic feature of all closed-shell structures is that high reaction temperatures (>800ºC) or large activation energies are needed to overcome the activation barrier associated with the bending of the otherwise flat 2D layers [60]. Although various synthetic approaches to chalcogenide nanoparticles have been established so far, their growth mechanism is still subject to discussion. Tenne and co-workers were the first to show that fullerene-type nanoparticles or nanopolyhedra and nanotubes represent an integral part of the phase diagram of MoS_2 and WS_2 [17a]. In the following decade a variety of methods including

- arc discharge [61,62],
- sulfidization/selenization of metal oxides [63-73], chlorides [74,75] and carbonyls [76],
- decomposition of ammonium thiometalates [77-80],
- chemical vapor transport [81,82],
- laser ablation [83-86],
- microwave plasma [87,88],
- atmospheric pressure chemical vapor deposition (APCVD) [89], and
- spray pyrolysis [90]

were utilized for the synthesis of IF or NT structures of MQ_2 materials. In the sequel, diverse synthetic approaches to nanoparticles of layered metal chalcogenides are highlighted.

1.6.1. New Synthetic Routes toward TMDs

Since the above methods have to rely mostly on high temperatures and/or complicated processes they may not be optimally suited for a large-scale preparation of pure nanostructured metal chalcogenides with a minimum amount of side products. On the other hand, as the mechanical, physical, and catalytic properties of nanostructured chalcogenides strongly depend on their size and shape, it is desirable to devise synthetic procedures which enable us to control the particle size and morphology to a significant extent. From an application point of view, the focus on nanoparticle growth will be on high purity, high-yield,

and therefore low-cost products. Here the different synthetic techniques that are employed to synthesize the inorganic nanotubes and fullerene-like particles are reported.

1.6.1.1. Metal Organic Chemical Vapor Deposition (MOCVD)

The metal organic chemical vapor deposition technique is a well-known technique for the preparation of thin films and nanoparticles. One approach to suppress solid-state diffusion as a reaction parameter is based on a gas-phase MOCVD reaction. In the first synthetic step chalcogenide nanoparticles are formed in a gas-phase reaction between the naked metal, produced by thermal decomposition of the corresponding metal carbonyls, and sulfur or selenium, respectively. One might speculate that in a subsequent growth step the lamellar sheet fragments continue to grow and begin to loosen at their ends until they roll up into onion- or nanotube-type structures.

The particular advantages of this method are that

(i) the generalized procedure might be extended to other members of the MQ_2 group, provided that volatile precursors are available,

(ii) the synthesis of solid solutions $M_{1-x}M'_xQ_2$ or $MQ_{1-x}Q'_x$ or even ternary phases may be envisioned,

(iii) a study of the initial phases of the reaction with sophisticated *in situ* techniques could be done, but still,

(iv) the reaction can be stopped at any time in order to perform a time-dependent structural investigation of the reaction products.

(v) The procedure may be scaled up for the synthesis of large quantities by parallelization with the aid of microreactors,

(vi) the use of highly toxic reactants H_2S and H_2Se is avoided, and

(vii) a facile and fast synthesis of selenides (and even tellurides) without thermally labile H_2Se (H_2Te) is possible in quantitative amounts.

Following this MOCVD approach MQ_2 (where M= Mo, W, Re and Q= S or Se) [91-93] and $M_{1-x}M'_xS_2$ [93b] nanoparticles were prepared using metal carbonyls and elemental sulfur or selenium as starting materials. The resulting MQ_2 nanoparticles could be transformed to fullerene-like nanoparticles in subsequent annealing steps.

A feasible growth mechanism of S- and R-type (with different sizes) WS_2 nanoparticles is depicted in Figure 1-13. Nucleation of WS_2 is induced and controlled by the temperature; it occurs in the hot zone of the induction furnace around the graphite coil if $T>T_{min}$ (as W and S are highly dispersed T_{min} will be lower than for the bulk synthesis of WS_2 from the elements).

The extension of the hot zone is small for low T, and it increases with increasing T. The key factor for the formation of particles with different sizes would be the difference in the retention times of the particles in the growth region, *i.e.* the region with T>Tmin. S-type particles appear to traverse only a short trajectory through the growth region. Particles experiencing a longer trajectory through the growth region are more likely to form aggregates. The longer reaction time also enabled these particles to adopt the energetically preferred spherical equilibrium morphologies: The higher the reaction temperature, the more extended the growth region and therefore the more different the trajectories. This leads to a less controllable particle size but a higher amount of R-type particles.

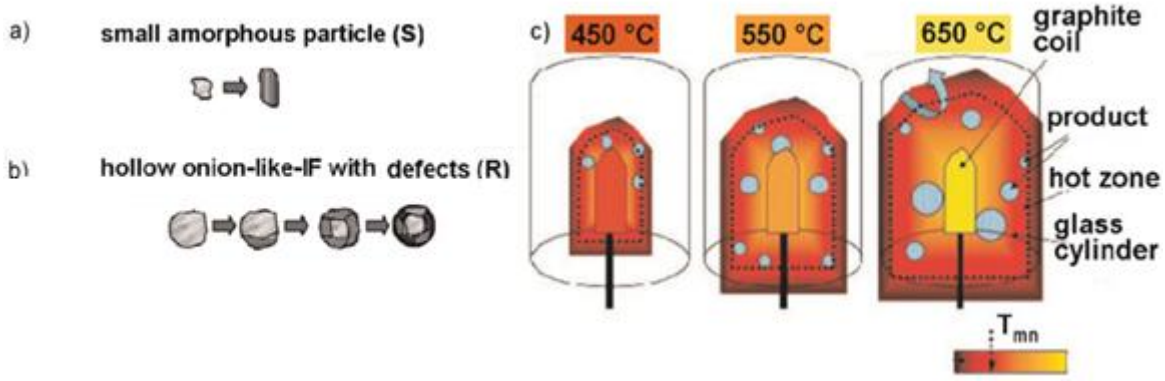

Figure 1-13. Formation of (a) S-type and (b) R-type particles – scheme and TEM images. (c) Schematic representation of the hot zone of the reactor around the graphite coil. A dotted line represents the minimum temperature needed for particle growth.

In the case of ReS_2, the role of the duration of stay of particles in the growth zone was found to be crucial for the formation of fullerene-like particles (Figure 3). Similar as observed in the case of IF-WS_2, IF-ReS_2 particles with different sizes were obtained; most importantly, a minimum diameter was required for IF-ReS_2 particles to be formed in order to reduce the size distribution of the particles, the temperature of the reactor (*i.e.* the growth zone) has to be increased or the volume of the growth region has to be reduced in order to level the trajectories of the individual particles.

For particles with diameters as small as 10–20 nm diffusion is complete after formation. As a result, nucleation becomes the rate-limiting step in the formation of the ordered ‘‘crystalline’’ solid (IF-ReS_2). When the amorphous particles are heated, ReS_2 starts to nucleate and grow until its growth exhausts one of the reactants within the particle volume or until the particle boundary is reached (see Figure 1-14).

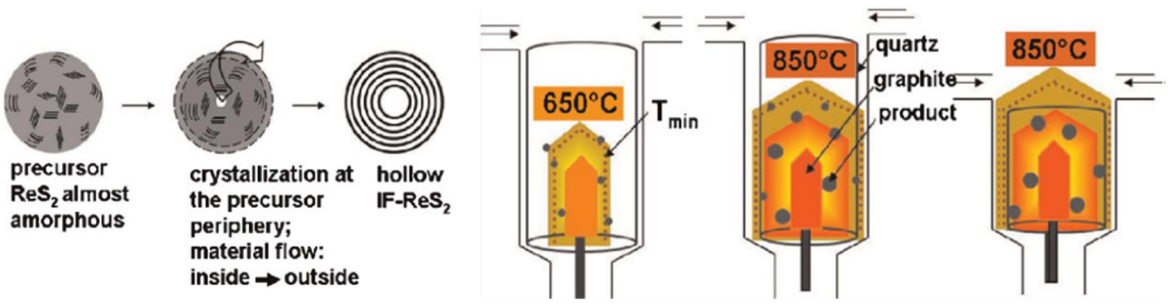

Figure 1-14. Top: Hot growth zone around the graphite receptor. The brown dotted line represents the minimum temperature required for particle growth. Bottom: Formation of a hollow IF-ReS_2 nanoparticle from an amorphous Re-S mixture.

1.6.1.1.1. Formation Mechanism of IFs

In order to obtain a better understanding of the particle growth an *in situ* heating TEM study was carried out where the formation of IF-WS_2 and IF-MoS_2 from amorphous MoS_2 and WS_2 precursor nanoparticles obtained via metal organic chemical vapor deposition (MOCVD) was monitored. From the electron micrographs it is evident that during the growth of these onion-like particles, defect annealing processes take a prominent role.

In order to trap reaction intermediates of the nested fullerene formation, the reaction must be kinetically controlled, *i.e.* solid state diffusion must be excluded as the rate determining step [94]. This can be achieved either by reducing the diffusion pathway, *i.e.* making the particles small, or by enhancing the atom mobility by adding a suitable mineralizing agent. For this iodine is used as the mineralizing agent. This diffusion enhancement resulted in the formation of giant MoS_2 ‘‘bubbles’’ with a controlled shell thickness about 5 nm and void sizes around 120 nm through the enhancement of surface diffusion with iodine.

The possibility of fast heating/cooling of the reaction zone makes this induction heated setup advantageous compared to the slow temperate ramps achievable using tube furnaces because ‘‘quenching’’ of the reaction is possible at any time. The giant fullerenes are the intermediates of not only a ‘‘size-up’’ step on a ‘‘shrinking hot giant’’ road to IF chalcogenides, but also in chemical transport reactions of layered chalcogenides.

The formation of the large interior voids might be traced back to formation of a gaseous phase through the thermal decomposition of the amorphous ternary Mo-S-I precursor phase. Part of the vapor phase (iodine or molybdenum iodide) is trapped within the newly forming fullerene-like structure. Upon annealing the thermal decomposition of the precursor particles proceeds, while, at the same time, the vapor pressure within the fullerene increases. This leads to a ‘‘size-up’’ effect through the thermal expansion of the encapsulated gas phase where the forming fullerene particle is stable as long as the pressure inside the fullerene remains below a

‘‘burst’’ threshold value (Figure 1-15). At the same time the iodine vapor within the fullerene leads to the formation of a surface film that makes the molybdenum and sulfur atoms mobile by isothermal chemical transport action of the halogen in the surface film. The steady loss of iodine to the gas phase promotes the formation of nuclei on the surface and thus leads to an enhanced and accelerated rebuilding of the IF-MoS_2 fullerene shell.

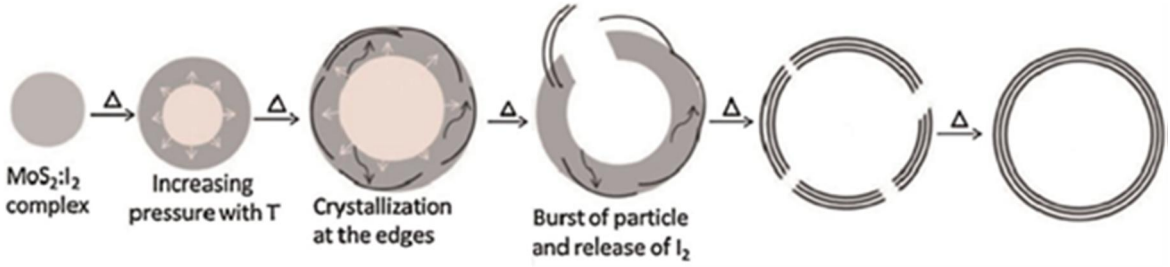

Figure 1-15. Growth mechanism of giant IF-MoS_2 ‘‘bubbles’’.

1.6.1.2. Vapor–liquid–solid (VLS) Growth

The vapor– liquid–solid (VLS) growth technique is a well-known technique for the synthesis of semiconductor nanowires. Nanowire growth has been achieved by catalytic growth using a metallic seed (typically Au) particle [95]. In these experiments the Au catalyst nanoparticles are supported on a SiO_2 substrate, and laser ablation was used to generate the reactants from a solid target. Growth ideally takes place underneath the metal droplet. Therefore, the nanowires are grown at low temperature where the growth on the noncatalyzed side surfaces is kinetically hindered. The unidirectional growth is usually explained by the vapor-liquid-solid (VLS) mechanism where a liquid droplet works as a preferential sink for the growth elements, which precipitate at the liquid-gas phase boundary.

Tin disulfide adopts the layered CdI_2 structure type, where the tin atoms are located in octahedral voids between two close packed slabs of sulfur to form a three-atom layered sandwich structure [96]. Since SnS_2 decomposes at temperatures >400 °C, it is envisioned that the VLS growth technique using low melting metals as catalysts can be used for the synthesis of SnS_2 nanotubes. For this, the initial studies started by using tin metal (melting point of 232 ºC) as a self-catalyst by vapor transport technique [97]. Using tin metal as self-catalyst resulted in the formation of IF-SnS_2 particles. The formation of the SnS_2 fullerenes occurs by sulfidization of tin nanoparticles formed by vapor transport.

As Bi and Sn are known to form an eutectic mixture around 150 ºC it is reasoned that Bi droplets might act as a sink for the growth species (SnS_2 and/or S) from the gas phase and subsequently as a seed for the growth of the SnS_2 nanotubes [98]. When bismuth was used as a catalyst, SnS_2 nanotubes were obtained. Figure 1-16 represents a proposed mechanism for the growth of SnS_2 nanotubes using Bi as catalyst.

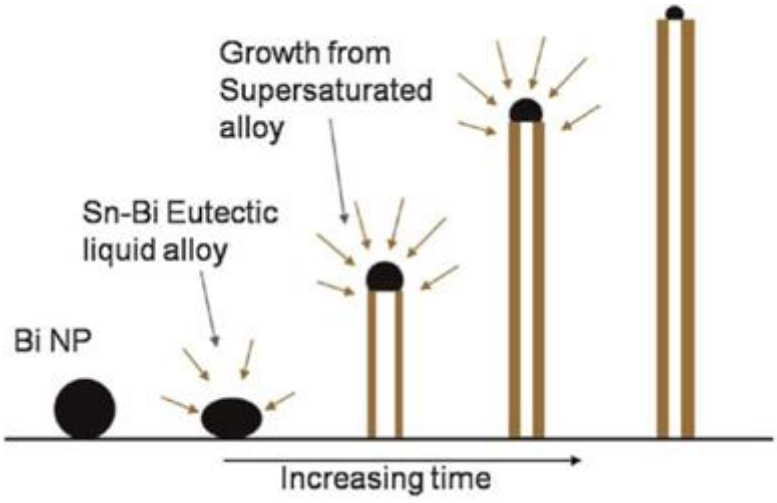

Figure 1-16. Proposed growth mechanism of the SnS_2 nanotubes with a bismuth catalyst.

1.6.1.3. Oxide-to-sulfide Conversion

Among the number of methods used for the synthesis of layered chalcogenide nanotubes, the most successful is the reductive sulfidization of oxide nanoparticles using H_2S. Initial studies were carried out on the conversion of tungsten oxide nanorods to NT-WS_2. The tungsten oxide nanorods were synthesized using a sol–gel technique, and the as-synthesized nanorods were used for the conversion to the sulfide nanotubes. Hexagonal WO_3 nanorods of 5–50 nm in diameter and 150–250 nm in length were obtained using the sol–gel process [99]. These WO_3 nanorods were highly suitable as a precursor for the synthesis of multiwalled NT-WS_2 by reduction with H_2S at 840 ºC for 30 min. The length and the wall thickness of the WS_2 nanotubes could be altered by controlled reduction of the oxide precursor.

Figure 1-17 shows TEM and HRTEM images of the oxide nanorods and the sulfide nanotubes resulting from the sulfidization. A mechanism for the growth of nanotubes from oxide whiskers and rods has been proposed previously by Tenne and coworkers [100,101]. According to this mechanism the growth of WS_2 layer starts by engulfing the WO_x particle in the initial phase of the reaction with a mantle of WS_2. During the course of the reaction this embryonic WS_2 layer starts growing inward as well as slowly converting of the oxide, which is continuously growing on the other end of the particles by the condensation of WO_x from the

vapor state. A similar mechanism is plausible in the present nanotube synthesis, where the reducing H_2/N_2 gas was replaced by a pre-treatment of the oxide with Ar gas. A TEM analysis of the oxide rods after the pretreatment with Ar shows the formation of an intermediate tungsten oxide with many defects while the appearance of the rods was retained. This could be related to a higher surface activity of the oxide nanorods.

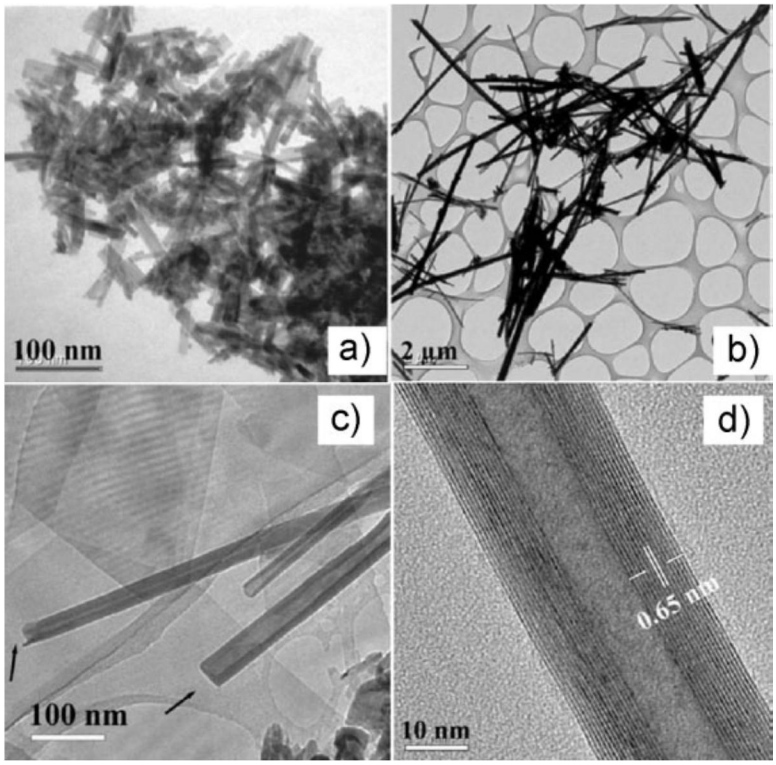

Figure 1-17. TEM (a, b) and HRTEM (c, d) images of the oxide nanorods (a) and the product obtained after sulfidization of the oxide nanorods (b–d).

The morphology of the starting compounds is intimately connected to the morphology of the final products. It is not only the spherical nanoparticles and nanorods that can be converted to the corresponding sulfide hollow structures, but the oxide nanotubes with an amine template molecules intercalated between the layers can also be converted to the sulfide nanotubes by retaining their original tubular morphology [102].

The amine intercalated vanadium disulfide nanotubes is the first layered chalcogenide nanotubes in which the organic molecules are intercalated in between the layers. Figure 1-18 shows TEM and HRTEM images of a partially and a fully sulfidized VS_2 nanotube with lattice fringes corresponding to a layer separation of approximately 2.8 nm (partially sulfidized and 1.6 nm (fully sulfidized). These values are significantly larger than the layer separations in bulk VS_2 (0.57 nm) [102a].

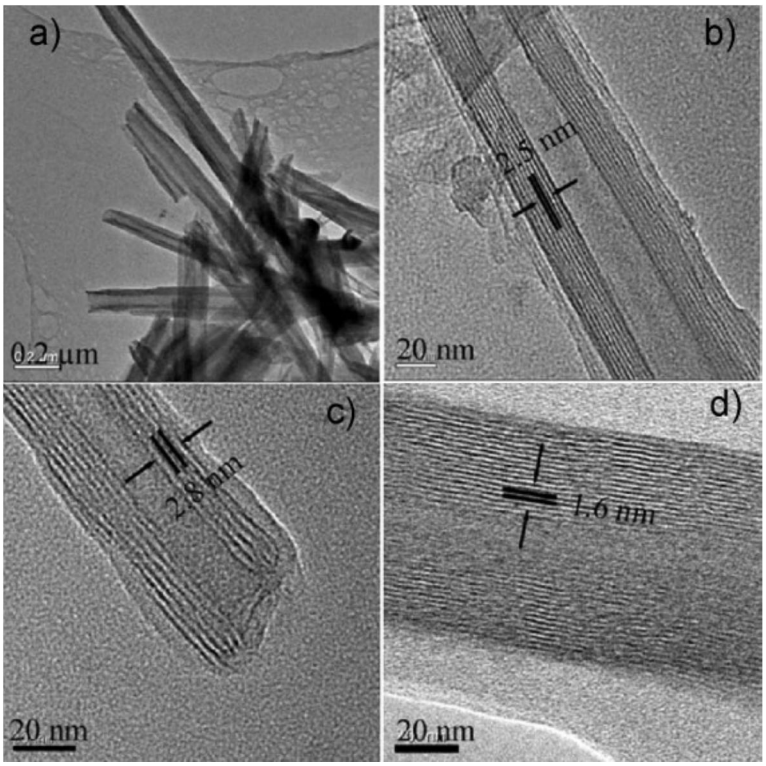

Figure 1-18. TEM and HRTEM images of the product obtained after the sulfidization of vanadium oxide nanotubes. (a) Low resolution overview TEM image of VO_x nanotubes used as a starting material for the synthesis of NT-VS_2. (b) HRTEM image of a single VO_x nanotube with a layer separation of 2.5 nm. (c) HRTEM image of a single VS_2 nanotube obtained from NT-VO_x intercalated with C_{16}-amine with a layer separation of 2.8 nm and a flat cap, showing a partially crystalline or amorphous coating. (d) HRTEM of a NT-VS_2 obtained from NT-VO_x intercalated with C_{12}-amine, with a layer d-spacing of 1.6 nm.

As a step further, the oxide to sulfide conversion technique was employed for the synthesis of the doped inorganic nanotubes. The niobium oxide nanorods were synthesized by a sol–gel process. And the as obtained Nb_2O_5 nanowires (NWs) were then coated with tungsten oxide by using a solvothermal approach [103]. The coated oxide nanorods upon annealing leads to the diffusion of tungsten into the niobium lattice resulting in the formation of mixed oxide nanorods. The coated NWs were sulfidized in a reaction by heating the coated NWs in Ar gas to 850 ºC while passing a stream of a H_2S for 30 min. Oxide to sulfide conversion takes place analogously to the way described for pure WS_2 nanotubes resulting in the formation of Nb–W–S composite nanostructures. The product contains stacked MS_2 platelets with diameters ranging from 40 to 60 nm, while the length of the stacks varies between 1 and 8 µm (Figure 1-19).

HRTEM images show these structures to be very different from the conventional curved nanostructures typically observed for layered chalcogenides, with a stacking of the layers

perpendicular to the growth direction of the chalcogenide nanotubes. Parallel platelet-like segments appear in an alternating periodic manner along the growth direction of the stacks. The layers within the stacks are generally smooth. Apparently the layers tend to bend between each segment at a length scale of about 5 nm. EDX reveals the presence of both, niobium and tungsten.

A closer view of the layers reveals diffuse bending and kinking that increase along the edges of the stacks (Figure 1-19) while the whole structure remains straight. Kinks, interruption of layers, orthogonal faults, and low contrast areas are common observed. The formation of all these defects can be related to the large compressive lateral lattice mismatch strain between NbS_2 and WS_2 during their growth. Substituting approx. 30% of niobium by tungsten leads to the formation of stacked NWs due to internal strain, rather than to the formation of Nb doped $Nb_xW_{1-x}S_2$ nanotubes.

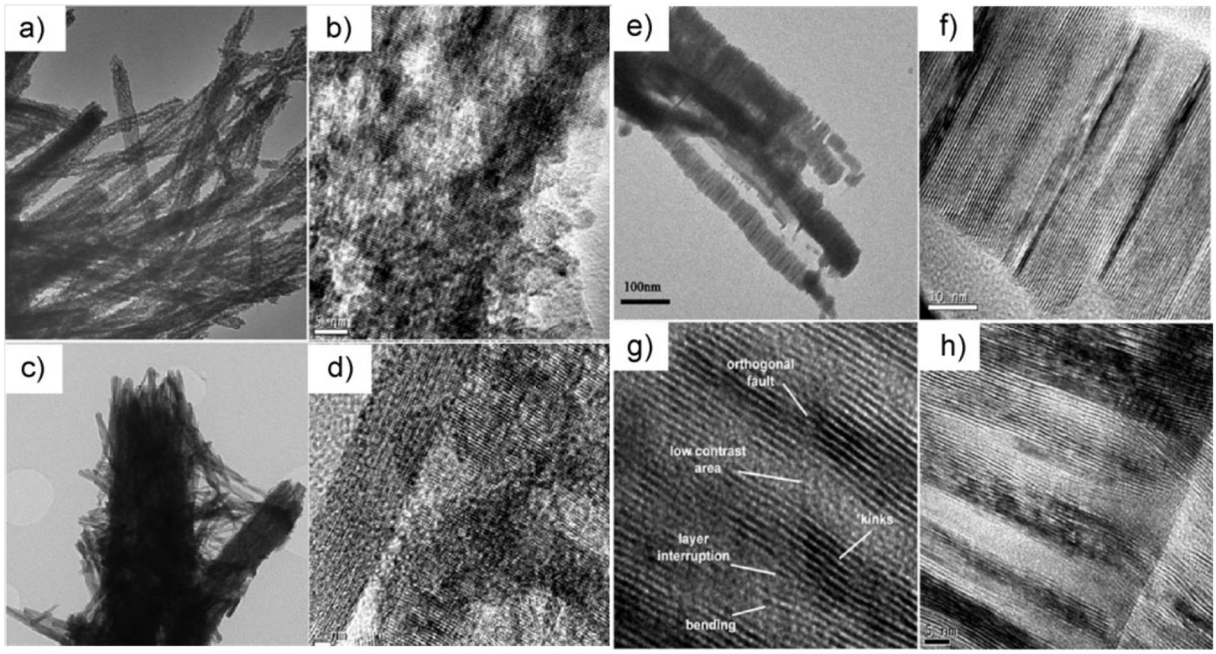

Figure 1-19. TEM and HRTEM images of pure niobium oxide nanorods and tungsten oxide coated niobium oxide and the product obtained after sulfidization of tungsten oxide coated niobium oxide nanorods. (a) TEM image of the Nb_2O_5 NWs obtained after the sol–gel process and (b) HRTEM image of a single NW obtained from the sol–gel process. (c) After solvothermal treatment the niobium oxide NWs were fully covered with tungsten oxide. (d) HRTEM image of a niobium oxide NW partially covered with tungsten oxide. (e–h) HRTEM images of the CRNWs. (e,f) High resolution images showing the curving of the layers along the segments. (g,h) Periodic alternation along the stack.

The synthetic methods, corresponding temperature and obtained morphologies are compiled in Table 1-2.

Table 1-2. Compilation of synthetic methods, temperatures, and product morphology.

compound	synthetic method	synthesis steps	temperature (°C)	morphology	reference
MoS_2	MOCVD	two steps	i) 350-550 ii) 850	fullerene	[94]
MoS_2	MOCVD	two steps	i) 400 ii) 800	fullerene	[91]
$MoSe_2$	MOCVD	two steps	i) 450 ii) 800	fullerene	[91]
ReS_2	MOCVD	two steps	i) 750 ii) 800	fullerene	[93a]
WS_2	MOCVD	two steps	i) 450-750 ii) 800	fullerene	[92]
WS_2	i) hydrothermal ii) sulfidization	two steps	i) 180 ii) 840	nanotubes	[99]
VS_2	i) hydrothermal ii) sulfidization	two steps	i) 180 ii) 225	Nanotubes	[102a]
$W_{1-x}Nb_xS_2$	i) hydrothermal ii) sulfidization	two steps	i) 180 ii) 850	coin-roll nanowires	[103]
SnS_2	vapor liquid solid growth	single step	800	nanotubes	[98]

1.7. Graphene and Beyond It

In the last couple of years, graphene and its synthetic strategies has become one of the most exciting topics of research world [104-109]. This 2D material serves as a new nanocarbon comprising layers of carbon atoms forming six-membered rings. It is distinctly different from carbon nanotubes and fullerenes and exhibits unique properties. The most important properties of graphene are fractional quantum Hall effect at room temperature [110-112], an ambipolar electric field effect along with ballistic conduction of charge carriers [113], tunable band gap [114] and high elasticity [115].

Ideally graphene is a single-layer material, but graphene samples with two or more layers are being investigated with equal interest. Three different types of this material are defined as single-layer (SG), bi-layer (BG) and few-layer graphene (number of layers $\leq$10).

Graphenes with varying number of layers can be synthesized by different strategies [107,108,116]. SG and BG graphene are obtained by the reduction of single layer graphene oxide, CVD and other methods like micromechanical cleavage. Few-layer graphenes are

prepared by the conversion of nanodiamond, arc discharge of graphite and other means. Nevertheless, well-defined procedures for the synthesis of graphenes with the desired number of layers have not been established yet.

1.8. Inorganic Analogues of Graphene

1.8.1. Synthesis

Following the discovery of inorganic congeners for fullerene and carbon nanotube (as mentioned in section 1.3) and chronological discovery and characterization of graphene, it would seem natural to explore the synthesis of graphene analogues of inorganic materials such as layered TMDs [117]. In an early report [118], graphene-like MoS_2 was prepared by lithium intercalation and exfoliation, but the material was just characterized by X-ray diffraction and consequently the exact nature and number of layers could not be determined. The single layers of WS_2 were also obtained by lithium intercalation and exfoliation [119,120] and there again the product was only characterized on the basis of *(002)* reflection in the X-ray diffraction pattern. Since even few-layer MoS_2 and WS_2 containing five layers do not exhibit the *(002)* reflection significantly, it is necessary to investigate inorganic graphene analogues by transmission electron microscopy and other techniques.

Rao *et al.* employed alternative synthesis methods to synthesize graphene-like MoS_2 and WS_2. The first method involved lithium intercalation of bulk MoS_2 and WS_2 and exfoliated in water. Reaction between lithium-intercalated MoS_2 and WS_2 and water results in the formation of lithium hydroxide and hydrogen gas bringing about the separation of the layers of the sulfide and the loss of periodicity along the c-axis. In the second method, molybdic- and tungstic acid were reacted with excess of thiourea in an inert atmosphere at 500 ºC. The last method involved the reaction between MoO_3 and KSCN under hydrothermal conditions [121].

The XRD patterns of the molybdenum sulfide samples obtained by the three methods display no *(002)* reflection. Energy dispersive x-ray analysis (EDX) shows the products to be stoichiometric MoS_2. TEM images of the products obtained from these three procedures show the presence of one or few layers of MoS_2 (Figure 1-20). Graphene analogues of WS_2 also prepared by two methods are also shown. The TEM images reveal that WS_2 obtained from both methods 1 and 2 mostly consists of SGs and BGs.

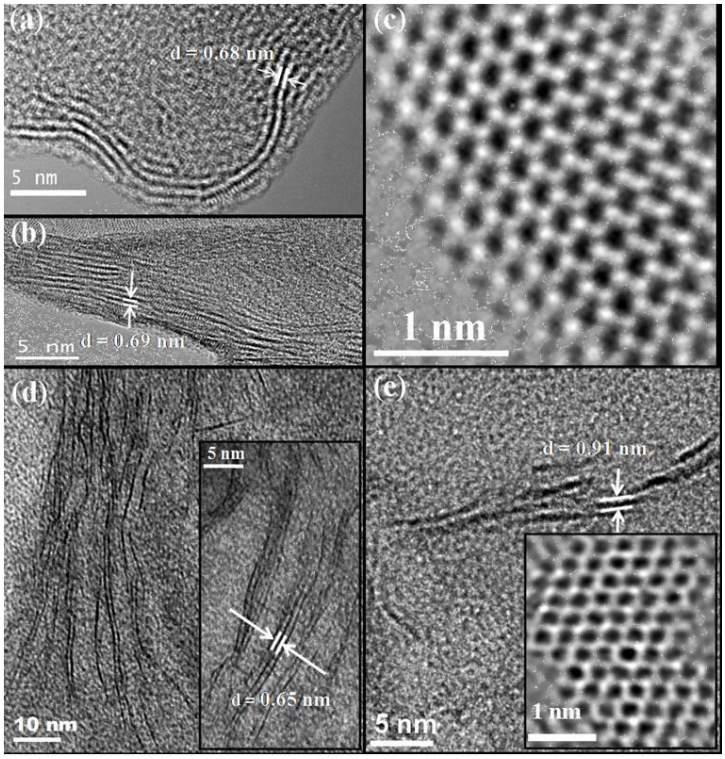

Figure 1-20. (a) and (b) the TEM images of MoS_2 layers obtained by Methods 2 and 3, (c) is the high resolution TEM image of layered MoS_2 from Method 3, (d) and (e) images of WS_2 layers from Methods 1 and 2 respectively. The bends in the layers can arise from defects [122].

The graphene-like MoS_2 layers (obtained from methods 2 and 3) show a layer separation in the range of 0.65-0.7 nm. The high resolution image shows the hexagonal structure formed by Mo and S atoms with a Mo-S distance of 2.30 Å. AFM images and the height profiles of the products also confirm the formation of few-layer MoS_2. In Figure 1-21, the Raman spectra of graphene-like MoS_2 samples prepared by this method is compared with the spectrum of bulk MoS_2 [122].

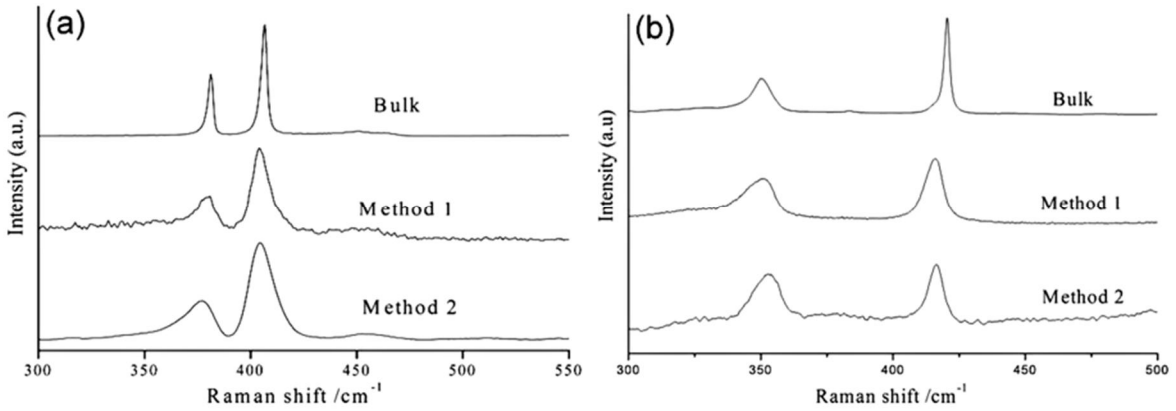

Figure 1-21. Raman spectra of (a) bulk MoS_2 and MoS_2 layers obtained by Methods 1 and 2 and (b) bulk WS_2 and WS_2 layers obtained by Methods 1 and 2 [122].

The bulk sample gives bands at 406.5 and 381.2 cm^{-1} due to the A_{1g} and E_{2g} modes with the full-width half maximum (FWHM) of 2.7 and 3.1 cm^{-1} respectively. The sample obtained by lithium intercalation exhibits the corresponding bands at 404.7 and 379.7 cm^{-1}. The sample obtained by Method 2 show these bands at 404.7 and 377.4 cm^{-1}. There is a clear softening of the A_{1g} and E_{2g} modes in the graphene analogues of MoS_2. Furthermore, the FWHM values are larger in the graphene-like samples, the values varying from 10 to 16 cm^{-1} compared to ~3 cm^{-1} in the bulk sample. The broadening of the Raman bands is considered to be due to the phonon confinement. The broadening also suggests that the lateral dimensions of these layers are in the nano regime.

Raman spectra of WS_2 obtained by both the methods show softening of the bands due to the A_{1g} mode (see Figure 1-22). Compared to the narrow bands at 351 (E_{2g}) and 420 cm^{-1} (A_{1g}) of bulk WS_2 with FWHM values around 7.8 and 2.4 cm^{-1} respectively, the spectrum of WS_2 obtained from lithium intercalation shows bands at 350 and 415 cm^{-1} with FWHM values of 13.7 and 8.4 cm^{-1}. The Raman spectrum of WS_2 layers synthesized by Method 2 also shows similar softening of the Raman bands and increase in the FWHM [122].

Rao and his co-workers also reported a bottom-up chemical synthesis of few-layer BN [123]. The synthesis of single- and few-layer graphene-type BN sheets involves the reaction of boric acid with different proportions of urea at 900°C. They have shown that the number of BN layers decreased with the increase in urea content in the reaction mixture, allowing a control on the number of BN layers (Figure 1-22). First principles simulations show that it is energetically easy for few-layer BN to form stacking faults that involve slips and twists of adjacent planes resulting in inhomogeneity in the interplanar distances and deform through forming ripples. It has a smaller buckling strength and elastic stiffness than graphene.

Long-range Coulomb interactions are found to be important to the stability of the different structures of BN.

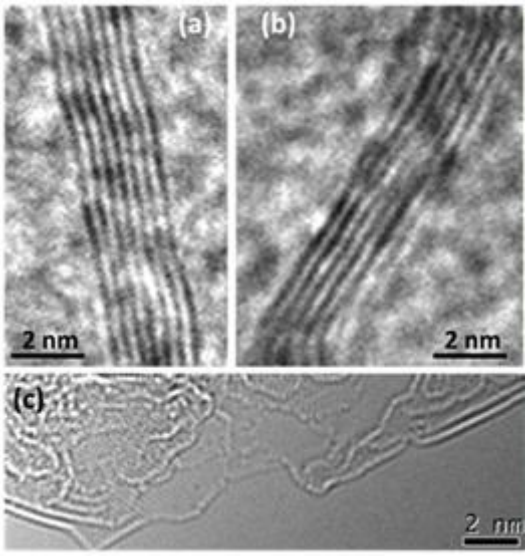

Figure 1-22. TEM images of few-layer BN prepared with (a) 1:12, (b) 1:24, and (c) 1:48 boric acid/urea mixture [123].

1.8.1.1. Liquid Exfoliation

Like carbon graphene [124], layered metal chalcogenides can also be exfoliated to utilize their full potential. For example, Bi_2Te_3 on exfoliation showed enhanced thermoelectric efficiency due to suppression in thermal conductivity [125]. Typically topological insulators, on exfoliation reduced the conductance. Also electronic properties get changed when the number layers is reduced; for example, the indirect band gap of bulk MoS_2 becomes direct bandgap materials on exfoliation to a few-layers thick flakes [126]. Like carbon graphene, the exfoliation of layered metal chalcogenides can also be mechanically on a small scale [127,128], but liquid-phase exfoliation methods are more successful to explore many applications [129]. These liquid exfoliation methods provide the basis to synthesize novel hybrid and composite materials [130-132].

A very general solution based exfoliation method has been reported by Coleman and his co-workers for almost all kinds of layered metal chalcogenides. According to this method, layered compounds such as MoS_2, WS_2, $MoSe_2$, $MoTe_2$, $TaSe_2$, $NbSe_2$, $NiTe_2$, BN, and Bi_2Te_3 can be successfully dispersed and exfoliated in most of the common solvents and can be deposited as individual flakes or films [133].

The main procedure involves the sonication of commercial MoS_2, WS_2, and BN powders in a number of solvents sorted on the basis of different surface tensions. The sheets were purified using centrifugation and decanting the supernatant. These exfoliated products showed enhanced optical properties in solvents with surface tension close to γ-40 mJ/m^2 [134,135]. The results can be explained using Hansen solubility parameter theory [136]. According to this theory, successful solvents for the exfoliation are the one with dispersive, polar, and H-bonding components of the cohesive energy density within certain well-defined ranges. This can be concluded that those solvents which minimize the energy of exfoliation can be successfully used to obtained single sheets.

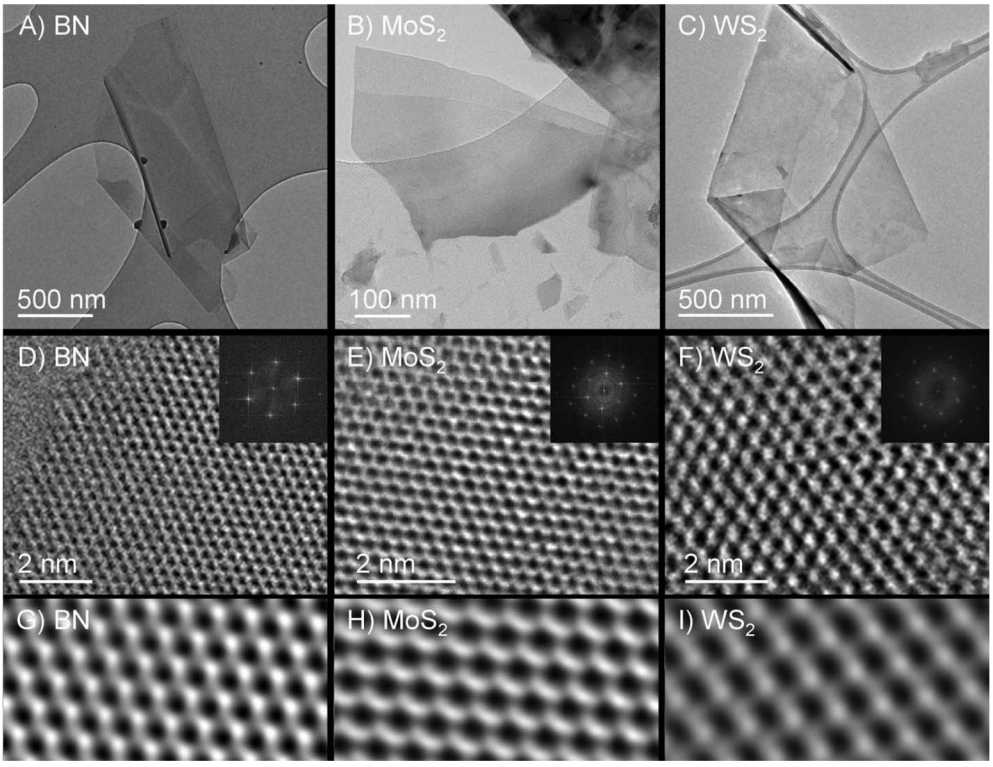

Figure 1-23. TEM of nanosheets. (A to C) Low resolution TEM images of flakes of BN, MoS_2, and WS_2, respectively. (D to F) High-resolution TEM images of BN, MoS_2 and WS_2 monolayers. Insets: Fast Fourier transforms of the images. (G to I) Butterworth-filtered images of sections of the images in (D) to (F) [133].

Based on this strategy, the exfoliated sheets as imaged by high resolution transmission electron spectroscopy are shown in Figure 1-23. TEM data strongly suggests that the exfoliated materials are consisting of single layers. The typical sizes imaged for these objects were ranging from 50 to 1000 nm for MoS_2 and WS_2 and 100 to 5000 nm for BN. The HRTEM images and associated Fourier transforms illustrate the hexagonal symmetry of these

materials. This is in contrast to the data reported for MoS_2 and WS_2 single sheets exfoliated using lithium intercalation, which results in deviation from hexagonal structure [137,138]. The images processed using Butterworth filtering revealed B-N bond lengths of 1.45 Å and MoS_2 and WS_2 hexagon widths of 3.8 Å and 4 Å, which confirm that no distortions were introduced as a result of exfoliation.

Since the solvent mediated exfoliation results in a very homogenous solution which is stable over days, the flakes can be deposited on substrates by spraying to get thin films. Figure 1-24 shows SEM and AFM images of MoS_2 films deposited on silicon wafer. The data obtained well matches with the data obtained from TEM. Raman mapping, also confirm that the flakes consist of MoS_2; the peak positions [139] shows the trigonal prismatic (2H) mono- or bilayer of MoS_2. SEM analysis also shows that although some deposited flakes are very thin, many are multilayers or clusters that have aggregated during deposition. AFM and STM imaging of individual flakes show them to display typical thicknesses of ~3 to 12 nm. Some of these images (like STM image in Figure 1-24), show steps. These are consistently ~1 nm high and probably originate in layer edges.

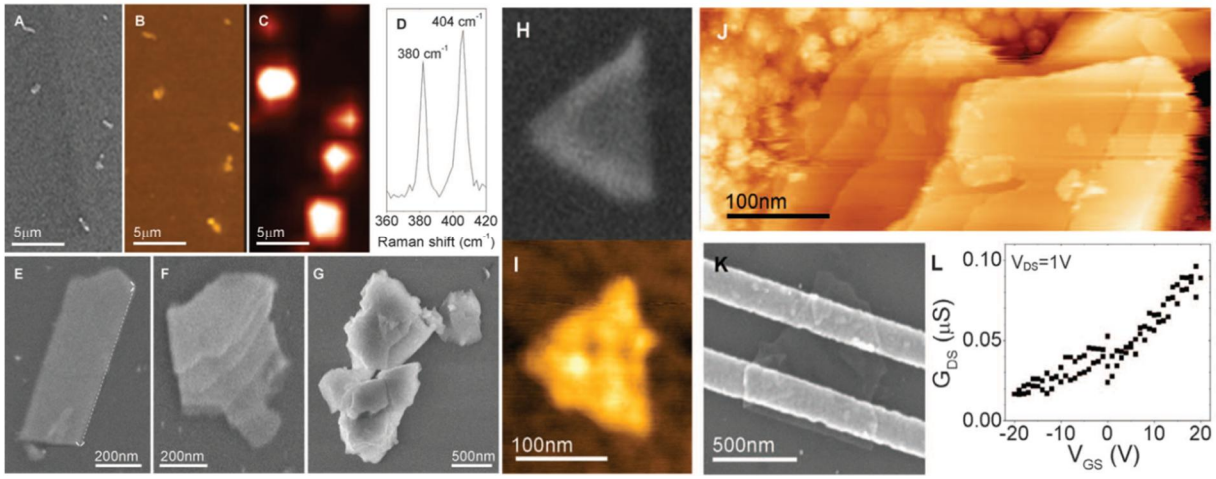

Figure 1-24. Deposition of nanosheets onto surfaces. (A and B) An SEM and an AFM image of MoS_2 flakes deposited on SiO_2 by spraying. (C) A Raman map of the same region. (D) Typical Raman spectrum of an individual flake. The Raman map plots the integral of the spectrum between 390 and 410 cm^{-1}. (E to G) A very thin flake, a multilayer, and a cluster of aggregated multilayers. The dashed line in (E) has been inserted to illustrate the straightness of the flake edge. (H and I) SEM and AFM images of an individual flake. (J) An STM image of an individual flake. The flakes in (I) and (J) have heights of 5 and 10 nm, respectively (25). (K) An SEM image of a MoS_2 flake on Si/SiO_2 with electrodes deposited on top. (L) Drain-source conductance (GDS) as a function of gate voltage (VGS) for the flake shown in (K). VDS is the applied drain-source voltage [133].

1.9. Scope and Aim

Despite a number of reports on the formation mechanism of INTs and IFs, many questions still remain to be resolved on this subject and therefore, there is need to develop new strategies to study the formation mechanism of these structures. The quenching of reactions allows monitoring of the reaction proceeding which became possible through the fast heating/cooling of the reaction zone in an induction furnace [94]. One way to study the formation mechanism of such structures and determining the role of diffusion for slow heating/cooling is using iodine as chemical transport agent and studying the amorphous Mo-S-I precursor particles captured from the reaction after annealing at elevated temperature. The effect of the iodine could also be studied by changing the molecular precursors' ratio (e.g. molybdenum carbonyl to iodine).

Like in the case of MoS_2 nanoparticle bundles, this method could be used to study the formation of 2H-WS_2@IF-WS_2 nanostructures as reaction intermediates. Different electron microscopy techniques such as TEM, STEM and dual SEM/FIB could be used to study the internal volume of the nested nanostructures. Finally, contact-mode AFM could be used to measure the stiffness of the fullerene shells.

The most promising technique to obtain the IF and INT of TMDs is the oxide to sulfide conversion technique which employs using oxide precursor nanoparticles to obtain the IF and INT. The final morphology will be dictated by the precursor oxide nanoparticles, for example, the round oxide nanoparticles leads to the formation of IF nanoparticles whereas the oxide nanorods leads to the formation of nanotubes. Normally, high temperatures around 850ºC are required to sulfidize the corresponding oxide nanoparticles.

With the recent developments in the chemistry of nanomaterials and rising demand to meet the full potentials of the chalcogenide nanoparticles, it is helpful to find a novel route to synthesize most applicable chalcogenide nanoparticles such as tungsten sulfide nanotubes in massive quantity. An important factor would be the ability of the chalcogenide nanoparticle surface to be functionalized. The presence of defects on the surface has been shown to provide such ability. The functionalization behavior of these nanotubes could be investigated using different metal and metal oxide nanoparticles such as gold, manganese oxide and Pt@Fe_3O_4 Janus nanoparticles based on Pearson's HSAB principle.

The direct transfer of the initial morphology to the end product during the sulfidization has been observed so far in the case of spherical nanoparticles (which form fullerenes and other onion-like morphologies) and also nanowires and nanorods (which form nanotubes). In order

to investigate whether the preservation of the morphology applies for any other structures, the oxide to sulfide conversion method could be utilized to convert WO_3 low aspect ratio nanorods to corresponding sulfides and it is helpful to use novel techniques such as ADT to investigate the effect of the oxide precursor crystal structure on the final morphology of the sulfide product.

An important and promising strategy for chemical modification of inorganic nanoparticles is the intercalation with a variety of metals and nucleophilic groups. Reversible intercalation of foreign atoms and molecular moieties could make them applicable in rechargeable batteries; drug delivery; remediation of water and for the use as detectors / sensors. An example is the gas-phase intercalation of Na, K and Rb atoms in IF-WS_2 [140]. The *c*/2 lattice spacing between the layers was shown to significantly expand upon intercalation. However, due to the substantial lattice strain, this lattice expansion (0.81 nm) is limited to the outermost layers (see Figure 1-25) and the innermost closed WS_2 layers remain unchanged (0.62 nm).

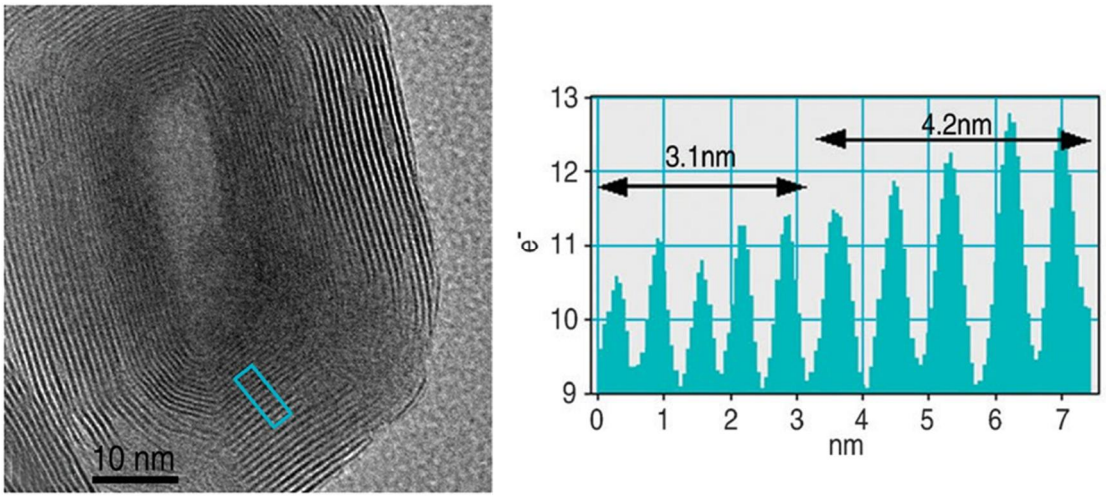

Figure 1-25. TEM image of an individual IF-WS_2 nanoparticle partially intercalated with Rubiduim atoms. Due to the significant strain, the intercalation which is indicated by lattice expansion (0.64 nm) of the closed shells is limited to the outermost 15 layers. The innermost layers of the nanoparticle exhibit the regular lattice spacing (0.62 nm) [140].

Since the walls of the nanotubes and fullerene-like nanoparticles are chemically very inert and quite impermeable, the diffusion of the guest moiety depends on the availability of weak links, *i.e.* surface defects or open tips at the nanotube edges. However, when the nanotube is not fully crystalline and its walls are made of small crystallites, the fast intercalation becomes possible leading to rapid charge/discharge cycles and high capacity for the guest atoms.

The restriction of convenient layered chalcogenide nanoparticles toward the intercalation could be overwhelmed by selecting an appropriate intercalation host. $Nb_{1-x}W_xS_2$ coin-roll

nanowires (CRNWs) might be a choice as in fact, the miniaturization of 2D structures by lateral confinements, makes them potential candidates not only for modulation of electron-transport phenomena, but also enhances their host capabilities arising from the enlarged surface area and improved diffusion properties upon the intercalation of guest molecules due to the finite lateral size and enhanced open-edge morphology of the 2D nanosheets. However, the intercalation and exfoliation of this type of nanowires leads to generation of a new type of graphene-type sheets, *e.g.* a mixed metal chalcogenide phase. The stabilization of the as-synthesized graphene-type sheets in the aquatic solution and other solvents could be enhanced by *in situ* functionalization of the graphene-type sheets using for example gold nanoparticles.

In this doctoral thesis, effective approaches to adapt and optimize the synthesis, stabilization and solubilization of **0D**, **1D** and **2D** nanostructures of layered TMDs are described and the probable mechanism for the formation of these nanostructures are proposed. These methods should allow high-yield, low-cost synthesis of homogeneous samples. For this purpose, (i) a modified metal organic chemical vapor deposition (MOCVD) method being a combination of the MOCVD and the chemical vapor transport approach, (ii) sulfidization of oxides and (iii) intercalation/exfoliation have been investigated which will be presented in the subsequent chapters.

Standard sample characterization comprised X-ray diffraction (XRD), scanning electron microscopy (SEM), atomic force microscopy (AFM), scanning tunneling electron microscopy (STEM) and transmission electron microscopy (TEM) in conjunction with energy dispersive X-ray spectroscopy (EDX). Complementary, dynamic light scattering (DLS), focused ion beam (FIB), and automated electron diffraction tomography (ADT) was employed.

1.10. References

[1] R. P. Feynman, *Eng. Sci.* **1960**, *23*, 22.

[2] H. W. Kroto, J. R. Heath, S. C. O'Brien, R. F. Curl, R. E. Smalley, *Nature* **1985**, *318*, 162.

[3] D. Rouvray, *Chem. Br.* **2000**, *36*, 46.

[4] G. Lawton, *Chem. Ind. (London)* **2001**, 174.

[5] K. Havancsak, *Mater. Sci. Forum* **2003**, *414*, 85.

[6] H. Presting, U. Konig, *Mater. Sci. Eng. C: Biomim. Supramol. Syst.* **2003**, *C23*, 737.

[7] M. C. Roco, *Curr. Opin. Biotechnol.* **2003**, *14*, 337.

[8] G. Orive, R. M. Hernandez, A. Rodriguez Gascon, A. Dominguez-Gil, J. L. Pedraz, *Curr. Opin. Biotechnol.* **2003**, *14*, 659.

[9] G. Guetens, K. Van Cauwenberghe, G. De Boeck, R. Maes, U. R. Tjaden, J. van der Greef, M. Highley, A. T. van Oosterom, E. A. de Bruijn, *J. Chromatogr. B: Biomed. Sci. Appl.* **2000**,*739*, 139.

[10] M. F. Hochella, *Earth Planet. Sci. Lett.* **2002**, *203*, 593.

[11] C. M. Lieber, *MRS Bull.* **2003**, *28*, 486.

[12] A. L. Buchachenko, *Russ. Chem. Rev.* **2003**, *72*, 375.

[13] K. J. Klabunde, *Nanoscale Materials in Chemistry*; edited by K. J. Klabunde; Wiley-Interscience: New York, 2001.

[14] G. A. Ozin, A. C. Arsenault, *Nanochemistry*; RSC Publishing: Cambridge, 2005.

[15] S. Iijima, *Nature* **1991**, *354*, 56.

[16] K. S. Novoselov, A. K. Geim, S. V. Morozov, D. Jiang, Y. Zhang, S. V. Dubonos, I. V. Grigorieva, A. A. Firsov, *Science* **2004**, *306*, 666.

[17] (a) R. Tenne, L. Margulis, M. Genut, G. Hodes, *Nature* **1992**, *360*, 444; (b) Y. Feldman, E. Wasserman, D. J. Srolovita, R. Tenne, *Science* **1995**, *267*, 222.

[18] Y. R. Hachohen, E. Grunbaum, J. Sloan, J. L. Hutchison, R. Tenne, *Nature* **1998**, *395*, 336.

[19] H. A. Therese, F. Rocker, A. Reiber, J. Li, M. Stepputat, G. Glasser, U. Kolb, W. Tremel, *Angew. Chem.* **2005**, *117*, 267; *Angew. Chem. Int. Ed.* **2005**, *44*, 262.

[20] J. Chen, S. -L. Li, Z. -L. Tao, Y. -T. Shen, C. -X. Cui, *J. Am. Chem. Soc.* **2003**, *125*, 5284.

[21] J. A. Hollingsworth, D. M. Poojary, A. Clearfied, W. E. Buhro, *J. Am. Chem. Soc.* **2000**, *122*, 3562.

[22] (a) D. J. Srolovitz, S. A. Safran, M. Homyonfer, R. Tenne, *Phys. Rev. Lett.* **1995**, *74*, 1779; (b) N. G. Chopra, R. J. Luyren, K. Cherry, V. H. Crespi, M. L. Cohen, S. G. Louis, A. Zettl, *Science* **1995**, *269*, 966.

[23] (a) W. Tremel, E. W. Finckh, *Chem. unserer Zeit* **2004**, *38*, 326; (b) W. Tremel, *Angew. Chem.* **1999**, *111*, 2311; *Angew. Chem., Int. Ed.* **1999**, *38*, 2175.

[24] D. Li, X. L. Li, R. R. He, J. Zhu, Z. X. Deng, *J. Am. Chem. Soc.* **2002**, *124*, 1411.

[25] L. Margulis, G. Salitra, R. Tenne, M. Talianker, *Nature* **1993**, *365*, 113.

[26] P. A. Parilla, A. C. Dillon, B. A. Parkinson, K. Jones, J. Alleman, G. Riker, D. S. Ginley, M. J. Heben, *J. Phys. Chem. B* **2004**, *108*, 6197.

[27] M. B. Sadan, L. Houben, A. Enyashin, G. Seifert, R. Tenne, *Proc. Natl. Acad. Sci. USA* **2008**, *105*, 15643.

[28] A. N. Enyashin, S. Gemming, M. Bar-Sadan, R. Popovitz-Biro, S. Y. Hong, Y. Prior, R. Tenne, G. Seifert, *Angew. Chem., Int. Ed.* **2007**, *46*, 623.

[29] M. B. Sadan, L. Houben, S. G. Wolf, A. Enyashin, G. Seifert, R. Tenne, K. Urban, *Nano Lett.* **2008**, *8*, 891.

[30] J. V. Lauritsen, J. Kibsgaard, S. Helveg, H. Topsøe, B. S.Clausen, F. Besenbacher, *Nature Nanotech.* **2007**, *2*, 53.

[31] I. Kaplan-Ashiri, S. R. Cohen, K. Gartsman, V. Ivanovskaya, T. Heine, G. Seifert, I. Wiesel, H. D. Wagner, R. Tenne, *Proc. Natl. Acad. Sci. USA.* **2006**, *103*, 523.

[32] I. Kaplan-Ashiri, S. R. Cohen, Y. Wang, G. Seifert, H. D. Wagner, R. Tenne, *J. Phys. Chem. C* **2007**, *111*, 8432.

[33] (a) D. Golberg, P. M. F. J. Costa, M. Mitome, Y. Bando, *J. Mater. Chem.* **2009**, *19*, 909, Feature Article; (b) Y. Sun, J. Hu, Z. Chen, Y. Bando, D. Golberg, *J. Mater. Chem.* **2009**, *19*, 7592, Feature Article.

[34] M. Virsek, A. Jesih, I. Milosevic, M. Damnjanovic, M. Remskar, *Surf. Sci.* **2007**, *601*, 2868.

[35] S. D. Yu, L. X. Chang, H. B. Yang, B. B. Liu, Y. Y. Hou, L. Wang, M. G. Yao, T. Cui, G. T. Zou, *J. Phys.: Condens. Matter* **2007**, *19*, 425228.

[36] H. E. Unalan, Y. ang, Y. Zhang, P. Hiralal, D. Kuo, S. Dalal, T. Utler, S. N. Cha, J. E. Jang, K. Chremmou, G. Lentaris, D. Wei, R. Rosentsveig, K. Suzuki, H. Matsumoto, M. Minagawa, Y. Hayashi, M. Chhowalla, A. Tanioka, W. I. Milne, R. Tenne, G. A. J. Amaratunga, *IEEE Trans. Electron Devices* **2008**, *55*, 2988.

[37] I. Robel, B. A. Bunker, P. V. Kamat, *Adv. Mater.* **2005**, *17*, 2458.

[38] S. Banerjee, S. S. Wong, *Nano Lett.* **2002**, *2*, 195.

[39] L. Sheeney-Haj-Khia, B. Basnar, I. Willner, *Angew. Chem., Int. Ed.* **2005**, *44*, 78.

[40] M. Olek, T. Busgen, M. Hilgendorff, M. Giersig, *J. Phys. Chem. B* **2006**, *110*, 12901.

[41] S. Banerjee, S. S. Wong, *Chem. Commun.* **2004**, 1866.

[42] B. H. Juarez, C. Klinke, A. Kornowski, H. Weller, *Nano Lett.* **2007**, *7*, 3564.

[43] Y. J. Na, H. S. Kim, J. J. Park, *Phys. Chem. C* **2008**, *112*, 11218.

[44] M. N. Tahir, N. Zink, M. Eberhardt, H. A. Therese, U. Kolb, P. Theato, W. Tremel, *Angew. Chem., Int. Ed.* **2006**, *45*, 4809.

[45] J. K. Sahoo, M. N. Tahir, F. Hoshyargar, B. Nakhjavan, R. Branscheid, U. Kolb, W. Tremel, *Angew. Chem. Int. Ed.* **2011**, *50*, 12271.

[46] Y. Q. Zhu, T. Sekine, Y. H. Li, W. X. Wang, M. W. Fay, H. Edwards, P. D. Brown, N. Fleischer, R. Tenne, *Adv. Mater.* **2005**, *17*, 1500.

[47] A. N. Enyashin, S. Gemming, G. Seifert, *Springer Series in Materials Science* **2007**, *93*, 33.

[48] C. Shahar, D. Zbaida, L. Rapoportb, H. Cohen, T. Bendikov, J. Tannous, F. Dassenoy, R. Tenne, *Langmuir* **2010**, *26*, 4409.

[49] A. Katz, M. Redlich, L. Rapoport, H. D. Wagner, R. Tenne, *Tribol. Lett.* **2006**, *21*, 135.

[50] G. R. Samorodnitzky-Naveh, M. Redlich, L. Rapoport, Y. Feldman, R. Tenne, *Nanomedicine* **2009**, *4*, 943.

[51] D. B. Mohan, A. Cavaleiro, *Vacuum* **2009**, *83*, 1257.

[52] M. Naffakh, C. Marco, M. A. Gomez, I. Jimenez, *J. Phys. Chem. B* **2008**, *112*, 14819.

[53] M. Naffakh, Z. Martin, N. Fanegas, C. Marco, M. A. Gomez, I. Jimenez, *J. Polym. Sci. Part B: Polym. Phys.* **2007**, *45*, 2309.

[54] X. Hou, C. X. Shan, K. -L. Choy, *Surf. Coat. Technol.* **2008**, *202*, 2287.

[55] M. Schneider, H. Dodiuk, S. Kenig, R. Tenne, *J. Adhes. Sci. Tech.*, in press.

[56] (a) R. Prins, *Adv. Catal.* **2002**, *46*, 399; (b) C. T. Tye, K. J. Smith, *Top. Catal.* **2006**, *37*, 129.

[57] (a) J. V. Lauritsen, M. Nyberg, J. K. Nørskov, B. S. Clausen, H. Topsøe, E. Lægsgaard, F. Besenbacher, *J. Catal.* **2004**, *224*, 94; (b) J. V. Lauritsen, M. V. Bollinger, E. Lægsgaard, K. W. Jacobsen, J. K. Nørskov, B. S. Clausen, H. Topsøe, F. Besenbacher, *J. Catal.* **2004**, *221*, 510; (c) J. V. Lauritsen, M. Nyberg, R. T. Vang, M. V. Bollinger, B. S. Clausen, H. Topsøe, K. W. Jacobsen, E. Lægsgaard, J. K. Nørskov, F. Besenbacher, *Nanotechnology* **2003**, *14*, 385.

[58] N. A. Dhas, K. S. Suslick, *J. Am. Chem. Soc.* **2005**, *127*, 2368.

[59] (a) J. Chen, S. L. Li, Q. Xu, K. Tanaka, *Chem. Commun.* **2002**, 1722; (b) F. Cheng, X. Gou, J. Chen, Q. Xu, *Adv. Mater.* **2006**, *18*, 2561.

[60] R. Tenne, *Adv. Mater.* **1995**, *7*, 965.

[61] I. Alexandrou, N. Sano, A. Burrows, R. R. Meyer, H. Wang, A. I. Kirkland, C, J Kiely, G. A. J. Amaratunga, *Nanotechnology* **2003**, *14*, 913.

[62] J. J. Hu, J. E. Bultman, J. S. Zabinski, *Tribol. Lett.* **2004**, *17*, 543.

[63] G. A. Camacho-Bragado, J. L. Elechiguerra, A. Olivas, S. Fuentes, D. Galvan, M. J. Yacaman, *J. Catal.* **2005**, *234*, 182.

[64] W. X. Chen, J. P. Tu, X. C. Ma, Z. D. Xu, R. Tenne, R. Rosentsveig, *Chin. Chem. Lett.* **2003**, *14*, 312.

[65] Y. Feldman, G. L. Frey, M. Homyonfer, V. Lyakhovitskaya, L. Margulis, H. Cohen, G. Hodes, J. L. Hutchison, R. Tenne, *J. Am. Chem. Soc.* **1996**, *118*, 5362.

[66] Y. Feldman, L. Margulis, M. Homyonfer, R. Tenne, *High Temp. Mater. Proc.* **1996**, *15*, 163.

[67] Y. Feldman, A. Zak, R. Popovitz-Biro, R. Tenne, *Solid State Sci.* **2000**, *2*, 663.

[68] A. Zak, Y. Feldman, V. Alperovich, R. Rosentsveig, R. Tenne, *J. Am. Chem. Soc.* **2000**, *122*, 11108.

[69] X. L. Li, Y. D. Li, *Chem. Eur. J.* **2003**, *9*, 2726.

[70] A. Rothschild, R. Tenne, J. Sloan, A. P. E. York, M. L. H. Green, J. Sloan, J. L. Hutchison, *Chem. Commun.* **1999**, 363.

[71] T. Tsirlina, Y. Feldman, M. Homyonfer, J. Sloan, J. L. Hutchison, R. Tenne, *Fullerene Sci. Technol.* **1998**, *6*, 157.

[72] R. L. D. Whitby, W. K. Hsu, T. H. Lee, C. B. Boothroyd, H. W. Kroto, D. R. M. Walton, *Chem. Phys. Lett.* **2002**, *359*, 68.

[73] K. S. Coleman, J. Sloan, N. A. Hanson, G. Brown, G. P. Clancy, M. Terrones, H. Terrones, M. L. H. Green, *J. Am. Chem. Soc.* **2002**, *124*, 11580.

[74] A. Margolin, R. Popovitz-Biro, A. Albu-Yaron, A. Moshkovich, L. Rapoport, R. Tenne, *Curr. Nanosci.* **2005**, *1*, 253.

[75] C. Schuffenhauer, R. Popovitz-Biro, R. Tenne, *J. Mater. Chem.* **2002**, *12*, 1587.

[76] G. H. Lee, J. W. Jeong, S. H. Huh, S. H. Kim, B. J. Choi, Y. W. Kim, *Int. J. Mod. Phys. B* **2003**, *17*, 1134.

[77] C. M. Zelenski, P. K. Dorhout, *J. Am. Chem. Soc.* **1998**, *120*, 734.

[78] J. Chen, S. L. Li, F. Gao, Z. L. Tao, *Chem. Mater.* **2003**, *15*, 1012.

[79] M. Nath, A. Govindaraj, C. N. R. Rao, *Adv. Mater.* **2001**, *13*, 283.

[80] M. Nath, C. N. R. Rao, *Dalton Trans.* **2003**, 1.

[81] M. Remskar, A. Mrzel, Z. Skraba, A. Jesih, M. Ceh, J. Demsar, P. Stadelmann, F. Levy, D. Mihailovic, *Science* **2001**, *292*, 479.

[82] M. Remskar, Z. Skraba, M. Regula, C. Ballif, R. Sanjines, F. Levy, *Adv. Mater.* **1998**, *10*, 246.

[83] P. A. Parilla, A. C. Dillon, B. A. Parkinson, K. M. Jones, J. Alleman, G. Riker, D. S. Ginley, M. J. Heben, *J. Phys. Chem. B* **2004**, *108*, 6197.

[84] Y. R. Hacohen, R. Popovitz-Biro, Y. Prior, S. Gemming, G. Seifert, R. Tenne, *Phys. Chem. Chem. Phys.* **2003**, *5*, 1644.

[85] R. Sen, A. Govindaraj, K. Suenaga, S. Suzuki, H. Kataura, S. Iijima, Y. Achiba, *Chem. Phys. Lett.* **2001**, *340*, 242.

[86] C. Schuffenhauer, B. A. Parkinson, N. Y. Jin-Phillipp, L. Joly-Pottuz, J. M. Martin, R. Popovitz-Biro, R. Tenne, *Small* **2005**, *1*, 1100.

[87] D. Vollath, D. V. Szabo, *Mater. Lett.* **1998**, *35*, 236.

[88] D. Vollath, D. V. Szabo, *Acta Mater.* **2000**, *48*, 953.

[89] X. L. Li, J. P. Ge, Y. D. Li, *Chem. Eur. J.* **2004**, *10*, 6163.

[90] S. Bastide, D. Duphil, J. P. Borra, C. Levy-Clement, *Adv. Mater.* **2006**, *18*, 106.

[91] J. Etzkorn, H. A. Therese, F. Rocker, N. Zink, U. Kolb, W. Tremel, *Adv. Mater.* **2005**, *17*, 2372.

[92] N. Zink, J. Pansiot, J. Kieffer, H. A. Therese, M. Panthöfer, F. Rocker, U. Kolb, W. Tremel, *Chem. Mater.* **2007**, *19*, 6391.

[93] (a) A. Yella, H. A. Therese, N. Zink, M. Panthöfer, W. Tremel, *Chem. Mater.* **2008**, *20*, 3587; (b) J. Tannous, F. Dassenoy, A. Bruhács, W. Tremel, *Tribol. Lett.* **2010**, *37*, 83.

[94] A. Yella, M. Panthöfer, M. Kappl, W. Tremel, *Angew. Chem.* **2010**, *122*, 2629; *Angew. Chem., Int. Ed.* **2010**, *49*, 2575.

[95] M. S. Gudiksen, C. M. Lieber, *J. Am. Chem. Soc.* **2000**, *122*, 8801.

[96] F. Hulliger, *Physics and Chemistry of Materials with Layered Structures*, Vol. 5, edited by F. Lévy, Dordrecht, 1977.

[97] A. Yella, E. Mugnaioli, H. A. Therese, M. Panthöfer, U. Kolb, W. Tremel, *Chem. Mater.* **2009**, *21*, 2474.

[98] A. Yella, E. Mugnaioli, M. Panthöfer, H. A. Therese, U. Kolb, W. Tremel, *Angew. Chem.* **2009**, *121*, 6546; *Angew. Chem., Int. Ed.* **2009**, *48*, 6426.

[99] H. A. Therese, J. Li, U. Kolb, W. Tremel, *Solid State Sci.* **2005**, *7*, 67.

[100] A. Rothschild, G. L. Frey, M. Homyonfer, R. Tenne, M. Rappaport, *Mater. Res. Innovation* **1999**, *3*, 145.

[101] A. Rothschild, J. Sloan, R. Tenne, *J. Am. Chem. Soc.* **2000**, *122*, 5169.

[102] (a) H. A. Therese, F. Rocker, A. Reiber, J. Li, M. Stepputat, G. Glasser, U. Kolb, W. Tremel, *Angew. Chem., Int. Ed.* **2005**, *44*, 262. The bulk materials are described in: (b) G. A. Wiegers, R. van der Meer, H. van Heiningen, H. J. Kloosterboer, A. J. A. Albernik, *Mater. Res. Bull.* **1974**, *9*, 1261; (c) L. F. Schneemeyer, A. Stacy, M. J. Sienko, *Inorg. Chem.* **1980**, *19*, 2659; (d) D. W. Murphy, F. J. DiSalvo, G. W. Hull, J. V. Waszczak, *Inorg. Chem.* **1976**, *15*, 17.

[103] A. Yella, E. Mugnaioli, M. Panthöfer, U. Kolb, W. Tremel, *Angew. Chem.* **2010**, *49*, 3301.

[104] A. K. Geim, K. S. Novoselov, *Nature Mater.* **2007**, *6*, 183.

[105] D. Li, R. B. Kaner, *Science* **2008**, *320*, 1170.

[106] M. I. Katsnelson, *Materials Today* **2007**, *10*, 20.

[107] C. N. R. Rao, K. Biswas, K. S. Subrahmanyam, A. Govindaraj, *J. Mater. Chem.* **2009**, *19*, 2457.

[108] C. N. R. Rao, A. K. Sood, K. S. Subrahmanyam, A. Govindaraj, *Angew. Chem. Int. Ed.* **2009**, *48*, 7752.

[109] C. N. R. Rao, A. K. Sood, R. Voggu, K. S. Subrahmanyam, *J. Phys. Chem. Lett.* **2010**, *1*, 572.

[110] K. S. Novoselov, A. K. Geim, S. V. Morozov, D. Jiang, M. I. Katsnelson, I. V. Grigorieva, S. V. Dubonos, A. A. Firsov, *Nature* **2005**, *438*, 197.

[111] Y. Zhang, J. W. Tan, H. L. Stormer, P. Kim, *Nature* **2005**, *438*, 201.

[112] K. S. Novoselov, Z. Jiang, Y. Zhang, S. V. Morozov, H. L. Stormer, U. Zeitler, J. C. Maan, G. S. Boebinger, P. Kim, A. K. Geim, *Science* **2007**, *315*, 1379.

[113] K. S. Novoselov, A. K. Geim, S. V. Morozov, D. Jiang, Y. Zhang, S. V. Dubonos, I. V. Grigorieva, A. A. Firsov, *Science* **2004**, *306*, 666.

[114] M. Y. Han, B. Oezyilmaz, Y. Zhang, P. Kim, *Phys. Rev. Lett.* **2007**, *98*, 206805.

[115] C. Lee, X. Wei, J. W. Kysar, J. Hone, *Science* **2008**, *321*, 385.

[116] S. Park, R. S. Ruoff, *Nature Nanotech.* **2009**, *4*, 217.

[117] K. S. Novoselov, D. Jiang, F. Schedin, T. J. Booth, V. V. Khotkevich, S. V. Morozov, A. K. Geim, *Proc. Natl. Acad. Sci. USA* **2005**, *102*, 10451.

[118] P. Joensen, R. F. Frindt, S. R. Morrison, *Mater. Res. Bull.* **1986**, *21*, 457.

[119] B. K. Miremadi, S. R. Morrison, *J. Appl. Phys.* **1988**, *63*, 4970.

[120] D. Yang, R. F. Frindt, *J. Phys. Chem. Solids* **1996**, *57*, 1113.

[121] Y. Tian, Y. He, Y. Zhu, *Mater. Chem. Phys.* **2004**, *87*, 87.

[122] H. S. S. R. Matte, A. Gomathi, A. K. Manna, D. J. Late, R. Datta, S. K. Pati, C. N. R. Rao, *Angew. Chem. Int. Ed.* **2010**, *49*, 4059.

[123] A. Nag, K. Raidongia, K. P. S. S. Hembram, R. Datta, U. V. Waghmare, C. N. R. Rao, *ACS Nano* **2010**, *4*, 1539.

[124] A. K. Geim, *Science* **2009**, *324*, 1530.

[125] B. Poudel, Q. Hao, Y. Ma, A. Muto, M. S. Dresselhaus, Y. Lan, D. Vashaee, G. Chen, A. Minnich, X. Chen, Z. Ren, *Science* **2008**, 320, 634.

[126] A. Splendi ani et al., *Nano Lett.* **2010**, *10*, 1271.

[127] K. S. Novoselov, D. Jiang, F. Schedin, T. J. Booth, V. V. Khotkevich, S. V. Morozov, A. K. Geim, *Proc. Natl. Acad. Sci. USA* **2005**, *102*, 10451.

[128] A. Ayari, E. Cobas, O. Ogundadegbe, M. S. Fuhrer, *J. Appl. Phys.* **2007**, *101* , 014507.

[129] R. Ruoff, *Nature Nanotech.* **2008**, *3*, 10.

[130] P. Joensen, R. F. Fr indt, S. R. Morrison, *Mater. Res. Bull.* **1986**, *21*, 457.

[131] C. Liu, O. Sin gh, P. Joensen, A. E. Curzon , R. F. Frindt, *Thin Solid Films* **1984**, *113* , 165.

[132] H. S. S. R. Matte, A. Gomathi, A. K. Manna, D. J. Late, R. Datta, S. K. Pati, C. N. R. Rao, *Angew. Chem. Int. Ed.* **2010**, *49*, 4059.

[133] J. N. Coleman, M. Lotya, A. O'Neill, S. D. Bergin, P. J. King, U. Khan, K. Young, A. Gaucher, S. De, R. J. Smith, I. V. Shvets, S. K. Arora, G. Stanton, H -Y. Kim, K. Lee, G. T. Kim, G. S. Duesberg, T. Hallam, J. J. Boland, J. J. Wang, J. F. Donegan, J. C. Grunlan, G. Moriatry, A. Shmeliov, R. J. Nicholls, J. M. Perkins, E. M. Grieveson, K. Theuwissen, D. W. McComb, P. D. Nellist, V. Nicolosi, *Science* **2011**, *331*, 568.

[134] Y. Hernandez, V. Nicolosi, M. Lotya, F. M. Blighe, Z. Y. Sun, S. De, I. T. McGovern, B. Holland, M. Byrne, Y. K. Gun'ko, J. J. Boland, P. Niraj, G. Duesberg, S. Krishnamurthy, R. Goodhue, J. Hutchison, V. Scardaci, A. C. Ferrari, J. N. Coleman, *Nature Nanotech.* **2008**, *3*, 563.

[135] S. D. Bergin V. Nicolosi, P. V. Streich, S. Giordani, Z. Sun, A. H. Windle, P. Ryan, N. P. P. Niraj, Z. -T. T. Wang, L. Carpenter, W. J. Blau, J. J. Boland, J. P. Hamilton, J. N. Coleman, *Adv. Mater.* **2008,** *20*, 1876.

[136] S. D. Bergin, Z. Sun, D. Rickard, P. V. Streich, J. P. Hamilton, J. N. Coleman, *ACS Nano* **2009**, *3*, 2340.

[137] R. Bissessur, M. G. Kanatzidis, J. L. Schindler, C. R. Kannewurf, *J. Chem. Soc. Chem. Commun.* **1993**, , 1582.

[138] R. A. Gordon, D. Yang, E. D. Crozier, D. T. Jiang, R. F. Frindt, *Phys. Rev. B* **2002**, *65*, 125407.

[139] C. Lee, H. Yan, L. E. Brus, T. F. Heinz, J. Hone, S. Ryu, *ACS Nano* **2010**, *4*, 2695.

[140] F. Kopnov, Y. Feldman, R. Popovitz-Biro, A. Vilan, H. Cohen, A. Zak, R. Tenne, *Chem. Mater.* **2008**, *20*, 4099.

Diffusion-Driven Formation of MoS_2 Nanotube Bundles Containing MoS_2 Nanopods

Associated publication: *Chem. Mater.*, **2011**, *23*, 4718-4720

2.1. Introduction

The discovery of carbon nanotubes has opened a completely new chapter in the field of novel carbon materials [1]. In analogy with carbon nanotubes, it has been anticipated that other two dimensional (2D) layered compounds can be "rolled up" to form fullerene-like structures, including tubes, scrolls, and onions [2]. The first inorganic (WS_2) nanotubes were synthesized in 1992 [3]. Since that time, a handful of other mesoscopic metal dichalcogenides (TiS_2 [4], SnS_2 [5], VS_2 [6], MoS_2 [7]) have been investigated as hollow closed structures of 2D layered materials. In particular, WS_2 and MoS_2 nanoparticles have shown important applications as solid lubricants [8], photovoltaic film [9], catalysts [10], super shock absorbers [11], etc. Various approaches to other materials forming nanotubes, such as $NiCl_2$ [11], $Ni(OH)_2$ [12], $In(OH)_3$ [13], or V_2O_5 [14] have been reported, which implies that, generally, substances crystallizing in layered structures may form nanotubes under favorable conditions.

Tenne *et al.* [15] were the first to report the production of macroscopic quantities of fullerene-like MoS_2 nanotubes via the gas-phase reaction between MoO_{3-x} and H_2S in a reducing atmosphere at elevated temperatures (800-950 ºC). Subsequently, the reaction mechanisms associated with particle formation were studied extensively [16]. Dorhout *et al.* [7a] used relatively low temperatures (~400 ºC) for annealing ammonium thiomolybdate within an alumina template. MoS_2 nanotubes with poor crystallinity were obtained, while the high-temperature approach (~1300 ºC) of Rao's group [7c] led to the formation of well-ordered tubes, but only in very low yields. Remskar and co-workers obtained MoS_2 nanotubes by chemical transport [7d]. Ghosh *et al.* showed the synthesis of honeycomb-like MoS_x nanoporous/mesoporous layer structures via the electrochemical deposition of MoS_x nanoplates from aqueous solutions on NiP and CoW substrates and subsequent annealing [7e]. Numerous new types of nanotubes and nanoparticles have been synthesized in recent years. Among them, the synthesis of core-shell nanotubes, such as $PbI_2@WS_2$ [17], the so-called "MoS_2 mama-tubes" [18], and others have been described. The synthesis of macroscopic amounts of INT-WS_2, using a fluidized-bed reactor, has been reported recently [19]. According to atomic force microscopy (AFM) investigations assisted by density functional-based tight binding (DFTB) calculations, individual WS_2 nanotubes exhibit a Young modulus of ~150-170 GPa and a tensile strength of 16 GPa [20].

The synthetic challenge in the synthesis of MoS_2 hollow nanoparticles such as nanotubes and nested fullerenes is that they are high-temperature and low-pressure phases which are not accessible via traditional solid-state routes. In conventional high temperature reactions, the

energy required for the solid-state diffusion of the reactants would exceed the nucleation energy of the metastable MoS_2 nanoparticles. A consequence of these bulk reactions is that only the thermodynamically stable final phase (*i.e.*, 2H-MoS_2) is obtained. In contrast, reactions in which solid state diffusion plays only a minor role are kinetically controlled [21]. Therefore, a metastable phase may nucleate and grow until its growth exhausts the supply of the reactants. The sequence of phases formed is dependent upon the relative activation energies for the nucleation of various compounds, and compounds in the equilibrium phase diagram may be temporarily skipped if they have a large activation energy for nucleation. In fact, all synthetic approaches to hollow chalcogenide nanoparticles rely on circumventing the solid-state diffusion step [22].

Our approach to bypass solid-state diffusion as a rate-determining step is based on a gas-phase reaction. In some recent contributions, the gas-phase synthesis of MS_2 (M = Sn, Mo, W, Re) nested particles was reported with the aid of a metal organic chemical vapor deposition (MOCVD)-based reaction [23]. In a first step, amorphous chalcogenide nanoparticles were formed in a gas-phase reaction from the precursors $Mo(CO)_6$ and sulfur or selenium, respectively. Annealing of these amorphous nanoparticles at moderate temperature leads to the formation of nested fullerene species. Attempts to enhance the atom mobility through surface diffusion by adding iodine as a mineralizing agent in this MOCVD reaction lead to the formation of partially amorphous primary structures with micrometer-scale dimensions. Upon annealing of these primary Mo/S/I particles, radially oriented arrays of hollow nanotubes containing nested structures in a peapod-like fashion were formed.

2.2. Experimental Section

2.2.1. Synthesis of MoS_2 Nanotubes

The reaction was carried out in a three-zone horizontal tube furnace. Five hundred milligrams (500 mg) of $Mo(CO)_6$ were weighed inside the glovebox and was transferred outside the box in a corundum boat in an argon filled chamber. Typically, 1000 mg of iodine was weighed and mixed with molybdenum carbonyl immediately before starting the reaction. Prior to the synthesis, the setup was flushed with argon for at least 30 min. Subsequently, the corundum boat was placed into a glass tube with an inner diameter of 15 mm, and the glass tube was placed in the upstream end of a reaction tube of an outer diameter of 35 mm inside a three-zone horizontal furnace. Argon was flushed through this setup for another half hour. The three zones were then heated to 550 ºC at a rate of 10 ºC/min. When the temperature

reached to 550 ºC, the boat was moved to the center of the furnace and the setup was flushed with H_2S for 1 h. After the heating step, the temperature was decreased to room temperature with the rate of 10 ºC/min under argon and the product was collected with a spatula from the outer wall of the small and the inner wall of the bigger glass tubes.

Thermal Annealing. The collected material was subjected to thermal annealing in a conventional tube furnace. The annealing was performed by transferring the sample from the first step into a corundum boat and placing it in the middle of a horizontal tube furnace at a temperature of 850 ºC with a heating rate of 5 ºC/min under constant argon gas flow of 100 sccm for 1 h. To see how the annealing temperature affects the composition and the morphology of final product, annealing was performed at temperatures of 750º, 800º, and 900 ºC as well, and the products were used for further characterizations.

2.2.2. Material Characterization

X-ray Powder Diffraction. X-ray diffraction (XRD) patterns were recorded using a Siemens Model D5000 diffractometer that was equipped with a Braun Model M50 position-sensitive detector in transmission mode using Ge (200) monochromatized Cu K_α radiation. Samples were prepared between two layers of cellophane tape. Crystalline phases were identified according to the PDF-2 database, using Bruker AXS EVA 10.0 software.

Electron Microscopy. The product was characterized using high-resolution scanning electron microscopy (HRSEM) (LEO Model 1530 field-emission scanning electron microscopy (SEM) system, 6 kV extraction voltages). Transmission electron microscopy (TEM) was carried out on a Philips Model EM420 instrument with a twin lens and a Philips Model CM12 instrument with a twin lens at an acceleration voltage of 120 kV. High-resolution images were taken with a Philips Model FEI TECNAI F30 ST electron microscopy system (field-emission gun, 300 kV extraction voltages) that was equipped with an Oxford EDX (energy-dispersive X-ray) spectrometer with a Si/Li detector and an ultrathin window for elemental analysis. Samples for TEM studies were prepared from ethanolic suspensions of the samples. Three drops of the sonicated suspension were administered onto a copper grid that was coated with an amorphous carbon layer.

2.3. Results and Discussion

The powder XRD patterns of the product obtained after the first step and after annealing are shown in Figure 2-1a. The diffraction pattern of the primary product could be assigned to I_2

(PDF-2 File Card No. 43-0304) and 2H-MoS_2 (PDF-2 File Card No. 37-1492). The product obtained after annealing showed a high degree of crystallinity, and most of the reflections could be assigned to 2H-MoS_2 and an impurity of $Mo_2S_5I_3$ (PDF-2 File Card No. 39-0717). This impurity phase is marked with an asterisk in Figure 2-1b.

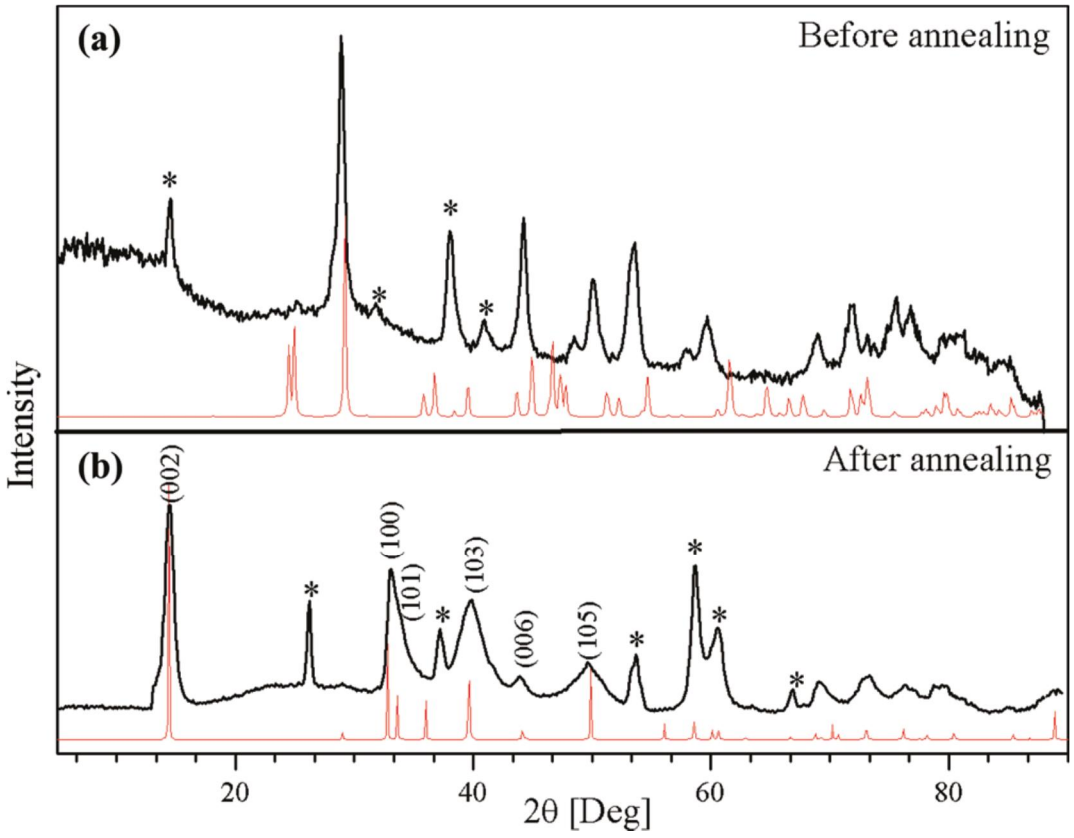

Figure 2-1. (a) Powder X-ray diffraction (XRD) pattern of the primary product obtained from the reaction of $Mo(CO)_6$, I_2, and H_2S/Ar at 550 ºC; the red trace line indicates I_2 (PDF-2 File Card No. 43-0304). (b) Powder XRD pattern of the primary product after annealing at 850 ºC; the red line corresponds to 2H-MoS_2 (PDF-2 File Card No. 37-1492), and the asterisks indicate reflections from $Mo_2S_5I_3$ (PDF-2 File Card No. 39-0717).

The primary product obtained after the first reaction step was characterized using SEM and TEM. The SEM image in Figure 2-2a shows that the product obtained at 550 ºC consisted mainly of microspheres with diameters of ~1-2 μm and some 2D flat nanostructures with a common origin and branches with a typical length of 5-8 μm (marked with a red square in Figure 2-2a). The magnified SEM image of the microspheres (Figure 2-2b) also shows branches emanating from a common origin. The high-resolution (HR) image in Figure 2-2c reveals the individual MoS_2 branches to have average diameters of ~50 nm. The branch substructures of the microspheres were found to be solid with a smooth surface, whereas the

branches of the 2D flat nanostructures were consistently open-ended (Figure 2-2d) with porous walls.

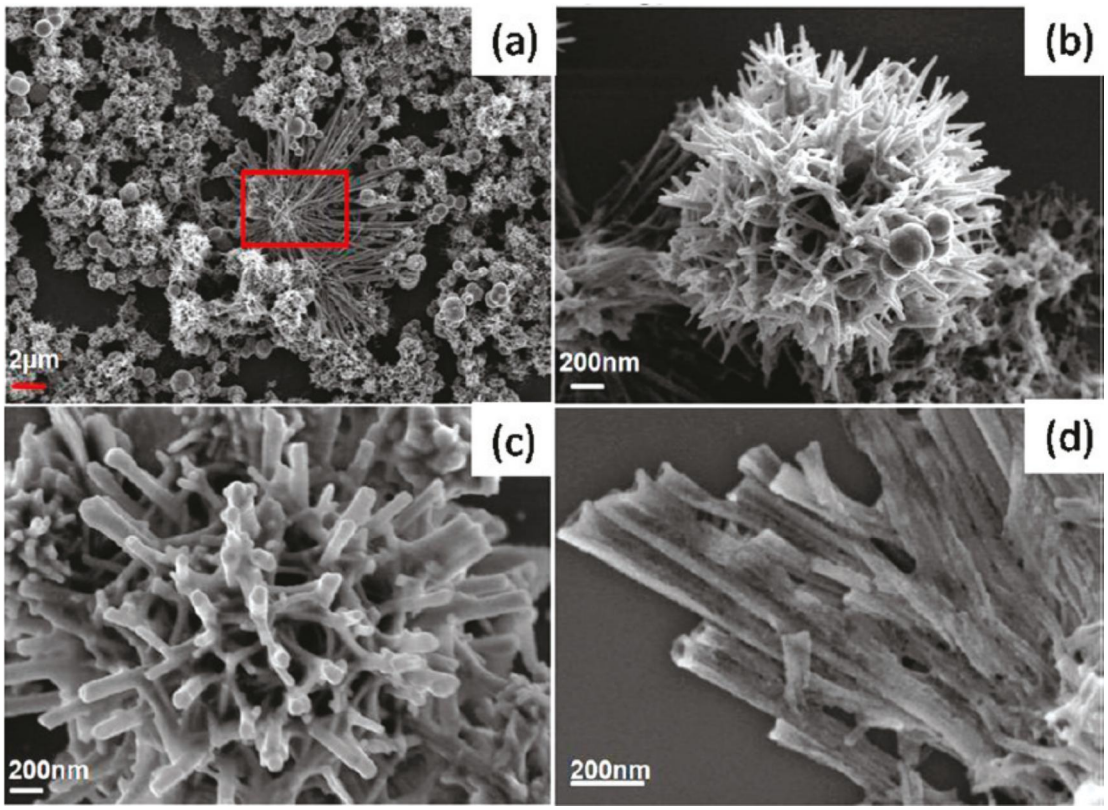

Figure 2-2. SEM images of the product obtained after the first step. (a) Overview SEM image of the product. The 2D branched nanostructures are marked by a red rectangle. (b) Magnified image of the microspheres showing branched MoS_2 nanowires emanating from the center. (c) High-resolution (HR) image showing the branched nanowires in a top view. (d) HR image of the branched 2D nanostructures with open-ended tips and porous walls.

The product was further characterized by a combined TEM/EDX analysis. Figure 2-3a shows a typical TEM image of one individual MoS_2 microsphere nanostructure, which indicates that the MoS_2 nanotubes emanating from the center are straight with relatively uniform diameters over their entire length (average length of ~400 nm). The tubular morphology of the MoS_2 nanostructure is clearly visible at the open ends. The sample released iodine under high vacuum conditions in the TEM system, which presumably results in the formation of an open-ended tube structure under in situ conditions. The particles attached to the outer walls of the tubes were formed under high vacuum, probably because of the release of iodine. The branched microsphere-type structures were stable even after long periods of ultrasonic treatment. This indicates their robustness, while the 2D branched nanostructures were less

stable upon sonication, as shown in Figure 2-3b. HRTEM analysis shows that the product was completely amorphous.

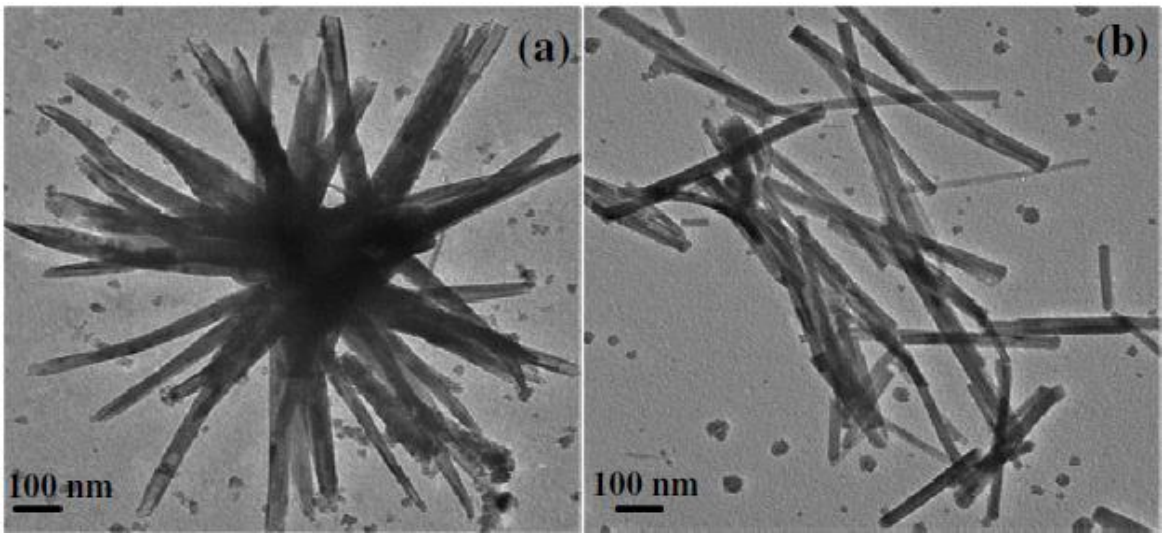

Figure 2-3. TEM images of the product obtained after the first step. (a) a single bundle which is stable after long ultrasonic treatment, (b) 2D branched nanostructures after the ultrasonic treatment.

Annealing of the product was carried out at 850 ºC under argon, and, after annealing, a highly crystalline product was obtained. Most of the reflections in the powder pattern could be assigned readily to 2H-MoS_2. The reflections marked with an asterisk could be assigned to $Mo_2S_5I_3$ [24].

Figure 2-4 shows TEM and HRTEM images of the product obtained after annealing. The SEM images (see Figure 2-5) resemble those of the product before annealing. However, the TEM images clearly show that, after annealing, the tubular 1D nanowires emanating from the microspheres became crystalline and transformed to nanotubes. Most tips of the tubes were closed, and some of the tubes were filled with some particles (in the middle of the tube) bearing resemblance to a "peapod-like" structure, as shown in Figure 3b. The HRTEM image in Figure 2-4c shows the closed tip of a MoS_2 nanotube. The interlayer spacing of 0.63 nm between the layers in the nanotubes is slightly larger than the (002) d-spacing of 2H-MoS_2. The "peapod-like" nanotubes were found to be quite unstable under the intense electron beam, and the fullerene-like particles (see Figures 2-4e and 4f) inside were found to open up under the beam to form bent aggregates of sheets.

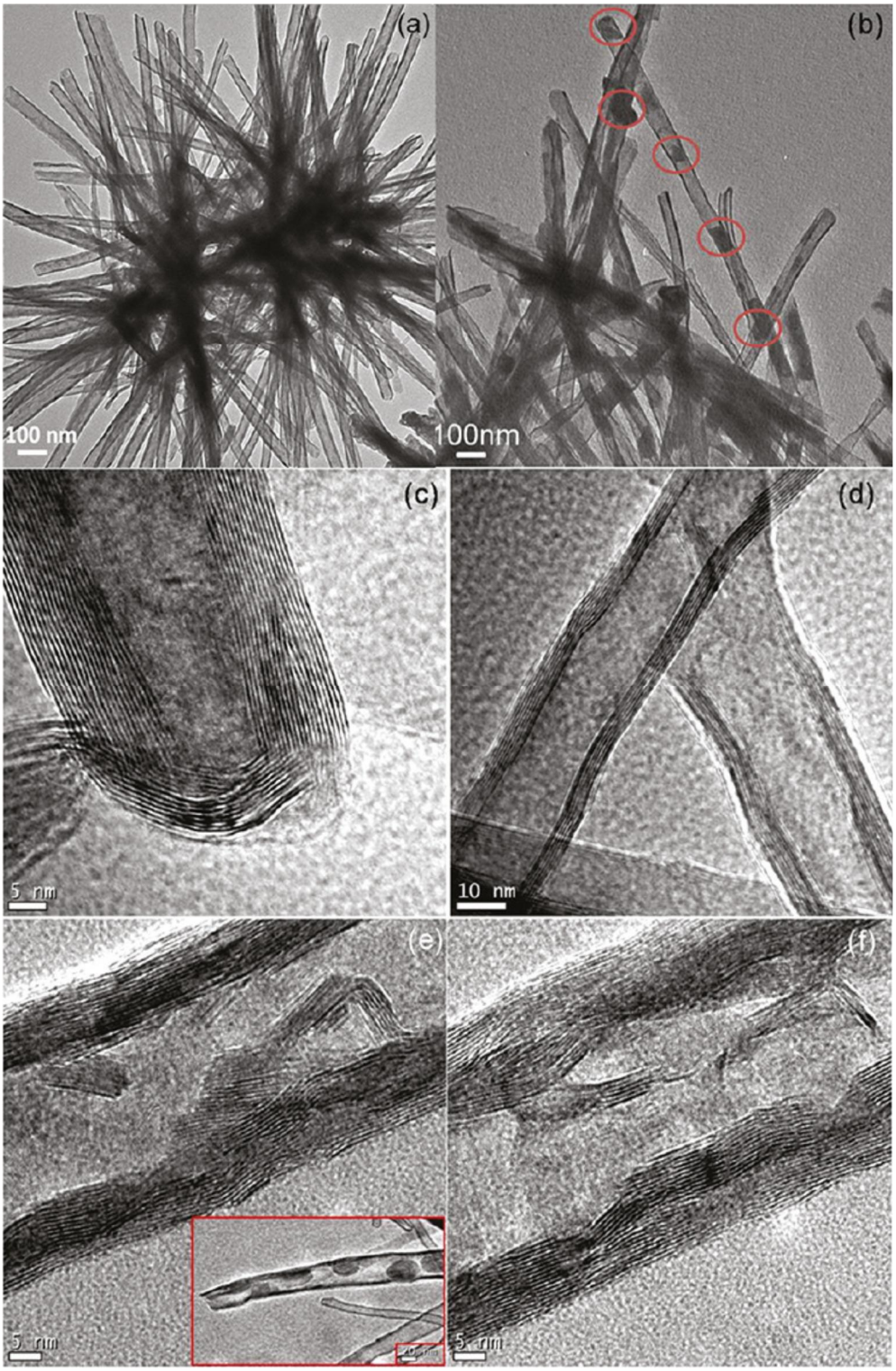

Figure 2-4. TEM images of the product obtained after annealing ((a) TEM image of a single microsphere, showing the nanotubes emanating from the center in a radial manner; (b) TEM image showing the ends of the microsphere with a peapod-like structure). HRTEM images of the product obtained after annealing ((c) closed-end nanotube, (d) openended nanotube, (e) peapod-like structure with nested fullerenes inside the nanotubes, and (f) a "burst" fullerene under the beam).

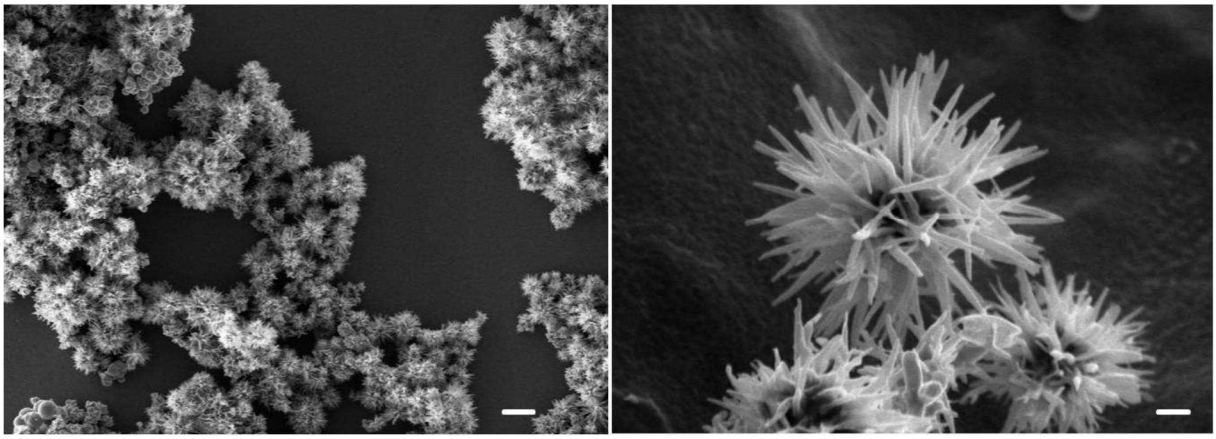

Figure 2-5. SEM images of the product obtained after the annealing at 850°C in Ar for 1 h. (a) SEM Overview of MoS_2 nanotube bundle aggregates and (b) HRSEM image of a single nanotube bundle.

In order to investigate how the annealing temperature affects the structure and morphology of MoS_2 nanotubes, thermal annealing of the product was carried out at 750, 800, and 900 ºC. Annealing at lower temperature of 750 ºC in argon resulted in the formation of tubes with more defects, as seen from the TEM and HRTEM image in Figure 2-6a, 6b and 6c. At 800 ºC, the formation of the "peapod-like" nanotubes is observed, as shown in Figure 2-6d, and the nanotubes have still defects, in comparison to those obtained at 850 ºC. Annealing at an elevated temperature (900 ºC) resulted in complete collapse of the nanotubes (see Figure 2-6e) and an elemental molybdenum residue was observed, according to phase analysis from powder XRD. The reaction was also performed at lower temperatures (*i.e.*, 350 and 450 ºC) and the product obtained was annealed at 850 ºC under an argon atmosphere. The TEM images of the product obtained at 350 ºC are shown in Figure 2-7a. The "cookie-like" structures seem to be spherical analogues of the "peapod-like" nanotubes. At 450 ºC, the branches of the nanotube bundles are about to emerge (see Figure 2-7b and 7c). EDX analysis of the product obtained after annealing showed the presence of MoS_2, along with a small amount of iodine, which is consistent with the powder diffraction pattern.

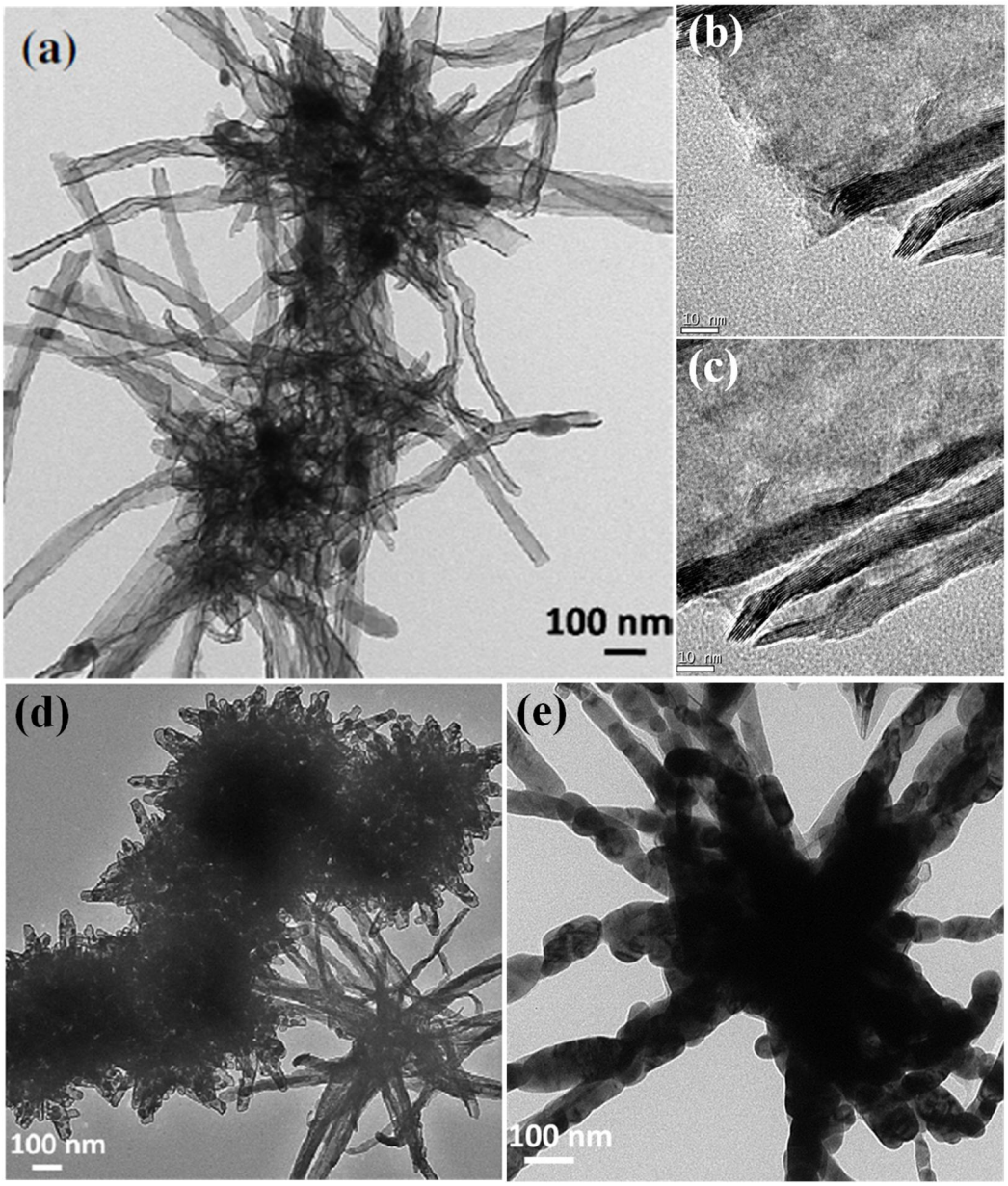

Figure 2-6. (a) TEM overview image of the product obtained at the annealing temperature of 750°C. (b), (c) HRTEM image of as-synthesized nanotubes (The tubes were found to have more defects compared to those obtained at 850°C), (d) TEM image of the product obtained at the annealing temperature of 800°C and (e) 900°C.

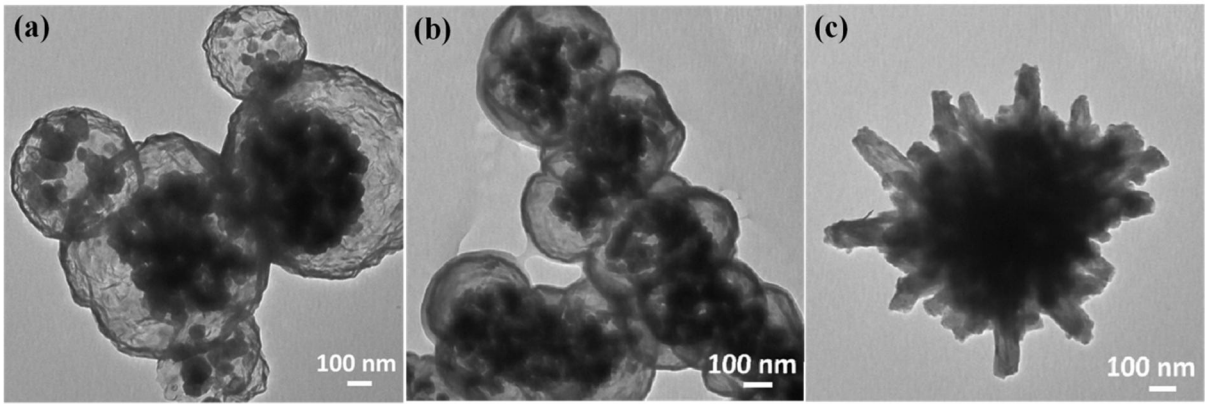

Figure 2-7. TEM image of the product obtained at the reaction temperature of (a) 350°C and (b), (c) 450°C.

In order to determine the role of iodine, the reaction was carried out in the absence of iodine, using only $Mo(CO)_6$ and H_2S as precursors. The SEM images of the product obtained in the absence of iodine are shown in Figure 2-8. The product now contained exclusively spherical particles that, in turn, were aggregates of smaller particles. Hence, the formation of the microspheres might be caused by the thermal decomposition of the amorphous Mo-S-I precursor, which leads to an outward diffusion flow of iodine (as indicated by the second arrow in Scheme 2-1) via the formation of hollow tubes upon annealing.

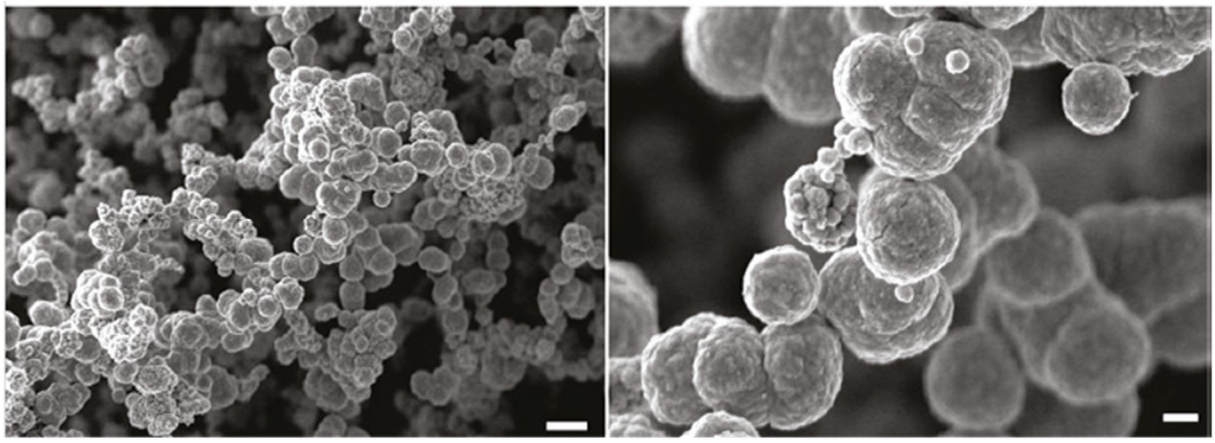

Figure 2-8. SEM images of the product obtained without using iodine in the process ((a) overview SEM image showing that the product consists of spherical particles; (b) magnified image showing that the surface is not uniform but rather consists of smaller aggregates).

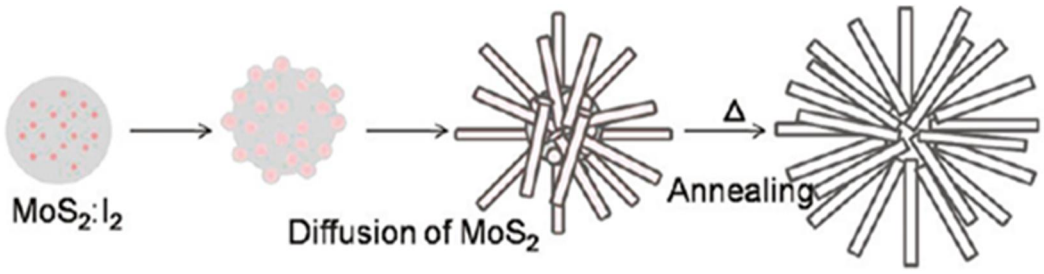

Scheme 2-1. The growth mechanism of MoS_2 nanotube bundles in the presence of iodine.

The fact that the MoS_2 nanotubes grow from a common nucleation point indicates that a MoS_2 "cluster" might occur in the course of the growth process. For the reorganization of the MoS_2 structure and the formation of MoS_2 nanotubes, defect annealing processes seems to play a prominent role. This defect annealing can only proceed smoothly when surface diffusion is rapid enough [25], *i.e.*, at elevated temperatures (T ≈ 850 ºC). In accordance with this interpretation, powder XRD and electron microscopy showed that MoS_2 nanostructures obtained in the presence of iodine are well-crystallized and well-ordered (2H-MoS_2), while those obtained in the absence of iodine do not form hollow structures and display a significantly higher defect density, as seen from the TEM image in Figure 2-9. The use of smaller amounts of iodine decreased the crystallinity of the products (see the SEM image shown in Figure 2-10 for half the amount of iodine), which indicates that ordering by surface diffusion is caused mainly by iodine.

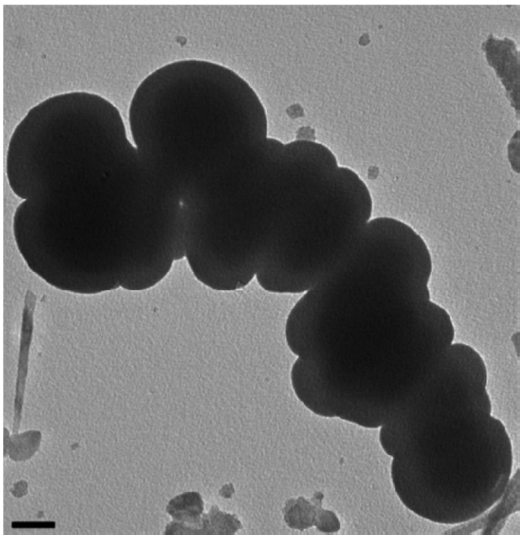

Figure 2-9. TEM image of the product obtained after omitting iodine as precursor.

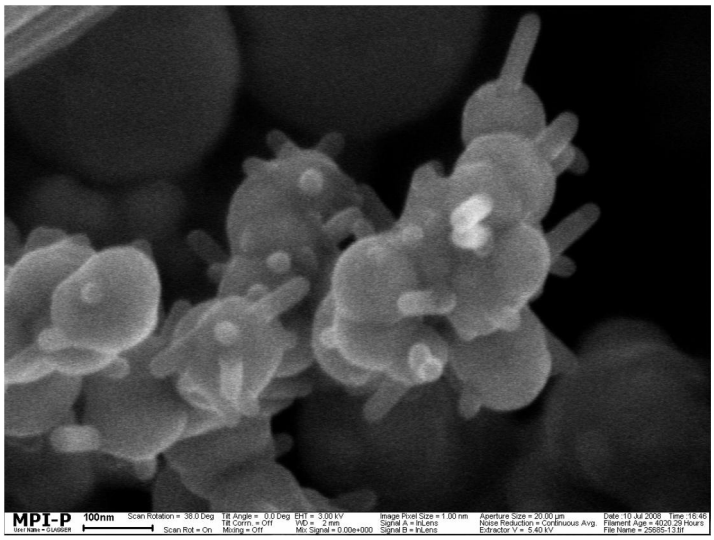

Figure 2-10. SEM image of the product obtained using half the amount of iodine.

The proposed growth mechanism may be contrasted with the vapor_liquid_solid (VLS) growth mechanism for nanorods or nanotubes. In this metal-catalyzed nanorods/tube synthesis, almost monodisperse metal nanoclusters can be used to control the diameter [5, 26] and (through growth time) the length [27] of Group III-V and Group IV semiconductor nanowires [28]. The vapor-phase reactants required for nanorods/tube growth are supplied by an inert carrier gas that provides the required dilution of the reactive vapor-phase species. The metal droplets catalyze the formation of nanorods/tubes by providing a nucleation surface. In principle, this approach can be successfully implemented if a proper catalyst suitable for the growth of the metal chalcogenide can be identified [5]. It is apparent that the nanotubes reported in this work clearly grow via a different mechanism. The chalcogenide nanotubes grow from a “catalytic” metal droplet in an outward direction, and the catalyst remained fixed at the end of the tube.

2.4. Conclusions

In conclusion, we have synthesized MoS_2 nanotube bundles emanating from a common origin in a radial manner. The iodine content of the precursors leads to the formation of a surface film that makes the molybdenum and sulfur atoms mobile, via isothermal chemical transport. The enhanced mobility of the Mo and S constituents aids in the formation of point defects within the MoS_2 layers that are needed to scroll up the inherently instable MoS_2 sheets. In the resulting tubular structures, the number of dangling bonds and, therefore, the total surface energy are decreased. The diffusion flow of the volatile reaction intermediates from the inside of the precursor particles to the outside of the precursor particles leads to the formation of nanotube bundles containing "peapod-like" MoS_2, which are mechanically stable upon sonication. The extension of this new synthesis approach to other layer-structure metal sulfides is subject of ongoing investigations.

2.5. References

[1] (a) S. Iijima, *Nature* **1991**, *354*, 56. (b) M. S. Dresselhaus, G. Dresselhaus, P. C. Eklund, *Science of Fullerenes and Carbon Nanotubes*.: Academic Press: New York, 1996.

[2] (a) W. Tremel, *Angew. Chem.* **1999**, *111*, 2311; *Angew. Chem., Int. Ed.* **1999**, *38*, 2175. (b) G. Patzke, F. Krumeich, R. Nesper, *Angew. Chem.* **2002**, *114*, 2554; *Angew. Chem., Int. Ed.* **2002**, *41*, 2446.

[3] R. Tenne, L. Margulis, M. Genut, G. Hodes, *Nature* **1992**, *360*, 444.

[4] J. Chen, S.-L. Li, Z.-L. Tao, Y.-T. Shen, C.-X. Cui, *J. Am. Chem. Soc.* **2003**, *125*, 5284.

[5] A. Yella, E. Mugnaioli, M. Panthöfer, H. A. Therese, U. Kolb, W. Tremel, *Angew. Chem.* **2009**, *121*, 6546; *Angew. Chem., Int. Ed.* **2009**, *48*, 6426.

[6] H. A. Therese, F. Rocker, A. Reiber, J. Li, M. Stepputat, G. Glasser, U. Kolb, W. Tremel, *Angew. Chem.* **2005**, *117*, 267; *Angew. Chem. Int. Ed.* **2005**, *44*, 262.

[7] (a) C. M. Zelenski, P. Dorhout, *J. Am. Chem. Soc.* **1998**, *120*, 734. (b) J. Chen, N. Kuriyama, H. Yuan, H. T. Takeshita, T. Sakai, *J. Am. Chem. Soc.* **2001**, *123*, 11813. (c) M. Nath, A. Govindaraj, C. N. R. Rao, *Adv. Mater.* **2001**, *13*, 283. (d) M. Remskar, A. Mrzel, M. Virsek, A. Jesih, *Adv. Mater.* **2007**, *19*, 4276. (e) S. K. Ghosh, T. Bera, O. Karacasa, A. Swarnakar, J. G. Buijnsters, J. P. Celis, *Electrochim. Acta* **2011**, *56*, 2433.

[8] (a) L. Rapoport, Y. Bilik, Y. Feldman, M. Homyonfer, S. R. Cohen, R. Tenne, *Nature* **1997**, *387*, 791. (b) L. Rapoport, V. Leshchinsky, Y. Volovik, M. Lvovsky, O. Nepomnyashchy, Y. Feldman, R. Popovitz-Biro, R. Tenne, *Surf. Coat. Technol.* **2003**, *163*, 405.

[9] M. Homyonfer, B. Alperson, Y. Rosenberg, L. Sapir, S. R. Cohen, G. Hodes, R. Tenne, *J. Am. Chem. Soc.* **1997**, *119*, 2693.

[10] (a) Y. Iwata, K. Sato, T. Yoneda, Y. Miki, Y. Sugimoto, A. Nishyima, H. Shimada, *Catal. Today* **1998**, *45*, 353. (b) J. V. Lauritsen, J. Kibsgaard, S. Helveg, H. Topsøe, B. S. Clausen, E. Lægsgaard, F. Besenbacher, *Nat. Nanotechnol.* **2007**, *2*, 53.

[11] Y. R. Hachohen, E. Grunbaum, J. Sloan, J. L. Hutchison, R. Tenne, *Nature* **1998**, *395*, 336.

[12] F.-S. Cai, G.-Y. Zhang, J. Chen, X.-L. Gou, H.-K. Liu, S.-X. Dou, *Angew. Chem.* **2004**, *116*, 4308; *Angew. Chem., Int. Ed.* **2004**, *43*, 4212.

[13] Y. Fang, X. Wen, S. Yang, *Angew. Chem.* **2006**, *118*, 4771; *Angew. Chem. Int. Ed.* **2006**, *45*, 4655.

[14] M. E. Spahr, P. Bitterli, R. Nesper, *Angew. Chem.* **1998**, *110*, 1339; *Angew. Chem., Int. Ed.* **1998**, *37*, 1263.

[15] (a) M. Hershfinkel, L. A. Gheber, V. A. Volterra, J. L. Hutchison, R. Tenne, *J. Am. Chem. Soc.* **1994**, *116*, 1914. (b) Y. Feldman, E. Wasserman, D. J. Srolovitz, R. Tenne, *Science* **1995**, *267*, 222.

[16] A. Rothschild, J. Sloan, R. Tenne, *J. Am. Chem. Soc.* **2000**, *122*, 5169.

[17] R. Kreizman, S.-Y. Hong, J. Sloan, R. Popovitz-Biro, A. Albu-Yaron, G. Tobias, B. Ballesteros, B. G. Davis, M. L. H. Green, R. Tenne, *Angew. Chem.* **2009**, *121*, 1256; *Angew. Chem. Int. Ed.* **2009**, *48*, 1230.

[18] M. Remskar, A. Mrzel, M. Virsek, A. Jesih, *Adv. Mater.* **2007**, *19*, 4276.

[19] A. Zak, L. Sallacan-Ecker, A. Margolin, M. Genut, R. Tenne, *Nano* **2009**, *4*, 91.

[20] (a) I. Kaplan-Ashiri, S. R. Cohen, K. Gartsman, R. Rosentsveig, G. Seifert, R. Tenne, *J. Mater. Res.* **2004**, *19*, 454. (b) I. Kaplan-Ashiri, R. Tenne, *J. Cluster Sci.* **2007**, *18*, 549.

[21] (a) R. Schneidmiller, A. Bentley, M. D. Hornbostel, D. C. Johnson, *J. Am. Chem. Soc.* **1999**, *121*, 3142. (b) M. Noh, D. C. Johnson, *J. Am. Chem. Soc.* **1996**, *118*, 9117. (c) F. R. Harris, S. Standridge, C. Feik, D. C. Johnson, *Angew. Chem.* **2003**, *115*, 5454; *Angew. Chem. Int. Ed.* **2003**, *42*, 5296.

[22] (a) S. Y. Hong, R. Popovitz-Biro, Y. Prior, R. Tenne, *J. Am. Chem. Soc.* **2003**, *125*, 10470. (b) J. M. Gordon, E. A. Katz, D. Feuermann, A. Albu-Yaron, M. Levy, R. Tenne, *J. Mater. Chem.* **2008**, *18*, 458. (c) P. A. Parilla, A. C. Dillon, B. A. Parkinson, K. M. Jones, J. Alleman, G. Riker, D. S. Ginley, M. J. Heben, *J. Phys. Chem. B* **2004**, *108*, 6197.

[23] (a) J. Etzkorn, H. A. Therese, F. Rocker, N. Zink, U. Kolb, W. Tremel, *Adv. Mater.* **2005**, *17*, 2372. (b) N. Zink, J.Pansiot, J. Kieffer, H. A. Therese, M Panthöfer, F. Rocker, U. Kolb, W. Tremel, *Chem. Mater.* **2007**, *19*, 6391. (c) A. Yella, H. A. Therese, N. Zink, M. Panthöfer, W. Tremel, *Chem. Mater.* **2008**, *20*, 3587. (d) A. Yella, E. Mugniaoli, H. A. Therese, M. Panthöfer, W. Tremel, *Chem. Mater.* **2009**, *21*, 2474.

[24] C. Perrin, A. Perrin, J. Prigent, *Bull. Soc. Chim. Fr.* **1972**, *8*, 3086.

[25] H. Schäfer, *Angew. Chem.* **1971**, *83*, 35.

[26] M. S. Gudiksen, C. M. Lieber, *J. Am. Chem. Soc.* **2000**, *122*, 8801.

[27] Y. Cui, L. J. Lauhon, M. S. Gudiksen, J. F. Wang, C. M. Lieber, *Appl. Phys. Lett.* **2001**, *78*, 2214.

[28] R. S. Wagner, *In Whisker Technology*; Wiley-Interscience: New York, 1970; pp 47-119.

The MOCVD Synthesis of WS_2 Nested Fullerenes Revisited: Formation Mechanism of IF-WS_2

Associated publication: *Inorg. Chem.*, **2012**, *submitted*

3.1. Introduction

Inorganic nanomaterials have engendered increasing interest in recent years, and considerable progress in the synthesis of a broad variety of new nanomaterials by novel wet chemical and high temperature methods has been achieved [1]. One class of inorganic nanomaterials that has found more prospective applications is inorganic fullerene-like (IF) nanoparticles and nanotubes (NT) [2] (the prototype representatives being IF-MoS_2 and IF-WS_2 nanoparticles and the respective nanotubes) as well as the corresponding nanoparticles of other layered chalcogenides [3,4].

Due to their particular structure, layered chalcogenides are quasi-two-dimensional (2D) compounds. Layered chalcogenides (M = group 4, 5, 6 or 7 early transition metal, Q = S, Se, Te) crystallize in a quasi-2D layered structure where the metal atom is sandwiched between two anionic planes with strong covalent metal–anion bonds. However, weak van der Waals interactions are responsible for stacking of the molecular sheets into a crystal, which often appears in a platelet-form (deck of cards mode of packing) [5,6]. This stacking can lead to the formation of either hexagonal polymorphs with two or four layers in the unit cell (2H, 4H), rhombohedral polymorphs with three or six layers (3R, 6R) or a trigonal polymorph with one layer (1T) [6,7]. Numerous applications have been demonstrated for the IF-MS_2 nanoparticles (M = Mo and W, in particular), the most prominent one being their use as solid lubricants [8]. A first medical application, the reduced friction in orthodontic wires and braces, was recently demonstrated as well [9]. Other potential applications include use in shock-resistant nanocomposites [10], rechargeable ion batteries [11], or as catalysts [12].

Tenne *et al.* demonstrated the bulk synthesis of fullerene-like WS_2 via a solid-gas-phase reaction between tungsten trioxide powder and H_2S in a reducing atmosphere at elevated temperatures (≥900°C), and the associated formation mechanism was studied [13]. Soon after, the gram quantity synthesis of IF-WS_2 was shown using a fluidized-bed reactor [14]. The synthesis of fullerene-like nanoparticles of WS_2 and MoS_2 using solid precursors has been also demonstrated by the reaction of the corresponding metal oxide nanopowders, sulfur and a reducing agent ($NaBH_4$ or $LiAlH_4$), achieved either by heating up to ~900°C (near-equilibrium conditions) or by photothermal ablation driven by highly concentrated white light (non-equilibrium environment) [15].

Whereas IF-WS_2 nanoparticles can be made at an almost industrial scale, their formation mechanism is still not well understood. Layered chalcogenide nanoparticles are produced under kinetic control in a process far from equilibrium, photothermal ablation [15] being a

prototype example. This may also explain the lack of reproducibility for some reactions [16]. Recently we reported an *in situ* heating TEM study of the formation of IF-WS_2 and IF-MoS_2 from amorphous MoS_2 and WS_2 precursor nanoparticles obtained via metal organic chemical vapor deposition (MOCVD) [17], where defect annealing processes play a prominent role. In contrast, particles annealed *ex situ* showed a more facile particle growth and higher crystallinity due to enhanced surface diffusion in the surrounding Ar gas atmosphere [18].

In order to trap reaction intermediates of the nested fullerene formation, the reaction must be performed under kinetic control, and solid-state diffusion has to be excluded as the rate-determining step. This can be achieved either by reducing the diffusion pathway, i.e. through the nanostructure of the starting compounds [19] or by enhancing the atom mobility through surface diffusion, either through the gas [20] or the liquid [21] phase. In this contribution we describe the formation of giant WS_2 fullerenes with a controlled shell thickness of about 10 nm and void sizes of around 100-250 nm through the enhancement of surface diffusion with iodine. Lamellar reaction intermediates are occluded in the giant fullerene particles as demonstrated by TEM and scanning electron microscopy (SEM) after cross-cutting with a focused ion beam (FIB). These giant IF-fullerenes transform to "conventional" fullerenes upon extended annealing. The role of the reaction and annealing temperature on the composition and morphology of the final product were investigated, and the strength of the WS_2 shell was measured by intermittent contact-mode AFM.

3.2. Experimental Section

3.2.1. Synthesis

The reaction was carried out in a three zone horizontal furnace with tungsten (VI) carbonyl and iodine as molecular precursors. In a typical modified MOCVD run, five hundred milligrams (500 mg) of $W(CO)_6$ (Acros, 99%) was weighed inside the glove box and transferred outside the box in a corundum boat in an Ar filled chamber. Typically, 1000 mg of sublimated iodine was weighed in and mixed with $W(CO)_6$ immediately before the reaction. Prior to the synthesis, the setup was flushed with Ar for at least half an hour in the glass tube, and subsequently the corundum boat was placed inside a glass tube (inner diameter 15 mm), and this glass tube was placed in the upstream end of a reaction tube of an outer diameter of 35 mm inside a three zone horizontal furnace. Ar was flushed again through this setup for at least half an hour. The three zones of the furnace were then heated up to 600°C at the rate of 10˚C/min. Once the reaction temperature was reached, the boat was shifted to the center of the

furnace and the setup was flushed with H_2S for one hour. The temperature was again decreased to the room temperature with the rate of 10˚C/min under argon and the product was collected from the outer wall of the small glass tube by a spatula. The reaction was also carried out at 300, 400 and 500°C in an analogous fashion.

Thermal Annealing. The product obtained from the first step was then subjected to further annealing at 850°C for one hour under a constant argon flow of 100 sccm with a heating rate of 5˚C/min in a horizontal tube furnace. The collected intermediates were annealed in a corundum boat that was placed in the middle of a horizontal tube furnace. In order to analyze how the annealing temperature affects the composition and the morphology of final product, annealing was performed at 750, 800 and 900°C.

3.2.2. Material Characterization

X-ray Powder Diffraction. X-ray diffraction patterns (XRD) were recorded using a Siemens D5000 diffractometer equipped with a Braun M50 position sensitive detector in transmission mode using Ge (200) monochromatized CuK_α radiation. The samples were prepared between two layers of Scotch magic tape. Crystalline phases were identified according to the PDF–2 database using Bruker AXS EVA 10.0 software.

Electron Microscopy. Transmission electron microscopy and electron diffraction were performed on a Phillips EM-420 microscope equipped with a slow scan CCD detector (1k x 1k) and a LaB_6 electron gun operated with an acceleration voltage of 120 kV. Transmission electron microscopy (TEM) images were processed with the Gnu image manipulation program GIMP Version 2.6.8 or with Image J Version 1.43u. High resolution (HR) images were taken on a Philips FEI TECNAI F30 ST electron microscope (field-emission gun, 300 kV extraction voltages) equipped with an Oxford EDX (energy-dispersive X-ray) spectrometer with a Si/Li detector and an ultrathin window for elemental analysis and a STEM detector. Scanning transmission electron microscopy (STEM) images were obtained with a high angular annular dark field detector. All TEM samples were prepared by dispersing the sample in ethanol and drop casting onto 300 mesh carbon coated copper grids.

Focused Ion Beam. In order to cut the cross-sections of the product, a focused ion beam (FIB) dual beam instrument (Nova 600 Nanolab, FEI, Hillsboro, OR, USA) was used which combines scanning electron microscopy (SEM) and FIB within one instrument. SEM was performed before and after cutting cross sections. The powder was located on a double side conductive tape already stacked to a SEM sample holder. The chamber vacuum was around $5x10^{-5}$ mbar. To protect the surface of the sample, a platinum layer from the metal organic

precursor methylcyclopentadienyl(trimethyl)platinum(IV) was deposited with a gas assisted FIB deposition system. The thickness of the Pt deposit layer was around 1 µm. Afterwards, the cross section was made in 3 steps. First the regular cross section with 0.5 nA beam current followed by two cleaning cross sections with 0.3 and 0.1 nA currents. Finally, the images acquired after cross cutting were recorded using SEM.

Atomic Force Microscopy. The samples for atomic force microscopy (AFM) measurements were prepared by dispersing WS_2 powder in a water solution using an ultrasonic bath. A drop of this solution was applied to a clean silicon wafer. After the solvent had evaporated, the remaining structures were studied by AFM. All AFM images were recorded using a commercial AFM (Dimension 3100, Nanoscope IIIa controller, Veeco, California, USA) in intermittent contact-mode at room temperature and under ambient conditions. Additionally, this instrument was used to perform force-distance curves on the WS_2 structures. The instrument was equipped with a 3-axis piezoelectric tube scanner allowing a maximum lateral scan size of 100 µm and a maximum z-range of 6 µm. Silicon cantilevers (OMCLAC240TS Olympus) with aluminum backside coatings and a nominal resonance frequency and spring constant of 70 kHz and 2N/m, respectively, were used in order to image and measure force curves of the sample. The tip integrated at the end of the cantilever had a nominal radius < 10 nm. Cantilevers were plasma cleaned before performing the mechanical test.

3.3. Results and Discussion

3.3.1. Synthesis and formation mechanism of IF-WS_2 particles

IF-WS_2 was synthesized from a mixture of $W(CO)_6$, H_2S and I_2. In a first step the precursors $W(CO)_6$ and I_2 were reacted at 165 °C to a WI_x intermediate. Binary tungsten iodides are known to form either from the reaction of metallic tungsten with iodine in a temperature gradient [22] or by reaction of $W(CO)_6$ with liquid iodine. Binary tungsten iodide compounds having compositions W_6I_{12}, W_6I_{14}, W_6I_{15}, W_6I_{17}, WI_3, $WI_{3.3}$, and WI_4 from these reactions were identified by chemical analyses [22], whereas W_6I_{12} was reported to be isotypic with Mo_6I_{12} [22b]. The reaction of $W(CO)_6$ with I_2 was reported to lead to the formation of "WI_3" [22a], whose structure remained unidentified and is presumably W_4I_{13} that was identified in a later study [22g]. This WI_x intermediate was reacted with H_2S for one hour at 600°C. The reaction setup was cooled to room temperature, and the primary product was isolated and characterized by TEM and XRD. The overview TEM images (Figure 3-1a) show the primary product to consist exclusively of spherical particles aggregates with an average diameter of

200 nm. These nanoparticles are solid and partially intergrown (Figure 3-1b). Based on the X-ray diffraction pattern it contains 2H-WS_2 as the only crystalline phase (Figure 3-1c). Still, the primary sample releases iodine in visible amounts although neither iodine nor crystalline ternary W-S-I were identified by X-ray diffraction. In the second reaction step the primary product was annealed at 850˚C for 1 h under a constant flow of Ar. IF-WS_2 nanoparticles were obtained.

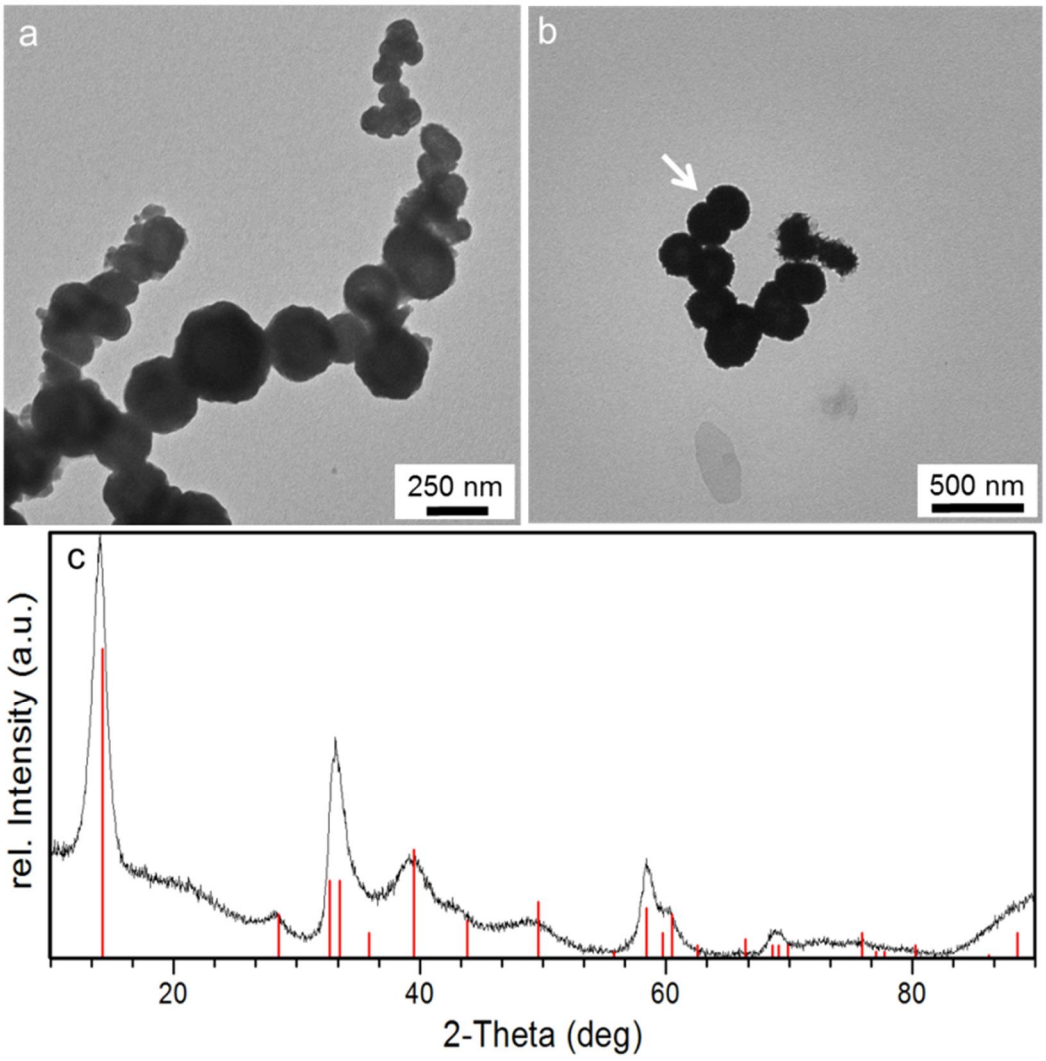

Figure 3-1. TEM images of the primary product obtained after the first step at 600°C. (a) Clusters of spherical particles, (b) Intergrown spherical particles (shown by an arrow) and (c) X-ray diffraction pattern of the primary product (line-pattern: 2H-WS_2, PDF-2 No. 08-0237).

X-ray powder diffraction. The X-ray powder diffraction (Figure 3-2) revealed the presence of 2H-WS_2 as the only crystalline product - all reflections could be assigned to tungstenite-2H (PDF-2 File Card No. 8-0237). A quantitative evaluation of these data using Rietveld refinements yielded refined lattice parameters of a = 3.143(1) Å and c = 12.706(6) Å and a

crystallite size approx. 9(1). The c-axis is significantly elongated in comparison to the reported value of the bulk material (c = 12.362 Å) which is implicated upon the formation of closed-cage facetted structures.Although the sample crystallinity judged from the powder X-ray profiles did not differ much for the primary product and the annealed product, electron microscopy acquisitions showed that the hollow closed-cage ordered layered structure was only present after the annealing step.

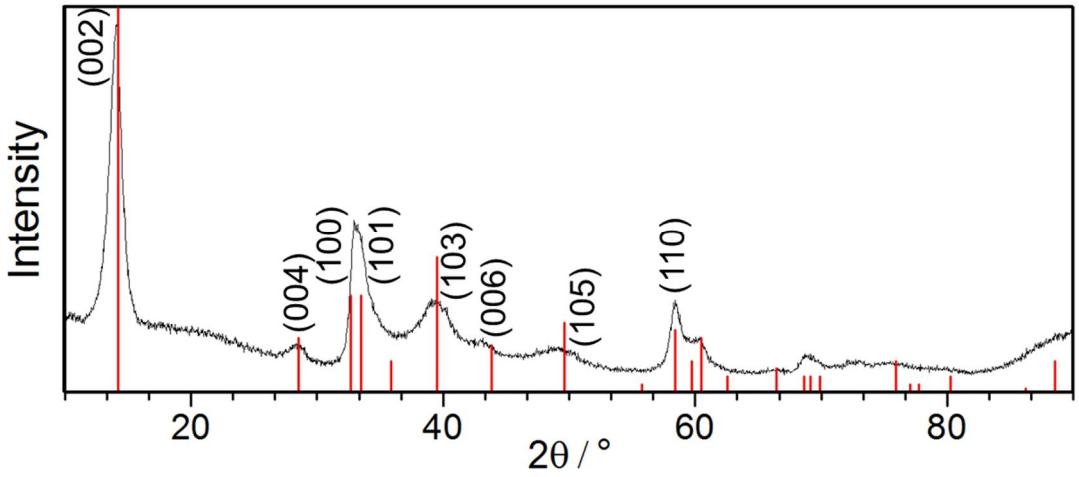

Figure 3-2. X-ray powder diffractogram of the product obtained after annealing at 850°C. Reflections are indexed according to 2H-WS_2 (PDF-2 No. 08-0237).

Electron microscopy. The product was further investigated using TEM, HRTEM, STEM, EDX line scanning, SEM and FIB. The TEM image in Figure 3-3a reveals that the product consists exclusively of spherical IF-WS_2 nanoparticles with diameters of 100-250 nm. HRTEM images show that the IF particles were not completely hollow, but contained encapsulated 2H-WS_2 lamellae (2H-WS_2@IF-WS_2), i.e. they contain a polycrystalline shell with encapsulated nanocrystalline lamellae without special orientation. The fullerene cages contain 14-16 layers in the external shell and about 8 layers in the lamellae. The STEM image in Figure 3-3c shows non-regularities in the thickness and in the length of the lamellae. EDX spectra revealed only the presence of W and S (Figure 3-3d). Although the 2H-WS_2@IF-WS_2 structures have thin walls and bear resemblance to MoS_2 giant bubbles [20], they are significantly smaller. The TEM images demonstrate that the dense spherical particles obtained in the first reaction step transform into the nested 2H-WS_2@IF-WS_2 structures shown in Figure 3-3.

In the first step, when the tungsten iodide intermediate reacts with H_2S, iodine might be partially trapped in between the lamellar crystallites of WS_2 in the form of non-crystalline WS_2I_x intermediates. A variety of ternary metal chalcogenides halide phases have been

described before [23,24]. In the second annealing step where the diffusion within the nested WS_2 fullerenes proceeds, the WS_2 lamellae interconnect through their outermost rims while the residual iodine inside the expanded IF-WS_2 particles is released. This leads eventually to the formation of 2H-WS_2@IF-WS_2 particles through iodine-assisted surface diffusion. When the nested fullerenes are formed, the inner lamellae are not integrated into the outer WS_2 shell, they are trapped in the form of short slabs. The 2H-WS_2@IF-WS_2 transform to "conventional" IF-WS_2 fullerenes after extended annealing.

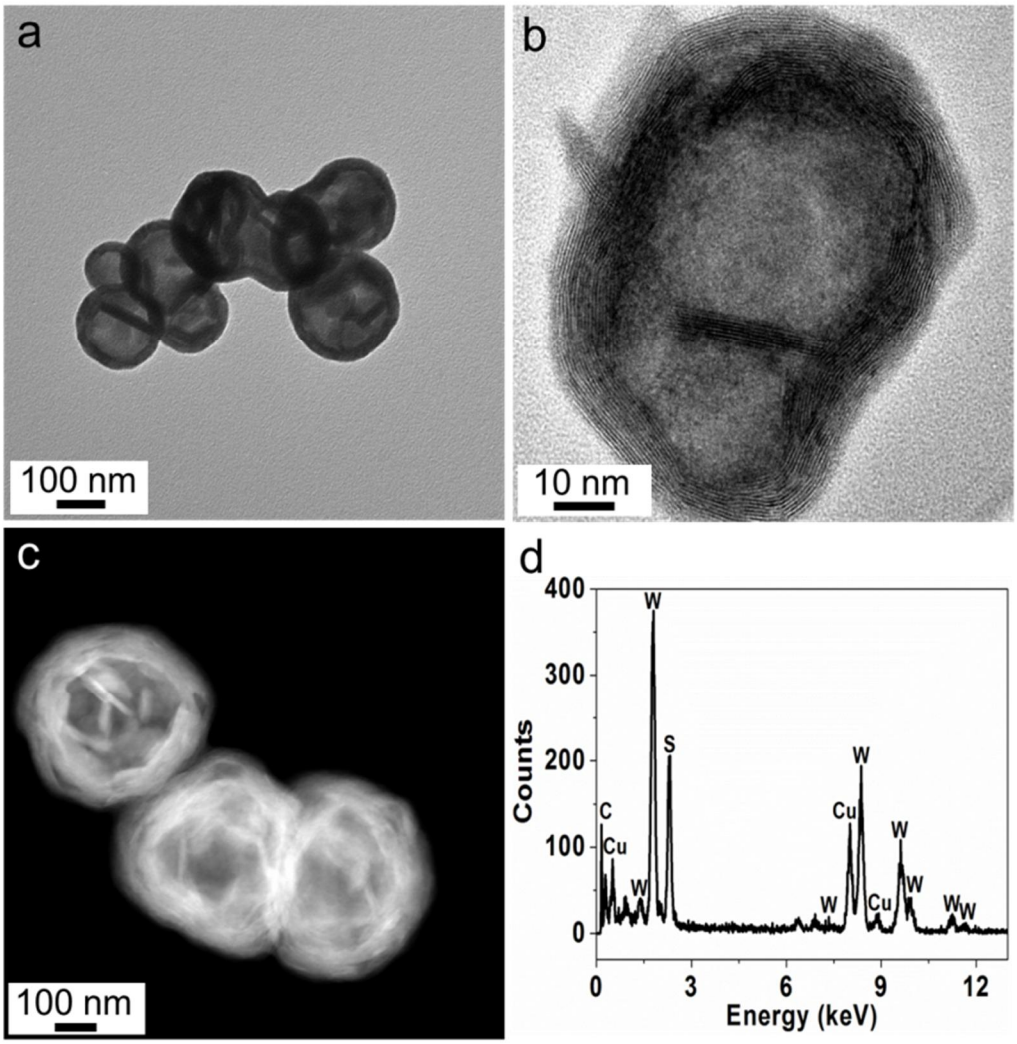

Figure 3-3. Physical characterization of the 2H-WS_2@IF-WS_2 nanoparticles. (a) TEM image of the product obtained after annealing. (b) HRTEM image of a particle showing the internal lamellae. (c) STEM image of several 2H-WS_2@IF-WS_2 particles. (d) EDX analysis of the 2H-WS_2@IF-WS_2 nanoparticles.

Finally, the structure of the 2H-WS_2@IF-WS_2 particles was investigated by STEM, EDX line scanning and a dual SEM/FIB technique. While the EDX elemental analysis indicated the overall the W and S content, an STEM/EDX line scanning analysis of individual

2H-WS_2@IF-WS_2 particles revealed their internal structure. The lighter contrast in Figure 3-4a corresponds to the WS_2 shell of the 2H-WS_2@IF-WS_2 particles and to the lamellae inside the fullerene cage. The EDX line-scan shows multiple maxima due to multiple sets of encapsulated lamellae (Figure 3-4b). A simplified sketch of the structure of the 2H-WS_2@IF-WS_2 particles is given in Figure 3-4c.

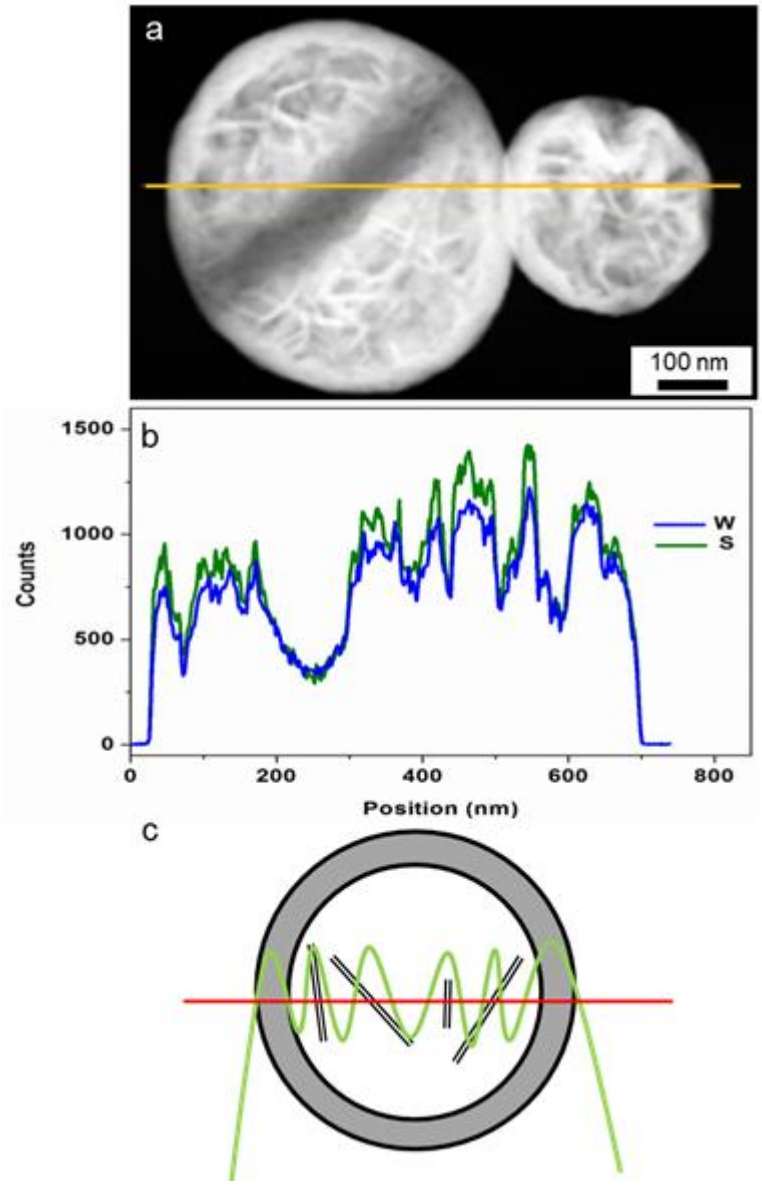

Figure 3-4. Structure of the 2H-WS_2@IF-WS_2 nanoparticles. (a) STEM image of two adjacent 2H-WS_2@IF-WS_2 nanoparticles. (b) Line scan for two particles. (c) Simplified sketch of a 2H-WS_2@IF-WS_2 particle and the path of the electron beam (red line) through the particle.

In order to obtain a direct view of the internal structure, a cross section was made with the FIB serial sectioning technique for scanning ion microscopy, which is very useful in observing the microstructures of materials. Figure 3-5a illustrates the SEM overview of the 2H-WS_2@IF-WS_2 nanoparticles. A platinum coating was used to stabilize a set of particles as shown in Figure 4b. The coated area was exposed to the ion beam and cut (the cutting line is shown by the dashed line in Figure 3-5b). Bombarding of the frozen particles located under the platinum layer with the high energy focused ion beam allowed us to observe the cross cut over a number of particles (Figure 3-5c). A lateral view over a giant particle reveals that the 2H-WS_2@IF-WS_2 particles are in fact not hollow but contain non-facetted structures inside the fullerene cage (Figure 3-5d).

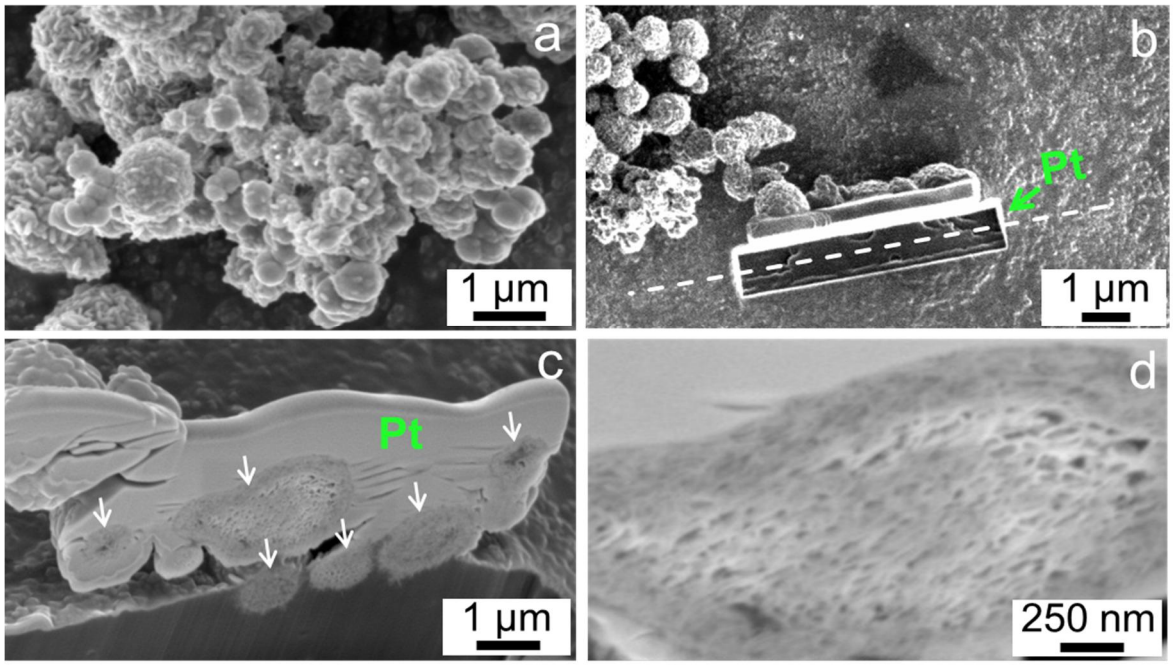

Figure 3-5. Characterization of the 2H-WS_2@IF-WS_2 particles nanoparticles using SEM/FIB. (a) Overview SEM image of the particles. (b) Selected row of the particles coated by platinum (top view). (c) The side view of the FIB-bombarded cross-section of the particles. (d) Magnified SEM image of the cross section showing the internal structure of 2H-WS_2@IF-WS_2 particles.

Influence of the reaction and annealing conditions. We also studied the role of the annealing temperature of the primary product on the structure and morphology of the 2H-WS_2@IF-WS_2 particles. The particles were annealed at 750˚C, 800˚C and 900˚C, and the products were investigated by TEM and XRD. The corresponding TEM images are provided on appendix, in the Supplementary Information (Figure S1-S3). Annealing at 750˚C leads to the formation of dense spherical particles (Figure S1, Supplementary Information). At 800°C

a fullerene-like shell starts to form the core still being amorphous. Further release of iodine causes the particles to expand because internal pressure is built up while a segregation of the outer shell and the internal compound becomes apparent (see Supplementary Information. Figure S2). The formation of the 2H-WS_2@IF-WS_2 particles occurs at 850˚C where the internal lamellae form an ordered crystalline structure. Further increase of the temperature to 900°C lead to a total collapse of the hierarchically structured nested fullerene and solid spherical particles were formed (Figure S3, Supplementary Information).

The first reaction step was also carried out at lower temperatures (300°C, 400°C and 500˚C) and the intermediate products were annealed at 850˚C under argon. The TEM image in Figure S4a (see Supplementary Information) shows that the product obtained at 300˚C leads to the formation of spherical WS_2 particles. When the pre-reaction was carried out at 400˚C hollow particles are about to form (Figure S4b). For pre-reactions at 500˚C the particles were not "fully" crystalline, but a layered structure starts to form on the shell of the particles (Figure S4c). In summary, smaller quantities of W-S-I intermediate were obtained with increasing reaction temperature, but more well-defined core-shell IF structures were obtained once the primary product was annealed.

Influence of the iodine content. The role of iodine on the mobility of the precursors was determined by varying the $W(CO)_6/I_2$ ratio. $W(CO)_6/I_2$ ratios of 1/0, 1, 1/2, 1/3 and 1/4 were tested in the MOCVD setup, and the primary products were annealed at 850˚C. In the absence of I_2, *i.e.* using only $W(CO)_6$ and H_2S as precursors, spherical particles (with small scrolls on the surface) were obtained and no transformation into nested fullerenes was observed (Figure 3-6a). For $W(CO)_6/I_2$ = 1 agglomerated spherical particles rather than nested fullerenes or "giant bubbles" [20] were formed (Figure 3-6b). For $I_2/W(CO)_6$ ratios > 3 no enhancement of the crystallinity was observed.

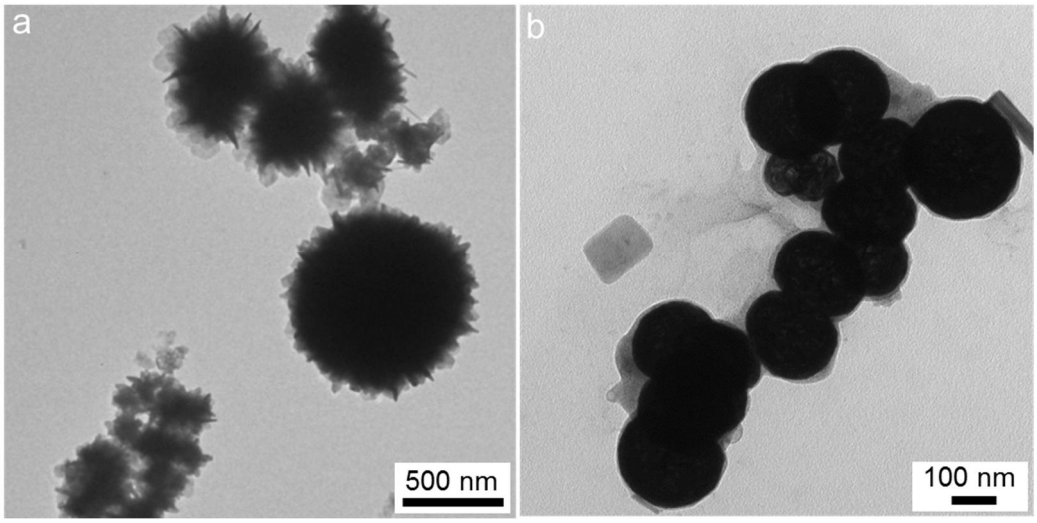

Figure 3-6. TEM image of the annealed product obtained (a) without iodine and (b) for a $W(CO)_6/I_2$ ratio of 1:1.

As illustrated in Scheme 3-1 the thermal decomposition of the amorphous precursor and the concomitant loss of iodine to the gas phase are accompanied by the buildup of a gas pressure inside the fullerenes. Assuming that the reaction to WS_2 from WI_x and H_2S step occurs without a loss of iodine and leads to a homogeneous distribution of the iodine within the WS_2 particles we estimate the amount of iodine inside a WS_2 sphere with a diameter of about 200 nm (volume ca. 4 x 10^{-15} mL) to be ≈ 10^{-19} mmol. For the corresponding molybdenum system the vapor above a mixture of MoS_2 and I_2 in the range from 400 to 800°C consists almost exclusively of I_2 [25], and similar situation is likely for the tungsten analogue. In this scenario, the pressure at 850°C is ≈ 2.3 bar. We assume that iodine assists the formation of IF-WS_2 by forming a highly mobile surface film [26] of volatile iodine or WI_x intermediates. As a result, the precursor particles transform to large hollow particles with giant fullerene-type structures during the annealing process. Parts of the vapor phase (iodine or WI_x) are trapped within the expanding IF-fullerene particles [27]. Upon annealing the thermal decomposition of the precursor particles proceeds while, at the same time, the vapor pressure within the fullerene increases. This leads to the observed “size-up” effect through the thermal expansion of the encapsulated gas phase. The forming fullerene particle is stable as long as the pressure inside the fullerene remains below a “burst” threshold value.

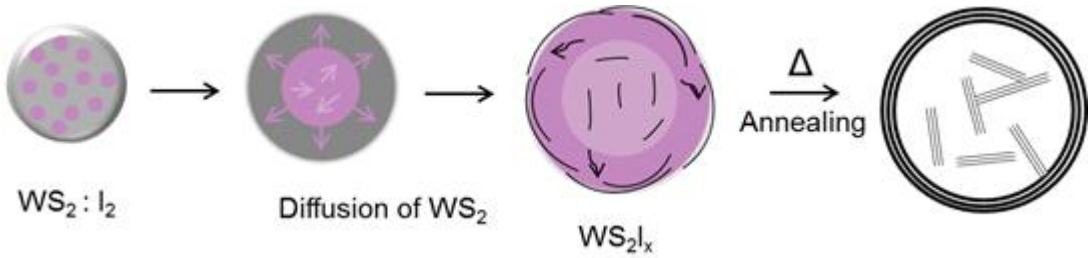

Scheme 3-1. Formation of 2H-WS_2@IF-WS_2 particles in the presence of iodine.

3.3.2. Mechanical stability of the 2H-WS_2@IF-WS_2 particles

Inorganic IF-WS_2 and IF-MoS_2 nanoparticles are known to be good friction modifiers and anti-wear additives. Their tribological performance is related to their structure, size, and shape. In order to obtain information concerning mechanical properties of the 2H-WS_2@IF-WS_2 particles and the relation to their internal structure AFM images of the 2H-WS_2@IF-WS_2 particles were recorded in the intermittent contact-mode and the height and phase images are shown in Figure S5, Supplementary Information. Figure S5a depicts a 2H-WS_2@IF-WS_2 particle height profile while Figure S5b shows its phase profile. The force required to rupture such a particle was determined from AFM force-distance curves. Intermittent contact-mode imaging was used to locate the sphere on the substrate and to position the AFM tip on top of the sphere. Prior to recording force curves on the sphere, the cantilever was calibrated using the thermal tune method [28]. Additionally, reference force curves were recorded on a hard substrate, in this case, the silicon substrate next to the sphere. Figure 3-7a shows such force-distance curves. A negative value of the tip-sample distance represents the deformation of the shell. The load on the sphere was gradually increased up to a loading trigger of 30 nN (1st curve in black). At this triggering value, the yield of the shell was observed at 25 nN during the 2nd curve (in red), producing a deviation from a linear elastic behavior. The second curve shows that it is necessary to move the tip further within the shell in order to obtain the same 30 nN as in the first curve. This means that the surface of the shell has lost its original mechanical stiffness and has been ruptured. At the end of the second curve a second increase in slope was observed, indicating that the other side of the shell initially supported on the substrate is touched. The 3rd curve (in blue) shows a slightly higher slope than the second curve, which indicates pressing against the supported side of the shell [27]. During the third curve, at around 27 nN, the yield of the supported shell occurred. This yield value agrees well with the values already reported for MoS_2 "bubbles" (18 nN) [20]. Right after the yield of the supported side, a drastic increase in the force-distance slope was acquired (4th curve in green), pointing to have punctured the pathway through the silicon

substrate. To support this idea it is noticeable that the distance from the jump-in of the force curve to the high-slope section of the 3rd curve is ~10 nm which corresponds to about 16 layers of WS_2. This acquisition is consistent with the value obtained from shell thickness by HRTEM (as demonstrated in Figure 3-7b).

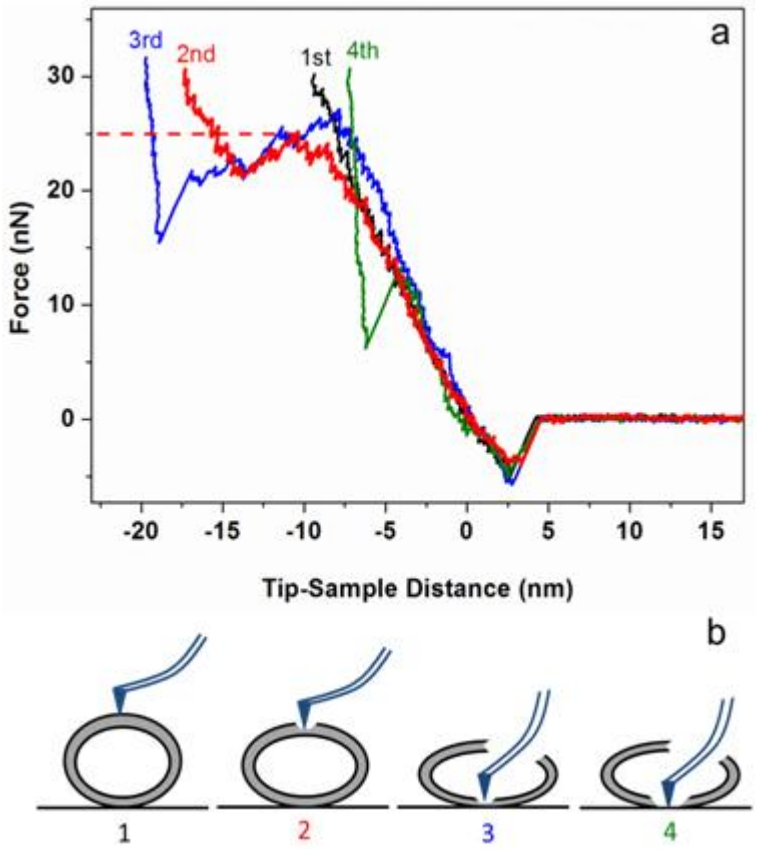

Figure 3-7. (a) Force curves obtained from intermittent contact AFM on a 2H-WS_2@IF-WS_2 particle. The rupture on the surface happens at 25 nN as can be seen from the 2nd curve (red). (b) Scheme illustrating the stepwise rupture of the 2H-WS_2@IF-WS_2 particles.

3.4. Conclusions

We have unravelled the formation mechanism of nested IF-WS_2 by annealing amorphous W-S-I nanoparticle precursors captured from an MOCVD reaction. The MOCVD approach allows not only the trapping of reaction intermediates by thermal quenching, but also a facile control of the reaction process and a monitoring of the particle growth by the choice of experimental parameters such as composition and temperature. Our strategy was to use amorphous W-S-I precursor nanoparticles to eliminate solid-state diffusion as a rate determining step in the formation of nested fullerenes. Thermal decomposition of the precursors at 400°C in the second reaction step leads to the formation of expanded fullerene cages with diameters > 200 nm that were enclosed by about 15 WS_2 layers. This "size-up" step appears to be due to a "bubble effect" from the gas phase generated during the thermal decomposition of the precursor compounds. The resulting inside-to-outside diffusion flow of reactive gas phase species leads to the formation of nested IF-particles with a number of lamellae trapped inside the fullerene cage. The role of the reaction and annealing temperature on the composition and morphology of the final product were also investigated and the strength of the WS_2 shell was measured by intermittent contact-mode AFM and the force needed to pop up the shells was determined. The higher mechanical stability of the 2H-WS_2@IF-WS_2 particles compared to IF-MoS_2 giant bubbles can be related to a cross-beam effect of the lamellae trapped inside the fullerene cage. The presence of lamellar structures inside the hollow cage may lead to enhanced tribological activities, because small particle sizes and crystal defects contribute to a fast exfoliation of the IF-nanoparticles: the amorphous character of the particles and the presence of defects, facilitate an exfoliation of layers under external pressure and therefore ameliorate the tribological performance of the material [29].

3.5. References

[1] G. A. Ozin, A. C. Arsenault, L. Cademartiri, Nanochemistry, A Chemical Approach to Nanomaterials, 2nd Ed., RSC Publishing, Cambridge 2009.

[2] (a) C. N. R. Rao, M. Nath, *Dalt. Trans.* **2003**, 1; R. Tenne, *Nat. Nanotechnol.* **2006**, *1*, 103. (b) R. Tenne, M. Remsar, A. Enyashin, G. Seifert, *Topics Appl. Physics* **2008**, *111*, 631. (c) R. Tenne, G. Seifert, *Annu. Rev. Mater. Res.* **2009**, *39*, 2.1. (d) M. N. Tahir, A. Yella, J. K. Sahoo, H. A. Therese, N. Zink, W. Tremel, *Phys. Status Solidi B* **2010**, *247*, 2338.

[3] (a) R. Tenne, L. Margulis, M. Genut, G. Hodes, *Nature* **1992**, *360*, 444. (b) L. Margulis, G. Salitra, R. Tenne, M. Talianker, *Nature*, **1993**, *365*, 113. (c) Y. Feldman, E. Wasserman, D. J. Srolovitz, R. Tenne, *Science* **1995**, *267*, 222.

[4] (a) J. Chen, Z.-L. Tao, S.-L. Li, *Angew. Chem.* **2003**, *115*, 2197; Angew**.** Chem. Int**.** Ed. **2003**, *42*, 2147. (b) X. L. Li, Y. D. Li, *Chem. Eur. J.* **2003**, *9*, 2726. (c) H. A. Therese, F. Rocker, A. Reiber, J. Li, M. Stepputat, G. Glasser, U. Kolb, W. Tremel, *Angew. Chem. Int. Ed.* **2005**, *44*, 262. (d) C. Schuffenhauer, B. A. Parkinson, N. Y. Jin-Phillipp, J. Joly-Pottuz, J. M. Martin, R. Popovitz-Biro, R. Tenne, *Small* **2005**, *1*, 1100. (e) M. Remskar, M. Virsek, A. Jesih, *Nano Lett.* **2008**, *8*, 76. (f) A. Yella, H. A. Therese, M. Panthöfer, W. Tremel, *Chem. Mater.* **2008**, *20*, 3587. (g) A. Yella, E. Mugnaioli, H. A. Therese, M. Panthöfer, U. Kolb, W. Tremel, *Chem. Mater.* **2009**, *21*, 2474.

[5] (a) W. Tremel, R. Seshadri, E. W. Finckh, *Chem. unserer Zeit* **2001**, 35, 42. (b) W. Tremel, E. W. Finckh, E. W. *Chem. unserer Zeit* **2004,** 38, 326.

[6] F. Hulliger, Struct. Bonding (Berlin) 1968, 4, 83. (b) Structural Chemistry of Layer-type Phases; F. Levy, Ed., D. Reidel: Baton, 1976; Vol. 5.

[7] F. Jellinek, G. Brauer, H. Müller, H. *Nature* **1960**, *185*, 376.

[8] (a) M. Chhowalla, G. A. J. Amaratunga, *Nature* **2000**, *407* 164. (b) L. Joly-Pottuz, F. Dassenoy, M. Belin, B. Vacher, J. M. Martin, N. Fleischer, *Tribol. Lett.* **2005**, *18*, 477. (c) L. Rapoport, N. Fleischer, R. Tenne, *J. Mater. Chem.* **2005**, *15* 1782.

[9] M. Redlich, A. Katz, L. Rapoport, H. D. Wagner, Y. Feldman, R. Tenne, *Dental Materials* **2008,** 24, 1640.

[10] (a) Y. Q. Zhu, T. Sekine, K. S. Brigatti, S. Firth, R. Tenne, R. Rosentsveig, H. W. Kroto, D. R. M. Walton, *J. Am. Chem. Soc.* **2003**, *125*, 1329. (b) Y. Q. Zhu, T. Sekine,

Y. H. Li, M. W. Fay, Y. M. Zhao, C. H. P. Poa, W. X. Wang, M. J. Roe, P. D. Brown, N. Fleischer, R. Tenne, *J. Am. Chem. Soc.* **2005**, *127*, 16263.

[11] (a) J. Chen, N. Kuriyama, H. Yuan, H. Takeshita, T. Sakai, *J. Am. Chem. Soc.* **2001**, *123*, 11813. (b) R. Dominko, D. Arcon, A. Mrzel, A. Zorko, P. Cevc, P. Venturini, M. Gabersek, M. Ramskar, D. Mihailovic, *Adv. Mater.* **2002**, *14*, 1531. (c) K. Tibbetts, C. R. Miranda, Y. S. Meng, G. Ceder, *Chem. Mater.* **2007**, *19*, 5302.

[12] S. Helveg, J. V. Lauritsen, I. Lægsgaard, J. K. Stensgaard, H. Nørskov, B. S. Clausen, H. Topsøe, F. Besenbacher, *Phys. Rev. Lett.* **2000**, *84*, 951. (b) J. V. Lauritsen, J. Kibsgaard, S. Helveg, H. Topsøe, B. S. Clausen, E. Lægsgaard, F. Besenbacher, *Nature Nanotechnol.* **2007**, *2*, 53.

[13] Y. Feldman, G. L. Frey, M. Homyonfer, V. Lyakhovitskaya, L. Margulis, H. Cohen, G. Hodes, J. L. Hutchison, R. Tenne, *J. Am. Chem. Soc.* **1996**, *118*, 5362.

[14] Y. Feldman, A. Zak, R. Popovitz-Biro, R. Tenne, *Solid State Sci.* **2000**, *6*, 663.

[15] I. Wiesel, H. Arbel, A. Albu-Yaron, R. Popovitz-Biro, J. M. Gordon, D. Feuermann, R. Tenne, *Nano Res.*, **2009**, *2*, 416.

[16] M. Nath, A. Govindaraj, C. N. R. Rao, *Adv. Mater.* **2001,** 13, 283.

[17] A. Yella, H. A. Therese, N. Zink, M. Panthöfer, W. Tremel, *Chem. Mater.* **2008**, *20*, 3587.

[18] (a) J. Etzkorn, H. A. Therese, F. Rocker, N. Zink, U. Kolb, W. Tremel, *Adv. Mater.* **2005**, *17*, 2372. (b) N. Zink, J. Pansiot, J. Kieffer, H. A. Therese, M. Panthöfer, F. Rocker, U. Kolb, W. Tremel, *Chem. Mater.* **2007**, *19*, 6391. (c) A. Yella, E. Mugniaoli, H. A. Therese, M. Panthöfer, W. Tremel, *Chem. Mater*, **2009**, *21*, 2474.

[19] A. Yella, E. Mugnaioli, U. Kolb, M. Panthöfer, W. Tremel, *Angew. Chem. Int. Ed.* **2010**, *49*, 3301.

[20] (a) A. Yella, E. Mugnaioli, M. Panthöfer, U. Kolb, W. Tremel, *Angew. Chem. Int. Ed.* **2009**, *48*, 6426. (b) G. Radovsky, R. Popovitz-Biro, M. Staiger, K. Gartsman, C. Thomsen, T. Lorenz, G. Seifert, R. Tenne, *Angew. Chem. Int. Ed.* **2011**, *50*, 12316.

[21] A. Yella, M. Kappl, M. Panthöfer, W. Tremel, *Angew. Chem. Int. Ed.* **2010**, *49*, 2575.

[22] (a) C. Djordjevic, R. S. Nyholm, C. S. Pande, M. H. B. Stiddard, *J. Chem. Soc.* **1966**, 16. (b) H. Schäfer, H.-G. Schnering, J. Tillack, F. Kuhnen, F. Wöhrle, H. Baumann, *Z. Anorg. Allg. Chem.* **1967**, *353*, 281. (c) H. G. Schulz, R. Siepmann, H. Schäfer. *J . Less-Common Met.* **1970**, *22*, 136. (d) R. D. Hogue, R. E. McCarley. *Inorg. Chem.* **1970**, *6*, 1354. (e) H. Schäfer, H.-G. Z. Schulz, *Z. Anorg. Allg. Chem.* **1984**, *516*, 196. (f) Y. Virmani, D. S. Bames, H. A. Skinner, *J. Chem.* Soc. *Dalton Trans.* **1974**, 399.

(g) J. D. Franolic, J. R. Long, R. H. Holm, *J. Am. Chem. Soc.* **1995**, *117*, 8139.

[23] W. Tremel, *Inorg. Chem*. **1992**, *31*, 755.

[24] J. Rouxel, *Acc. Chem. Res*. **1992**, *25*, 328.

[25] U. Hotje, M. Binnewies, *Z. Anorg. Allg. Chem.* **2005**, *631*, 2467.

[26] (a) D. Juza, D. Giegling, H. Schäfer, *Z. Anorg. Allg. Chem.* **1969**, *366*, 121. (b) H. Schäfer, *Chem. Int. Ed. Engl.* **1971**, *10*, 43.

[27] (a) N. Bertram, J. Cordes, Y. D. Kim, G. Ganteför, S. Gemming, G. Seifert, *Chem. Phys. Lett.* **2006**, *418*, 36. (b) S. Gemming, J. Tamuliene, G. Seifert, N. Bertram, Y. D. Kim, G. Ganteför, *Appl. Phys. A* **2006**, *82*, 161.

[28] J. Domke, M. Radmacher, *Langmuir* **1998**, *14*, 3320.

[29] J. Tannous, F. Dassenoy, A. Bruhács, W. Tremel, *Tribol. Lett.* **2010**, *37*, 83.

Defects as a Tool to Solubilize and Functionalize WS_2 Nanotubes

Associated publication: *Dalt. Trans.*, **2012**, *submitted*

4.1. Introduction

Nanotubes (NTs) and nested inorganic fullerenes (IFs) are allotropes of layered transition-metal chalcogenides at the nanoscale [1-3], which have demonstrated great potential for various applications such as solid lubricants [4-6], as cathode materials in rechargeable batteries [7], as shock-resistant materials [8], or in sulfur removal catalysis [9]. Many properties of these nanomaterials such as tribological behavior, mechanical strength, electrical resistivity or optical and magnetic properties are related to their crystal structure which is characterized by weak van der Waals forces between the individual MQ_2 layers containing metal atoms sandwiched between two inert chalcogen sheets. Still, the elastic strain originating from surface curvature and intrinsic defects leads to reactive sites at the edges of the closed-cage structures [10].

One-dimensional (1D) nanostructures such as nanotubes or nanowires are of particular interest because they allow studying physical and chemical properties such as mechanical strength, electrical resistivity, or optical and magnetic properties confined in one dimension. In this regard, tungsten sulfide (WS_2) has found useful applications in photovoltaics [11], medical coatings [12] and impact-absorbing materials [13]. In order to exploit these applications the first challenge is to gain control of the interfaces of layered chalcogenide nanoparticles and substrates to adjust the wetting properties of both materials. Although different approaches have been put forward in the past years to tailor the surfaces of layered metal chalcogenides nanoparticles [14-18] an engineering of their surfaces has been mostly neglected. It has been demonstrated recently that point defects on the surfaces of chalcogenide nanoparticles can be marked as reactive sites with chalcophilic agents such as gold nanoparticles [19,20]. The defect sites could be passivated by silane coating. These findings suggest that the functionalization of layered metal chalcogenide surfaces is promoted by surface defects. The surface coverage appears to be proportional to the defect density. Therefore there is a need to develop synthetic methods to control the defect density while preserving the bulk characteristics of layered metal chalcogenides A variety of methods has been reported for the synthesis of WS_2 nanotubes, including the sulfidization of metal oxides [21-26], deposition in porous alumina [27], electron-beam irradiation activation [28], arc discharge [29,30] and sonoelectrochemical bath reaction [31] or electrochemical deposition from an ethylene glycol solution [32]. Still, the reductive sulfidization of WO_x nanoparticles has proven the most efficient method for the synthesis of WS_2 nanotubes (NT-WS_2) and fullerene nanoparticles (e.g. IF-WS_2) [21-26].

Different from most inorganic nanoparticles, layered chalcogenide nanotubes and inorganic fullerenes have long resisted functionalization using standard surface chemistry. The inert chalcogenide layers sandwiching the metal atoms sterically shield them from a nucleophilic attack by organic ligands and makes chalcogenide nanoparticles inert and notoriously difficult to functionalize. Therefore covalent surface functionalization of layered chalcogenides needs metals with a high sulfur affinity as a "glue" for anchoring organic ligands to the sulfur surface [14-18].

In this contribution we report the synthesis of highly dispersible and surface active WS_2 nanotubes, which were formed by reductive sulfidization of $W_{18}O_{49}$ nanoparticles obtained through the controlled hydrolysis of WCl_6 with primary alcohols under solvothermal conditions. These $W_{18}O_{49}$ nanoparticles were used as precursors for the synthesis of the WS_2 nanotubes. Defect-rich nanotubes were dispersible easily in organic solvent and could be functionalized with different types of inorganic nanoparticles.

4.2. Experimental Section

4.2.1. Synthesis

Solvothermal Synthesis of $W_{18}O_{49}$ Nanowires. The starting solution for all the experiments was prepared by dissolving 506.25 mg of tungsten hexachloride (98%, WCl_6, ABCR) in 25 mL of ethanol (P.A. VWR) by sonication ([WCl_6] = 0.05 M). Typically, the final solution was prepared by injecting 3.2 mL of the starting solution in a 50 mL Teflon-lined vessel containing 31.8 mL of the respective alcohol ([WCl_6] = 0.0045 M). The Teflon-lined vessel was sealed in a stainless steel autoclave. Unless mentioned otherwise, the solvothermal reaction was carried out for 10 h at 200°C in an electric oven. After the reaction, dark blue fluffy particles were collected by centrifugation, rinsed with ethanol three times and dried at 60°C. To study the influence of the concentration of the tungsten source on the morphology of the tungsten oxide nanowires, the final solution was also prepared in different concentrations (0.007 M and 0.0055 M) by injecting 5 mL and 3.9 mL of the starting solution into the Teflon-lined vessel containing 30 mL and 31.1 mL ethanol, respectively. To study the role of the of alcohol on the growth and morphology of the tungsten oxide nanowires the reaction was carried out with methanol (≥99.8%, Sigma-Aldrich), 1-propanol (≥99.5%, Sigma-Aldrich) and cyclohexanol (99%, ABCR) in an analogous manner, and the final

solution was in turn prepared by injection of 3.2 mL of the starting solution into the Teflon-lined vessel containing 31.8 mL of the alcohols.

Synthesis of $W_{18}O_{49}$ Nanorods by Hot Injection [33]. In a typical synthesis tungsten ethoxide (0.5 mL) was injected into a preheated mixture containing of trioctyl amine (17.5 mL) and oleic acid (12.5 mL) at 320 °C. The temperature was held for 5 minutes, followed by cooling to room temperature. The $W_{18}O_{49}$ nanorods were precipitated by addition 15 mL of ethanol. The product was collected by centrifugation and washed with ethanol and aceton.

Synthesis of WS_2 Nanotubes by Reductive Sulfidization of $W_{18}O_{49}$ Nanorods/wires. The as-synthesized $W_{18}O_{49}$ nanowires/nanorods were placed in a corundum boat inside a quartz tube which was flushed with argon for half an hour prior to the reaction to remove oxygen. The corundum boat was kept in the middle of the furnace and heated to 850°C at the rate of 5°C/min under constant flow of argon. Just before reaching to 850°C, the argon was switched to H_2S gas with a flow rate of 40 sccm and kept at this temperature for half an hour. The H_2S flow was carefully controlled using a flow meter. After half an hour, the furnace was cooled to ambient temperature at the rate of 5°C/min under constant flow of argon. The resulting black powder was collected and used for the further characterization.

Synthesis and Functionalization of WS_2 Nanotubes with Metal (Au), Metal Oxide (MnO) and Janus Type metal@metal oxide ($Pt@Fe_3O_4$) Nanoparticles. The Au, MnO and $Pt@Fe_3O_4$ nanoparticles were synthesized as reported earlier [34,35]. In a typical experiment 3 mg of the WS_2 nanotubes were dispersed in 5 mL of chloroform/ethanol (1:1) by sonicating the sample for 5-7 min. The solution was degassed under argon for 10-15 min. In another centrifuge vial, 8 mg of the nanoparticles were dissolved in 5 mL of chloroform (Au, MnO, $Pt@Fe_3O_4$). Subsequently, the solution was added dropwise to the degassed mixture of WS_2 nanotubes over a period of 5-7 min. The reaction mixture was degassed again under argon for 5 min and put in a shaker for 2 h at room temperature (RT). After the reaction was complete unbound nanoparticles were removed by centrifuging the sample thrice at 4000 rpm for 10 min. Finally, the functionalized WS_2 nanotubes were characterized by TEM/HRTEM combined with EDX. Samples for TEM were prepared by putting 1-2 drops of dispersed sample on a copper TEM grid followed by drying.

4.2.2. Material Characterization

X-ray Powder Diffraction. X-ray diffraction patterns (XRD) were recorded on a Siemens D5000 diffractometer equipped with a Braun M50 position sensitive detector in transmission

mode using Ge (200) monochromatized CuKα radiation. Samples were prepared between two layers of Scotch Magic Tape. Crystalline phases were identified according to the PDF–2 database using the Bruker AXS EVA 10.0 software.

Electron Microscopy. Transmission electron microscopy (TEM) and electron diffraction (ED) were performed on a Phillips EM-420 equipped with a slow scan CCD detector (1k x 1k) and a LaB6 electron gun operated with an acceleration voltage of 120 kV. TEM images were processed with the Gnu Image Manipulation Program GIMP Version 2.6.8 or with Image J Version 1.43u. High resolution (HR) images were taken with a Philips FEI TECNAI F30 ST electron microscope (field-emission gun, 300 kV extraction voltages) equipped with an Oxford EDX (energy-dispersive X-ray) spectrometer with a Si/Li detector and an ultrathin window for elemental analysis and a STEM detector. TEM samples were prepared by dispersing the sample in ethanol and drop casting on 300 mesh carbon coated copper grids.

4.3. Results and Discussion

The $W_{18}O_{49}$ nanowires [36] were prepared by solvothermal treatment and sulfidized subsequently to obtain WS_2 nanotubes. Scheme 4-1 illustrates the synthetic route for the preparation of the $W_{18}O_{49}$ nanowires and their conversion to WS_2 nanotubes. In the first step, a tungsten chloride solution in ethanol was diluted with an alcohol (ROH, R = Me, Et, Pr and c-C_6H_{11}) and transferred into a Teflon-lined vessel which was sealed in a stainless autoclave and subjected to the solvothermal treatment. After cooling to room temperature dark blue nanowires $W_{18}O_{49}$ were obtained. The alcohols serve in this reaction as solvent, reducing and hydrolysis agent. In the second reaction step the $W_{18}O_{49}$ nanowires were sulfidize to WS_2 nanotubes.

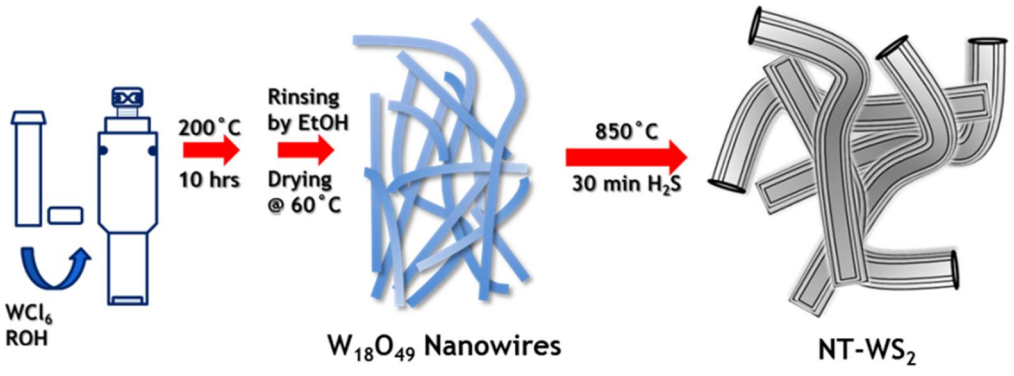

Scheme 4-1. Formation of $W_{18}O_{49}$ nanowires and their transformation to WS_2 nanotubes.

Details concerning the morphology and the crystallinity of the $W_{18}O_{49}$ nanoparticles as a function of the preparation conditions are given here. All $W_{18}O_{49}$ precursor particles were sulfidized under identical conditions by reaction with H_2S for 30 min at 850°C. Therefore differences in the crystallinity and the defect density can be attributed to the particle uniformity, size, crystallinity and aspect ratio of the $W_{18}O_{49}$ precursor particles. The resulting WS_2 nanotubes were characterized by TEM, HRTEM and XRD. The X-ray diffractogram in Figure 4-2b indicates the presence of single-phase 2H-WS_2 (PDF-2 file card No. 08-0237).

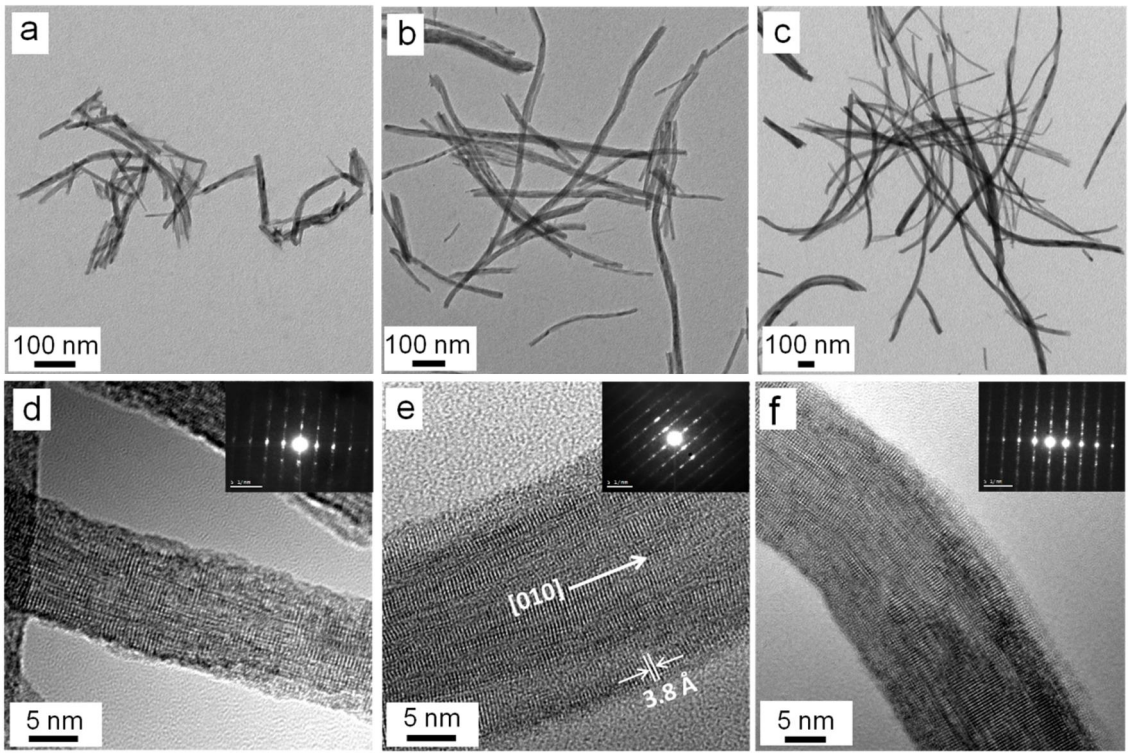

Figure 4-1. TEM/HRTEM images of $W_{18}O_{49}$ nanowires obtained from 0.0045 M (a,d) methanolic, (b,e) ethanolic and (c,f) propanolic solution.

To study the effect of the reaction conditions on the uniformity, crystallinity and morphology of the $W_{18}O_{49}$ nanoparticles, the reaction conditions (temperature, reaction time and precursor concentration) were varied systematically. Figure 4-1 shows $W_{18}O_{49}$ nanoparticles obtained by hydrolysis in different alcohols. The diameter and the length of the nanoparticles could be tuned from 10-40 nm over 1 micron to several micrometers by varying the hydrolysis reagent (methanol, ethanol, propanol). Nanowires obtained from propanol are quite uniform in diameter compared to those obtained from methanol or ethanol. Variation of the WCl_6 concentration did not lead to significant changes. Although the morphology, size and monodispersity of the nanoparticles differ to some extent, their crystallinity is very similar as

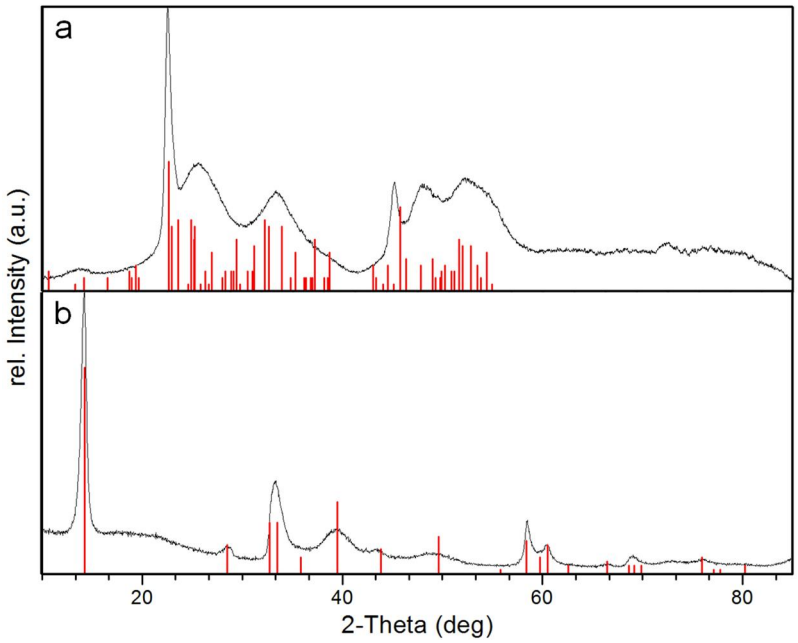

Figure 4-2. (a) X-ray powder diffraction patterns of (a) as-synthesized tungsten oxide nanowires and (b) corresponding tungsten disulfide nanotubes.

judged by X-ray powder diffraction (Figure 4-2a). The synthesis was carried out at different reaction conditions. The corresponding TEM images of the $W_{18}O_{49}$ nanoparticles are shown in Figure 4-3. Well-defined and monodisperse $W_{18}O_{49}$ nanoparticles could be obtained from reactions at 200°C, reaction times of 10 h and precursor concentrations of 0.0045 M. The results are compiled in Table 4-1.

Table 4-1. Comparison of $W_{18}O_{49}$ nanowires prepared under different reaction conditions.

Solvent	Concentration (M)	Temperature (°C)	Duration (h)	Size (nm)
MeOH	0.0045	200	10	10 × 200
EtOH	0.0045	200	10	20 × 600
PrOH	0.0045	200	10	20 × 2 µm
c-$C_6H_{11}OH$	0.0045	200	10	25 × 500
EtOH	0.0055	200	10	40 × 500
EtOH	0.0071	200	10	25 × 300
EtOH	0.0071	220	5	20 × 200

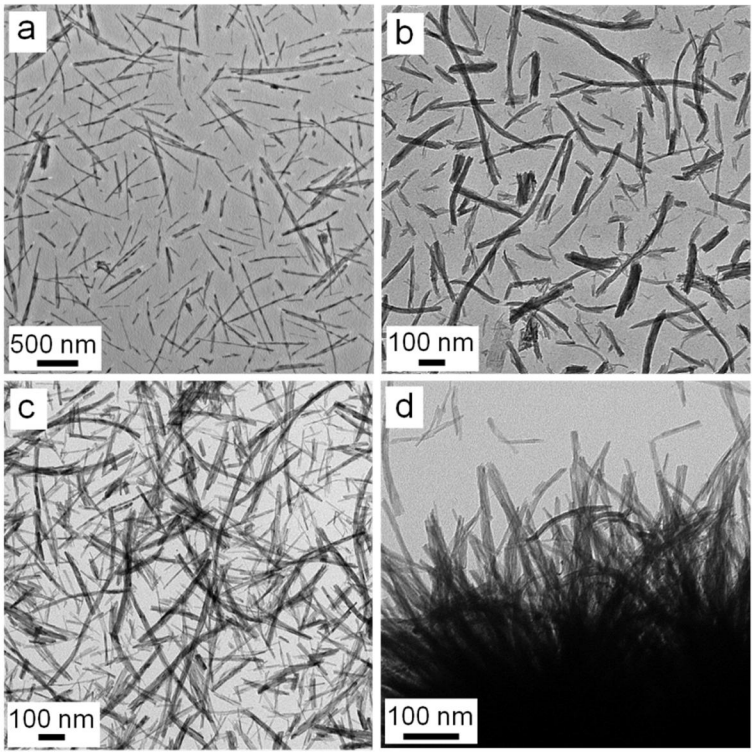

Figure 4-3. TEM overview of the tungsten oxide product obtained in (a) cyclohexanol, (b) EtOH (0.0055 M), (c) EtOH at 0.0071 M and (d) EtOH (0.0071 M) when treated at 220°C for 5 hours.

Figure 4-4 shows TEM overview and HRTEM images of the WS_2 nanotubes resulting from the sulfidization of the $W_{18}O_{49}$ nanoparticles obtained by hydrolysis in different alcohols. The uniformity and yield of WS_2 nanotubes obtained from $W_{18}O_{49}$ nanoparticles made in propanol (Figure 4-4c, f) was much better than that of nanotubes made from $W_{18}O_{49}$ nanoparticles obtained from ethanol (Figure 4-4b, e) and methanol (Figure 4-4a, b). We attribute this to the size and crystallinity of the corresponding $W_{18}O_{49}$ nanoparticles. Sulfidization of $W_{18}O_{49}$ nanoparticles obtained from methanol lead to $\geq$ 80% by-products of nanosheets and nanoscrolls, whereas long (up to 4 μm), uniform and flexible WS_2 nanotubes were obtained from $W_{18}O_{49}$ nanowires made in propanol (yield ~ 100%, Figure 4-4c and Figure 4-5). Some morphological details of WS_2 nanotubes made from $W_{18}O_{49}$ nanoparticles obtained under different conditions are compiled in Table 4-2.

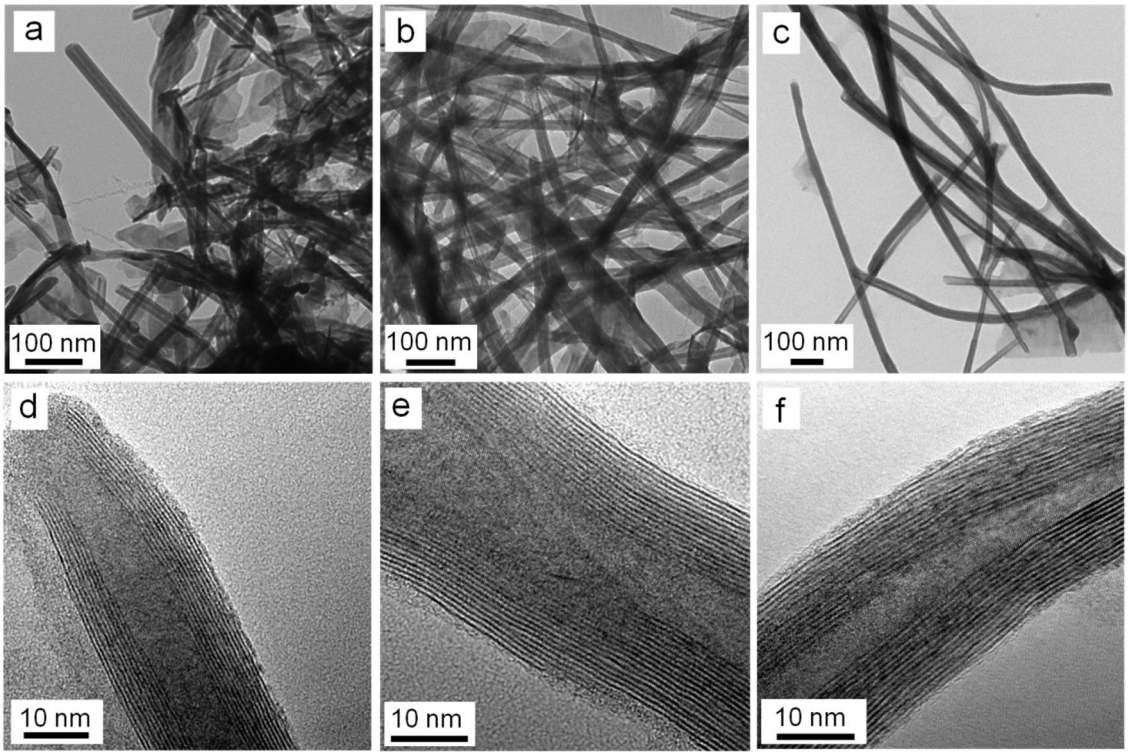

Figure 4-4. (a-c) TEM overview and corresponding (d-f) HRTEM images of WS_2 nanotubes obtained by sulfidization of $W_{18}O_{49}$ nanowires synthesized in (a,d) methanol, (b,e) ethanol and (c,f) propanol.

Table 4-2. Summary of morphological details of WS_2 nanotubes made from $W_{18}O_{49}$ nanowires obtained under different reaction conditions.

X	Y	Morphology of WS_2 nanotubes
MeOH	0.0045	Long/thin, large aspect ratio
EtOH	0.0045	Long/thin, large aspect ratio
PrOH	0.0045	Long/bent, large aspect ratio
c-$C_6H_{11}OH$	0.0045	Poorly crystalline
EtOH	0.0055	Poorly crystalline
EtOH	0.0071	Poorly crystalline (along with nested fullerenes)
EtOH	0.0071[a]	Poorly crystalline

[a] treated at 220°C for 5 h

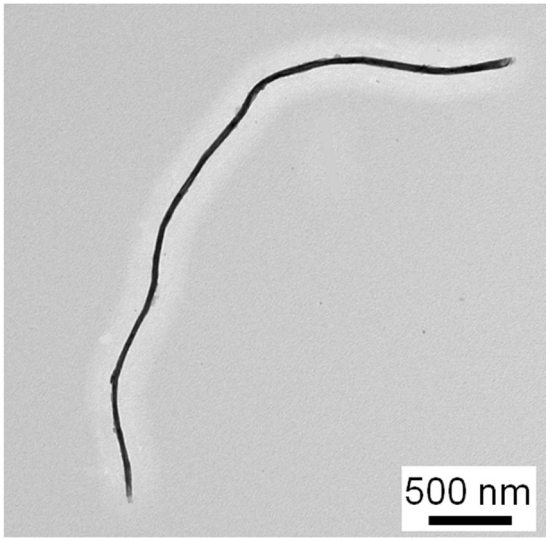

Figure 4-5. TEM image of a micrometer-sized WS_2 nanotube obtained by sulfidization of $W_{18}O_{49}$ nanowires obtained in propanol.

From a mechanistic point of view the sulfidization is assumed to start at the outer surface of the $W_{18}O_{49}$ nanowires [23]. The defects density is dictated (i) by the sulfidization conditions and (ii) the precursor nanoparticles (see Figure 4-6). Under constant sulfidization conditions the precursor particles play a dominant role.

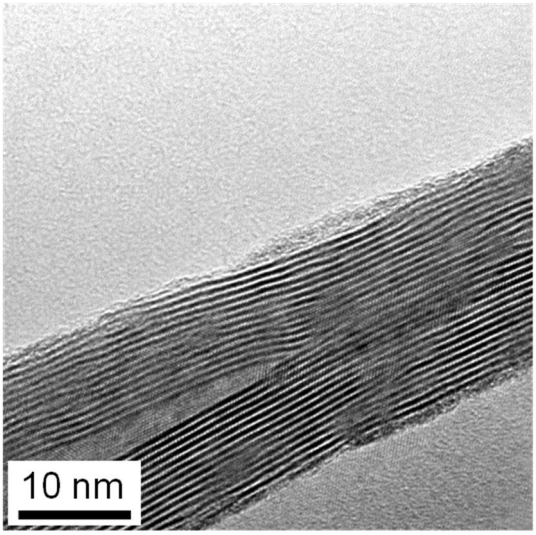

Figure 4-6. HRTEM image of a WS_2 nanotube with defective lumen demonstrating the defects transferred from the nanowire precursor.

WS_2 nanotubes obtained from $W_{18}O_{49}$ nanowires made in ethanol and propanol showed a Moiré -like pattern-like structure (see Figure 4-7a). The HRTEM image of the closed-tip nanotube (Figure 4-7b) revealed a hexagonal dot lattice inside the nanotube. These graphene-type sheets (viewed edge-on) in the walls appear as dotted lines in Figure 4-7b and

lead to a complex Moiré pattern similar to those observed in chiral multiwalled carbon nanotubes (MWCNTs) [37]. As shown in Figure 4-7c, the fast Fourier transform (FFT) of the selected area in Figure 4-7b shows a doublet pattern with three rings (corresponding to *d* values of 2.76 Å, 1.64 Å and 1.4 Å) resulting from the (100), (106) and (114) planes of 2H-WS_2, respectively. The presence of the Moiré-like pattern for the fully sulfidized WS_2 sheets shows the polychirality of the multi-walled WS_2 nanotubes.

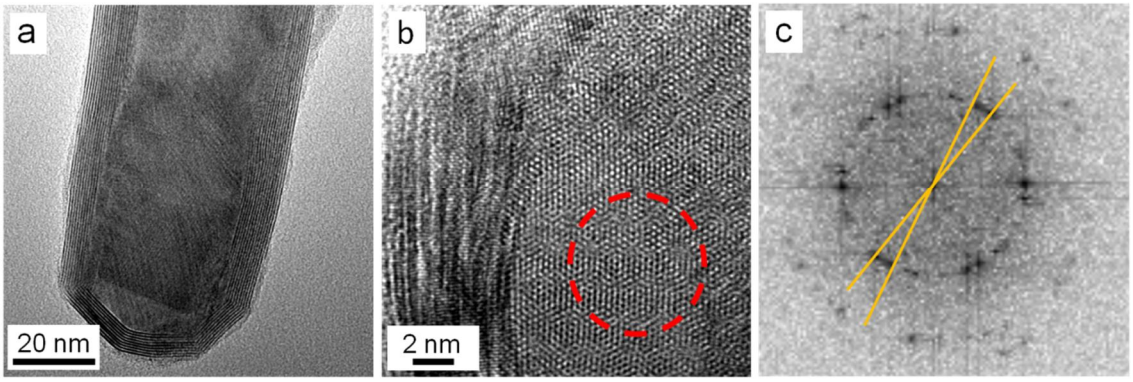

Figure 4-7. (a) TEM overview image of a closed-tip WS_2 nanotube showing the Moiré-like dot pattern in its central part. (b) HRTEM image of the WS_2 nanotube. (c) FFT of the area highlighted by the dashed red circle in (b).

We have also sulfidized synthesized $W_{18}O_{49}$ nanorods obtained by the hot injection approach [33], but attempts to convert these $W_{18}O_{49}$ nanorods to WS_2 nanotubes were unsuccessful (1-2% yield of WS_2 nanotubes, see Figure 4-8), presumably because the thermal decomposition of the oleic acid capping agents during the sulfidization process leads to the formation of a passivating carbon film.

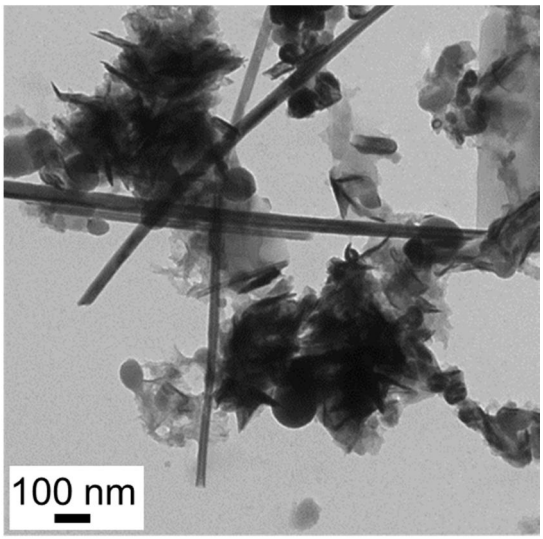

Figure 4-8. TEM image of the product obtained by sulfidization of $W_{18}O_{49}$ nanorods synthesized by hot injection.

Whereas WS_2 nanotubes made by sulfidization from WO_3 nanorods [21-26] can be solubilized only after functionalization with chelating ligands [14,16], the defect-rich WS_2 nanotubes prepared in this work from $W_{18}O_{49}$ nanowires were easily dispersible in organic solvents. Their suspensions were stable for several days (Figure 4-9). Atoms at these defect sites are under-coordinated with dangling bonds, and they tend to be more reactive than those in an equivalent defect-free lattice [38]. As a result they are more prone to adsorb solvent molecules which make them highly dispersible in polar solvents like DMF and DMSO. Our findings are in harmony with a recent report that gold nanoparticles are preferentially adsorbed at defect sites of WS_2 nested fullerenes and nanotubes [20].

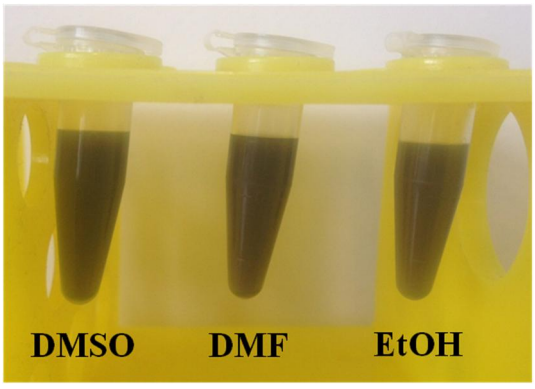

Figure 4-9. Digital photograph showing the dispersibility of defect-rich WS_2 nanotubes in dimethylsulfoxide (DMSO), dimethylformamide (DMF) and ethanol (EtOH) (C=0.10 mg/mL).

The enhanced reactivity of defects in layered chalcogenide nanostructures could be demonstrated by the adsorption of metal, metal oxide and Janus type nanoparticles on defect-rich WS_2 nanotubes (Figure 4-10). The overview TEM images (Figure 4-10 a-c) confirm that the nanotubes are uniformly coated with $Pt@Fe_3O_4$, MnO and Au nanoparticles, respectively. The high resolution TEM images (Figure 4-10 d-f) show the binding of respective nanoparticles in a monolayer manner. The large binding density of the nanoparticles suggests that defects are indeed a tool to decorated WS_2 nanotubes with chalcophilic Pearson-soft nanoparticles.

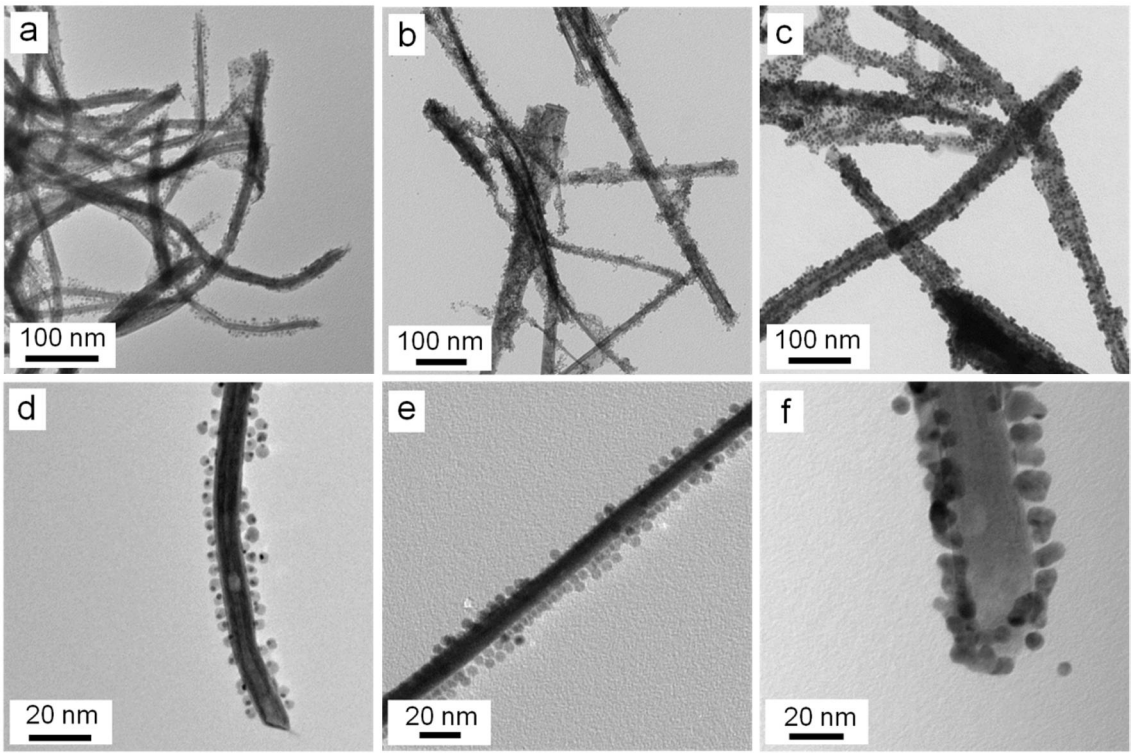

Figure 4-10. TEM image of a WS_2 nanotube having a monolayer with nearly full coverage of (a,d) $Pt@Fe_3O_4$ Janus particles, (b,e) MnO nanoparticles and (c,f) Au nanoparticles.

4.4. Conclusions

We have developed a facile route for the synthesis of highly defective WS_2 nanotubes by the sulfidization of highly defective $W_{18}O_{49}$ tungsten oxide nanoparticles that were obtained by the hydrolysis of WCl_6 in alcohols. The alcohols serve in this reaction as solvents, reducing and hydrolysis agents. Propanol proved the most effective reagent for obtaining $W_{18}O_{49}$ particles with the required anisotropy for the subsequent synthesis of WS_2 nanotubes. Reductive sulfidization of highly anisotropic $W_{18}O_{49}$ nanoparticles (obtained from propanol) leads to the formation of long (several micrometers) and curved WS_2 nanotubes with a large number of defects and dislocations. In contrast, $W_{18}O_{49}$ nanoparticles with a surfactant coating could not be converted to WS_2 nanotubes. Unlike defect-free WS_2 nanotubes the defect-rich nanotubes were highly dispersible in organic solvents, and they could be decorated easily with metal, metal oxide and hybrid metal@metal oxide nanoparticles.

The facile functionalization of chalcogenide nanoparticles opens new fields for this class of materials which have been pursued actively during the past few years for the related carbon nanotubes and various oxide materials: (i) the functionalization of chalcogenide nanotubes for the attachment of electronically active components, light harvesting ligands for solar cell applications to the sidewalls of the tubes, (ii) dispersion of nanotubes, e.g. for the integration in composites which is of interest because of their exceptional mechanical properties. (iii) Furthermore, it allows the fabrication of thin films by surface binding of chalcogenide particles to metal or oxide surfaces, which might allow their use as lubricants.

4.5. References

[1] C. N. R. Rao, M. Nath, *Dalton Trans.* **2003**, 1.

[2] R. Tenne, *Nature Nanotechnol*. **2006**, *1*, 103.

[3] M. N. Tahir, A. Yella, J. Sahoo, H. A. Therese, N. Zink, W. Tremel, *Phys. Status Solidi. B* **2010**, *247*, 2338.

[4] L. Rapoport, Yu. Bilik, Y. Feldman, M. Homyonfer, S. R. Cohen, R. Tenne, *Nature* **1997**, *387*, 791.

[5] J. Tannous, F. Dassenoy, B. Vacher, T. Le Mogne, A. Bruhacs, W. Tremel, *Tribol. Lett.* **2011**, *41*, 55.

[6] O. Tevet, P. Von-Huth, R. Popovitz-Biro, R. Rosentsveig, H. D. Wagner, R. Tenne, *Proc. Natl. Acad. Sci. U. S. A.* **2011**, *108*, 19901.

[7] J. Jang, S. Jeong, B. Park, J. Seo, J. Cheon, M.-C. Kim, E. Sim, Y. Oh, S. Nam, *J. Am. Chem. Soc.* **2011**, *133*, 7636.

[8] Y. Q. Zhu, T. Sekine, K. S. Brigatti, S. Firth, R. Tenne, R. Rosentsveig, H. W. Kroto, D. R. M. Walton, *J. Am. Chem. Soc.* **2003**, *125*, 1329.

[9] S. Gemming, G. Seifert, *Nature Nanotechnol.* **2007**, *2*, 21.

[10] B. Späth, F. Kopnov, H. Cohen, A. Zak, A. Moshkovich, L. Rapoport, W. Jägermann, R. Tenne, *Phys. Status Solidi B* **2008**, *245*, 1779.

[11] S. Kumar, C. Borriello, G. Nenna, R. Rosentsveig, T. Di Luccio, *Eur. Phys. J. B* **2012**, *85*, 160.

[12] A. R. Adini, M. Redlich, R. Tenne, *J. Mater. Chem.* **2011**, *21*, 15121.

[13] C. S. Reddy, A. Zak, E. Zussman, *J. Mater. Chem.* **2011**, *21*, 16086.

[14] M. N. Tahir, M. Eberhardt, N. Zink, H. A. Therese, U. Kolb, P. Theato, W. Tremel, W. *Angew. Chem*. **2006**, *118*, 4927; *Angew. Chem. Int. Ed.* **2006**, *45*, 4809.

[15] M. N. Tahir, N. Zink, M. Eberhardt, H. A. Therese, U. Kolb, P. Theato, W. Tremel, *Small* **2007**, *3*, 829.

[16] M. N. Tahir, F. Natalio, H. A. Therese, A. Yella, M. R. Shah, R. Berger, H.-J. Butt, N. Metz, P. Theato, H. C. Schröder, W. E.G. Müller, W. Tremel, *Adv. Funct. Mater*. **2009**, *19*, 285.

[17] J. K. Sahoo, M. N. Tahir, A. Yella, R. Branscheid, U. Kolb, W. Tremel, *Langmuir* **2011**, *27*, 385.

[18] M. N. Tahir, A. Yella, J. K. Sahoo, F. Natalio, U. Kolb, F. Jochum, P. Theato, W. Tremel, *Isr. J. Chem*. **2010**, *50*, 500.

[19] C. Shahar, D. Zbaida, L. Rapoport, H. Cohen, T. Bendikov, J. Tannous, F. Dassenoy, R. Tenne, *Langmuir* **2010**, *26*, 4409.

[20] C. Shahar, R. Levi, S. R. Cohen, R. Tenne, *J. Phys. Chem. Lett.* **2010**, *1*, 540.

[21] L. Margulis, G. Salitra, R. Tenne, M. Talianker, *Nature* **1993**, *365***,** 113.

[22] Y. Feldman, E. Wasserman, D. J. Srolovitz, R. Tenne, *Science* **1995**, *267***,** 222.

[23] A. Rothschild, J. Sloan, R. Tenne, *J. Am. Chem. Soc.* **2000**, *122*, 5169.

[24] Y. Q. Zhu, W. K. Hsu, N. Grobert, B. H. Chang, M. Terrones, H. Terrones, H. W. Kroto, D. R. M. Walton, *Chem. Mater.* **2000**, *12*, 1190.

[25] H. A. Therese, J. Li, U. Kolb, W. Tremel, *Solid State Sci.* **2005**, *7*, 67.

[26] M. Remskar, M. Virsek, A. Jesih, *Nano Lett.* **2008**, *8*, 76.

[27] C. M. Zelenski, P. K. Dorhout, *J. Am. Chem. Soc.* **1998**, *120*, 734.

[28] M. J. Yacaman, H. Lopes, P. Santiago, D. H. Galvan, I. L. Garzon, A. Reyes, *Appl. Phys. Lett.* **1996**, *69*, 1065.

[29] I. Alexrou, N. Sano, A. Burrows, R. R. Meyer, H. Wang, A. I. Kirkl, C. J. Kiely, G. A. J. Amaratunga, *Nanotechnology* **2003**, *14*, 913.

[30] J. J. Hu, J. E. Bultman, J. S. Zabinski, *Tribol. Lett.* **2004**, *17*, 543.

[31] Y. Mastai, M. Homyonfer, A. Gedanken, G. Hodes, *Adv. Mater.* **1999**, *11*, 1010.

[32] A. Albu-Yaron, C. Levy-Clement, J. L. Hutchison, *Electrochem. Solid-State Lett.* **1999**, *2*, 627.

[33] A. Yella, M. N. Tahir, S. Meuer, R. Zentel, R. Berger, M. Panthöfer, W. Tremel, *J. Amer. Chem. Soc.* **2009**, *48*, 17566.

[34] J. K. Sahoo, M. N. Tahir, A. Yella, T. D. Schladt, E. Mugnaioli, U. Kolb, W. Tremel, *Angew. Chem.* **2010**, *122*, 7517; *Angew.Chem. Int. Ed.* **2010**, *49*, 7578.

[35] J. K. Sahoo, M. N. Tahir, F. Hoshyargar, B. Nakhjavan, R. Branscheid, U. Kolb, W. Tremel, *Angew. Chem.* **2011**, *123*, 12479; *Angew. Chem. Int. Ed.* **2011**, *50*, 12271.

[36] The synthesis of $W_{18}O_{49}$ nanowires has been described by various authors, see for example: (a) G. Xi, S. Ouyang, P. Li, J. Ye, Q. Ma, N. Su, H. Bai, C. Wang, *Angew. Chem. Int. Ed.* **2012**, *51*, 2395. (b) C. Guo, S. Yin, Y. Huang, Q. Dong, T. Sato, *Langmuir* **2011**, *27*, 12172. (c) C. Guo, S. Yin, M. Yan, M. Kobayashi, M. Kakihana, T. Sato, *Inorg. Chem.* **2012**, *51*, 4763. (d) X. W. Lou, H. C. Zeng, *Inorg. Chem.* **2003**, *42*, 6169.

[37] S. Amelinckx, A. Lucas, P. Lambin, *Rep. Prog. Phys.* **1999**, *62*, 1471.

[38] G. Ertl, J. Küppers, *Low Energy Electrons, Surface Chemistry*, 2nd Ed., Verlag Chemie, Weinheim, 1985.

From WO_3 Nanorods to WS_2 Nanocoffins

Associated publication: *manuscript under preparation*

5.1. Introduction

The structural features and growth mechanism of inorganic chalgogenide nanoparticles and nanotubes, first described by Tenne *et al.* [1] have attracted intense interest [2-5]. Among various layered metal chalcogenides, tungsten disulfide (WS_2) and molybdenum sulfide (MoS_2) nanostructures have been of both fundamental and technological interest during the past two decades because of their intriguing physicomechanical properties. For example, WS_2 fullerene-like (IF) nanoparticles can be used as solid lubricants [6]; WS_2 nanotubes can be employed as scanning probe microscope tips [7] and field emitters [8] etc. Single layer MoS_2 could be used as a conductive channel in field-effect transistors as recently described by Kis and coworkers [9]. The current on/off ratio in ambient temperature revealed a mobility close to that achieved in graphene nanoribbons and thin silicon films. This observation might offer the application of metal dichalcogenides monolayers as thin transparent semiconductors in energy harvesting and optoelectronics.

To date, various methods have been advised to produce WS_2 and MoS_2 nanostructures, such as chemical transport [10], gas-solid reactions [11] and in situ heating [12] which leads to IF nanoparticles, short and long nanotubes, nanotube bundles and microtubes [13]. Since the first report on the production of tungsten sulfide nanotubes by Tenne and coworkers in 1992, numerous new types of nanotubes and nanoparticles have been synthesized in recent years using different approaches. Among them, the synthesis of core-shell nanotubes, such as PbI_2@WS_2 [14], the so-called "MoS_2 mama-tubes" [15] and others have been described. However, the right angle tips has been observed in core-shell structures such as niobium-doped tungsten sulfide closed-ended nantubes [16], due to structural defects rising by introduction of dopant within the host crystal structure or in so-called "thick" nanotubes or nanocubes [17]. It had been verified that, rectangular defects can lead to the appearance of vertexes with 90° angles in the IF structures [18,19].

In the current study, we demonstrate the synthesis of the tungsten sulfide nanostructures with 90° apex denoted as "nanocoffins" by sulfidizing the corresponding oxide nanorods. The oxide nanorods were prepared by solvothermal approach using tungsten (V) ethoxide as precursor.

5.2. Experimental Section

5.2.1. Synthesis

Synthesis of WO_3 nanorods. In a glovebox, 0.2 mL of tungsten (V) ethoxide ($W(OEt)_5$, ABCR, 95%) was taken into a syringe and transferred outside the box and immediately dissolved in ~ 12.5 mL of benzyl alcohol (BzOH, Sigma, 99.8%) and the clear solution was transferred into a Teflon lined 50 mL stainless steel autoclave and heated at 200°C for 25 h. After this time, the autoclave was cooled back to the room temperature normally. After cooling to the room temperature, the greenish yellow precipitate was collected by centrifugation at 9000 rpm for 10 min, washed twice with ethanol and dried at 60°C.

Synthesis of WS_2 nanocoffins. The nanorods obtained from the first step were taken in a corundum boat and kept inside a quartz tube which was flushed with argon for half an hour prior to the heating to remove any oxygen. The corundum boat was kept at the middle of a tube furnace and heated up to 850°C at the rate of 5°C/min under constant argon flow. Just before reaching to 850°C, the argon was switched to H_2S gas with a flow rate of 40 sccm and kept at this temperature for half an hour. During the sulfidization, the H_2S flow was carefully controlled using a flowmeter. After half an hour, the furnace was cooled to ambient temperature at the rate of 5°C/min under argon flow. The black powder obtained after cooling was collected and was used for the further characterization.

5.2.2. Material Characterization

X-ray Powder Diffraction. X-ray diffraction patterns (XRD) were recorded using a Siemens D5000 diffractometer equipped with a Braun M50 position sensitive detector in transmission mode using Ge (200) monochromatized CuKα radiation. Samples were prepared between two layers of Scotch Magic Tape. Crystalline phases were identified according to the PDF–2 database using Bruker AXS EVA 10.0 software.

Electron Microscopy. Low resolution transmission electron microscopy was performed on a Phillips EM-420 equipped with a slow scan CCD detector (1k x 1k) and a LaB_6 electron gun operated with an acceleration voltage of 120 kV. Transmission electron microscopy (TEM) images were processed with the Gnu Image Manipulation Program GIMP Version 2.6.8 or with Image J Version 1.43u. High resolution transmission electron microscopy (HRTEM) images were taken with a FEI TECNAI F30 ST electron microscope (field-emission gun, 300 kV extraction voltages) equipped with a STEM high angular annular dark field detector and an Oxford energy-dispersive X-ray (EDX) spectrometer with a Si/Li detector and an ultrathin

window for elemental analysis. HRTEM and electron diffraction were recorded by a GATAN CCD camera (14-bit 794MSC, 1024 × 1024 pixels). TEM grids were prepared by dispersion of the sample in ethanol and drop casting on 300 mesh carbon coated copper grids.

Automated Diffraction Tomography (ADT). ADT data acquisition was performed with a FISCHIONE tomography holder, using the ADT acquisition module described in ref. [20] and [21]. ADT-3D software package was used for three-dimensional diffraction volume reconstruction and visualization [22].

5.3. Results and Discussion

The first step involves a solvothermal approach to obtain tungsten oxide nanorods by alcoholysis of $W(OEt)_5$ at 200°C for 25 h. The greenish yellow powder obtained after the solvothermal reaction was investigated by XRD, TEM and HRTEM. Figure 5-1 shows the X-ray powder diffraction pattern obtained from the greenish yellow powder. According to full pattern profile analysis, the XRD pattern is a superposition of the diffraction patterns of the monoclinic phase of WO_3 (approx. 55%, crystallite size 83 nm) and orthorhombic hydrated tungsten oxide phase, that is, $WO_3 \cdot {}^1/_3H_2O$ (ca. 45%, crystallite size 72 nm).

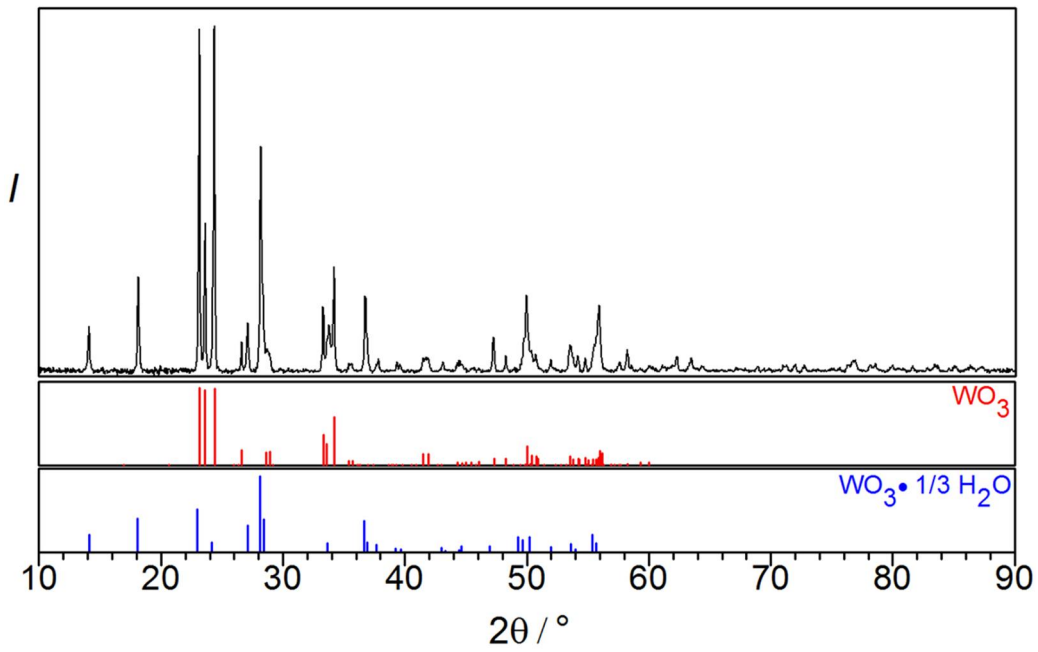

Figure 5-1. X-ray powder diffraction pattern (black) of the product obtained from the solvorthermal treatment. The red line shows the reflections from WO_3 (PDF-2 File Card No. 43-1035) and the blue reflections corresponds to the tungsten oxide hydrate, $WO_3 \cdot 1/3H_2O$ (PDF-2 File Card No. 1-072-0199).

The TEM images in Figures 5-2 a-b show the typical morphology of the as-synthesized precursors. The nanorods are ca. 150 nm in width and several hundred nanometers in length occasionally stacking and ordering along a common direction. HRTEM shows that partial volumes of the nanorods consist of a bulky crystalline domains with lattice fringes coherent with the lattice parameters of WO_3 (Figure 5-2c). In contrast, other areas show disorder features as undulated layers, faults and layer closures (Figures 5-2 c-d). The most disordered areas correspond usually to regions close to the rod rims.

Three dimensional diffraction volumes acquired and reconstructed by ADT (Figures 5-2 e-f) reveal that a typical rod consists in fact of two different lattices, respectively corresponding to the crystal structures of WO_3 (WO, space group $P2_1/n$, a=7.297Å, b=7.539Å, c=7.688Å, β=90.91° [23]) and $WO_3 \cdot {}^1/_3H_2O$ (WOH, space group *Fmm2*, a=7.359Å, b=12.513Å, c=7.704Å [24]). The two lattices have related cell parameters and orientation. In fact the cell vectors have approximately the same orientation and the two lattices can be distinguished only by the different length of **b***. This result is supported by the analysis of the fast Fourier transforms (FFT) of HRTEM images (insets in Figure 2b-c). The FFT from more disordered areas show a progressive weakening of reflections 0*kl* with $k+l = 2N+1$ (consistently with the face-centering of WOH lattice) and diffuse scattering appear along **b***. The disordered areas correspond therefore to the hydroxidated areas. In order to support this idea, the hydratation of WO was further studied in details as demonstrated in Figure 5-3. The HRTEM image of a typical nanorod is shown in Figure 5-3a. The main direction of growth is [001]. It is notable that the disorder is always along b* that is orthogonal to the growth direction. According to FFT analysis on the areas 1 and 2, the apex (001) of the rods is WO (Figure 5-3b), while the long sides (010) transform easily to WOH (Figure 5-3c). Figure 5-3d shows an unusual orientation along [010]. Right in the middle, where we have only WO, the extinction rule for *h0l* is $h+l = 2N$, consistent with space group $P2_1/n$ (Figure 5-3f). The same is observed along (001) that in not affected by the hydratation (Figure 5-3g). On the contrary, along (100) the extinction rule for *h0l* is $h,l = 2N$, consistent with space group *Fmm2*, i.e. WOH (Figure 5-3e). This means that the transformation from WO to WOH along (100) is complete.

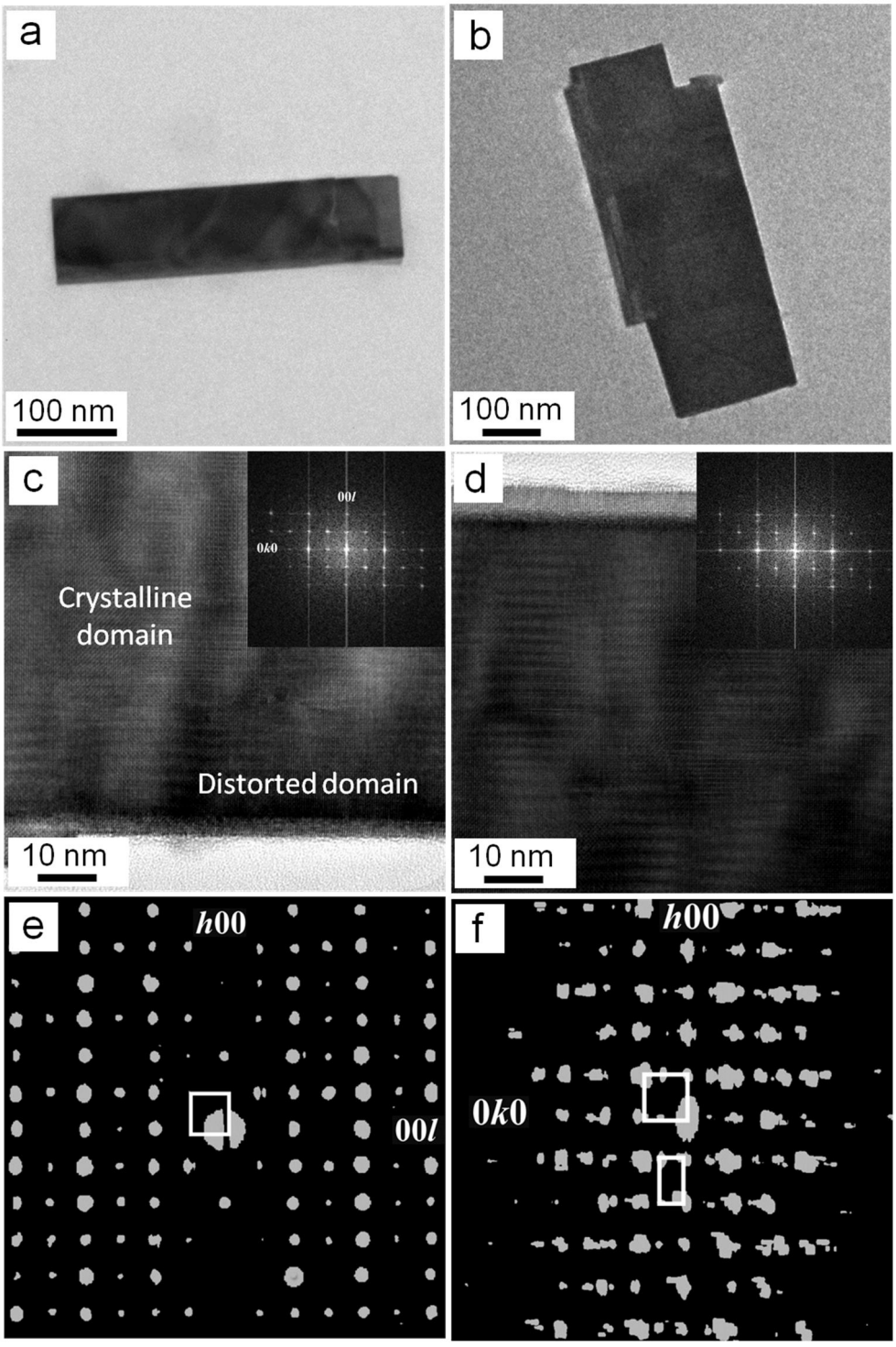

Figure 5-2. Nanorod precursor from solvothermal treatment. (a) and (b) TEM images of typical as-synthesized rod, (c) HRTEM of a rod showing a bulky crystalline domain (up) next to a more disordered domain (down). The disordered domain is close to the rim of the rod. The inset shows the FFT of the ordered upper part, consistent with [100] of WO_3, (d) HRTEM of a disordered area and correspondent FFT, (e) three-dimensional ADT reconstructed diffraction volume collected on a rod and projected along b* showing how WO_3 and W_3O_9•H_2O lattices overlap in this direction, (f) projection of the same diffraction volume along c* showing the two lattices of WO_3 and W_3O_9•H_2O. ADT images are realized with ADT3D software.

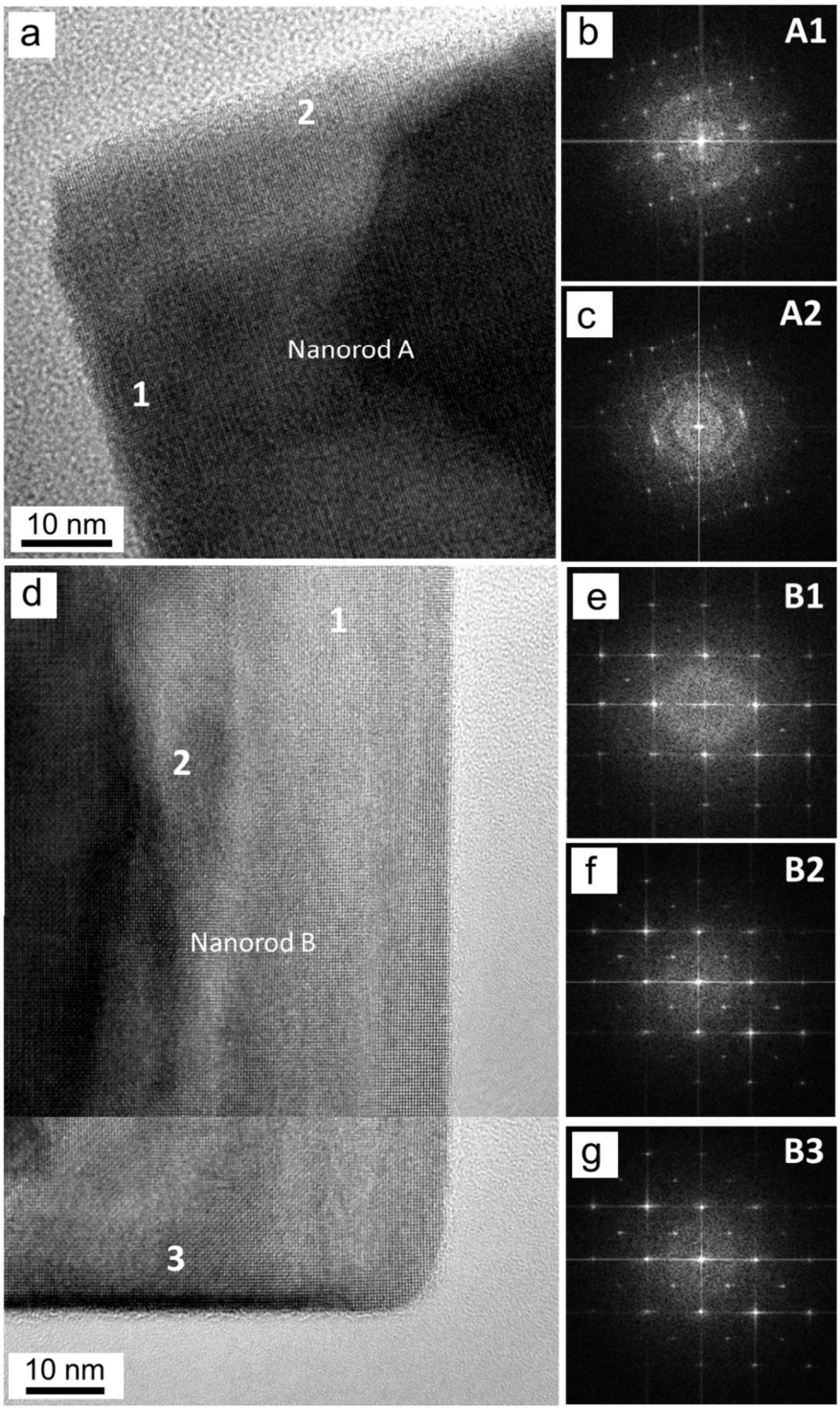

Figure 5-3. Two different nanorods. Nanorod A: (a) HRTEM image of the nanorod showing the orientation along [010], NED from the area (b) A1 and (c) A2, Nanorod B: (d) HRTEM image of the nanorod orienting along [010], NEDs from the area (e) B1, (f) B2, (g) B3.

Previously, we had refined the oxide–sulfide conversion method and successfully created very long pure WS_2 nanotubes by forming WO_x nanorods prior to oxide-sulfide conversion [25]. Here in the present work, the presence of gaseous H_2S in the chamber facilitated

oxide-to-sulfide conversion and resulted in formation of WS_2 nanocoffins. As shown in Figure 5-4, the X-Ray powder diffraction pattern obtained after sulfidization matches with that of a 1:1 mixture of WS_2-2H and WS_2-3R phase. A slight expansion along the stacking direction [001] of 0.3% and 1.7% was observed for WS_2-3R and WS_2-2H phases, respectively.

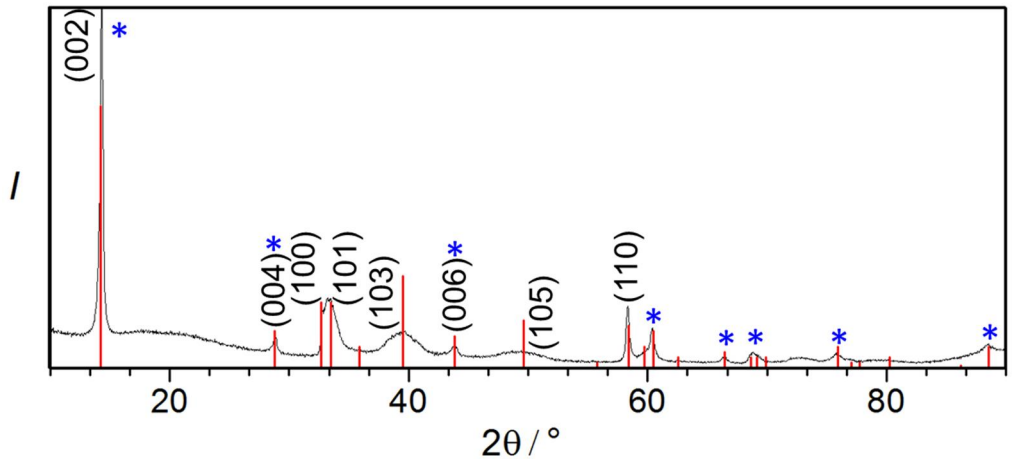

Figure 5-4. X-ray powder diffraction pattern of the product obtained after sulfidisation of the oxide nanorods (black). The red bars correspond to WS_2-2H phase (PDF-2 File Card No. 8-0237) and the blue asterisks indicate superposition of the reflections from WS_2-3R (PDF-2 File Card No. 35-0651).

The sulfidization of the tungsten oxide nanorods resulted in the formation of nanocoffins with approximately the same dimensions observed for the oxide precursor. One such nanocoffin is displayed in Figure 5-5a and b. The notability of WS_2 nanocoffins is related not only to their size, which distinguishes them from standard known closed-tipped nanotubes, but also to the fact that their apexes form systematically a ninety degree angle as displayed in Figure 5-5c.
EDX analysis shows that the walls of the coffins are made of WS_2. The inner part delivers a weaker signal, showing that the coffins have an empty, or at least less dense, internal volume (Figure 5-5d). Additionally a weak signal of oxygen is detectable from the inner part.
Conventional NED patterns show that the external walls of the coffins are made of layered WS_2 with typical interplanar distances of 0.63 nm. 3D reconstructions of the scattering image from ADT data of an area with an atypically thick wall reveal a hexagonal lattice (Figure 5-5 e-f). Despite a strong diffuse scattering along **c***, the main periodicity reveal that the predominant polytype, at least in the analyzed coffins, is the rhombohedral one [26].

The inner part of the coffins produces a ring-like pattern that can be indexed with *hk*0 reflection of WS_2 (Figure 5-5g). Tilting the sample the circular rings change to ellipses (Figure 5-5h). Floor (and eventually roof) of the coffins might therefore be made of layers of WS_2 stacked with a diffuse rotational disorder. All the layers lie on the (001) face and have random **a** and **b** orientations. The internal volume of the coffin does not give rise to diffraction intensities. The weak EDX signal from oxygen suggests small parts of an oxidic phase remaining inside the nanocoffins.

In some cases, the shorter wall contains fewer layers than the longer wall which indicates differential transformation rates for shorter and longer nanocoffin walls. In other words, the growth rate is not the same for adjacent walls and this leads to fusion of two walls with different wall thicknesses (Figure 5-6a). In a few cases of this type, the shorter wall is considerably buckled (Figure 5-6b). The formation of buckles shows that the thinner walls might cause a lateral strain at the wall corners leading to a negative curvature inward the nanocoffin structure. In addition to single nanocoffins, WS_2 layers appear to be included in the nanocoffin itself as well. Careful inspection of such samples points to the fact that several nanocoffins are likely to be fused into each other making a “twin” nanocoffins, sharing a common wall along their main axis (Figure 5-6c). A magnified TEM view of the T-shape junction is demonstrated in Figure 5-6d. These structures might be formed when the fast growth in plane favors the fusion of crossing sulfide walls. Nevertheless, some deviations from 90° could be observed among the outer layers where the rectangular shape of the inner layers might change to curved kinks (see Figure 5-7).

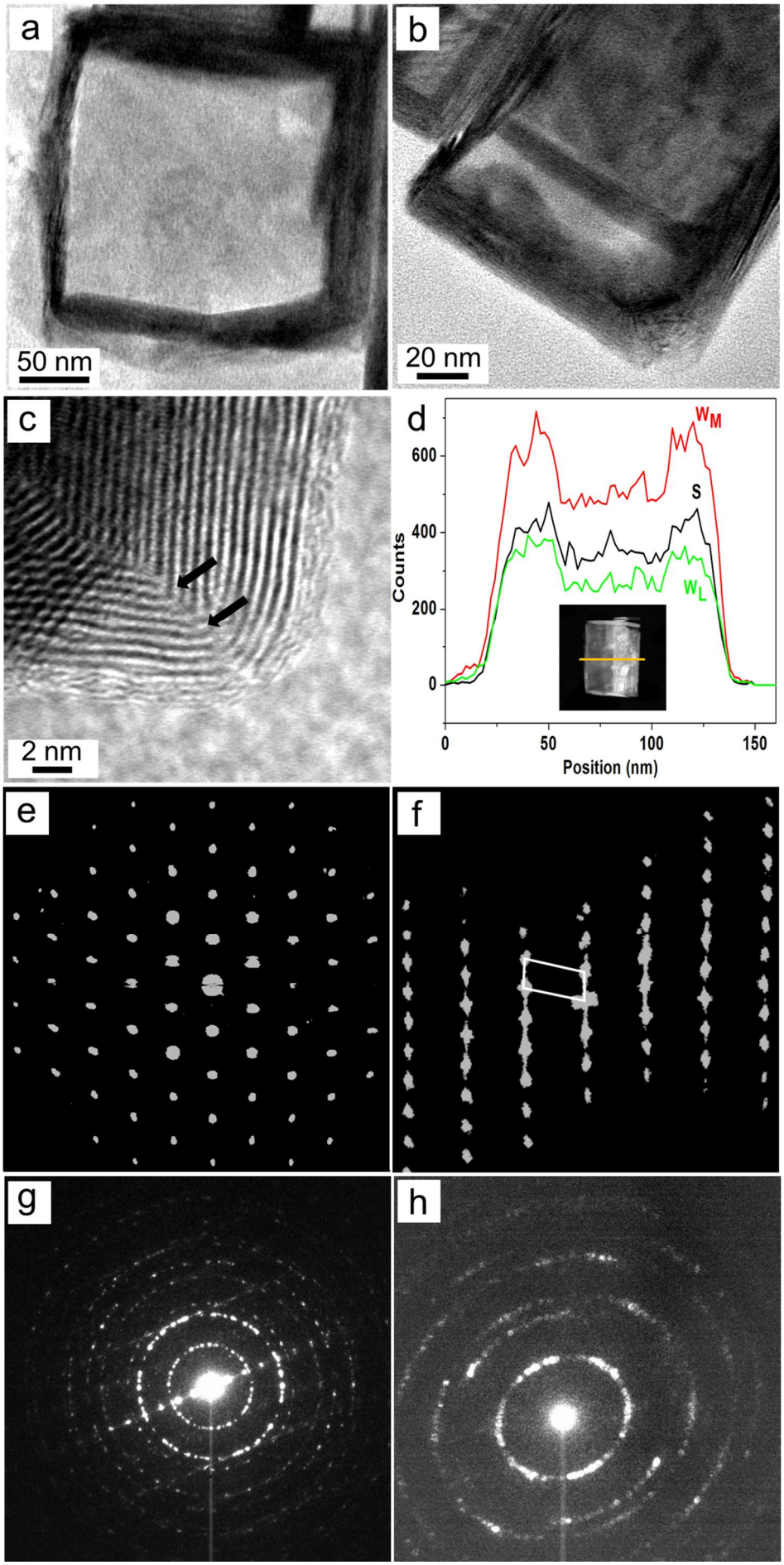
a
50 nm
b
20 nm
c
2 nm
d
W_M
S
W_L
Counts
600
400
200
0
0
50
100
150
Position (nm)
e
f
g
h

Figure 5-5. Nanocoffins. (a) and (b) TEM images of typical nanocoffins, (c) HRTEM showing the right angle edge of a coffin, (d) EDX profile across the coffin shown in the STEM image in inset, (e) three-dimensional ADT reconstructed diffraction volume collected on a wall and projected along c*, (f) the same diffraction volume showing the diffuse scattering along c* and the rhombohedral arrangement of the prominent reflections, (g) NED from a coffin collected at 0° of tilt. The rings correspond to the *hk0* reflection of WS_2 and are originated by the floor of the coffin, while the line of reflections originates from a wall and corresponds to a distance of 0.63 nm, typical of WS_2 layers, (h) NED from the internal volume of a coffin after a tilt of 20°, where the diffraction rigs corresponding to the *hk0* reflections turn into ellipses due to the oblique cut.

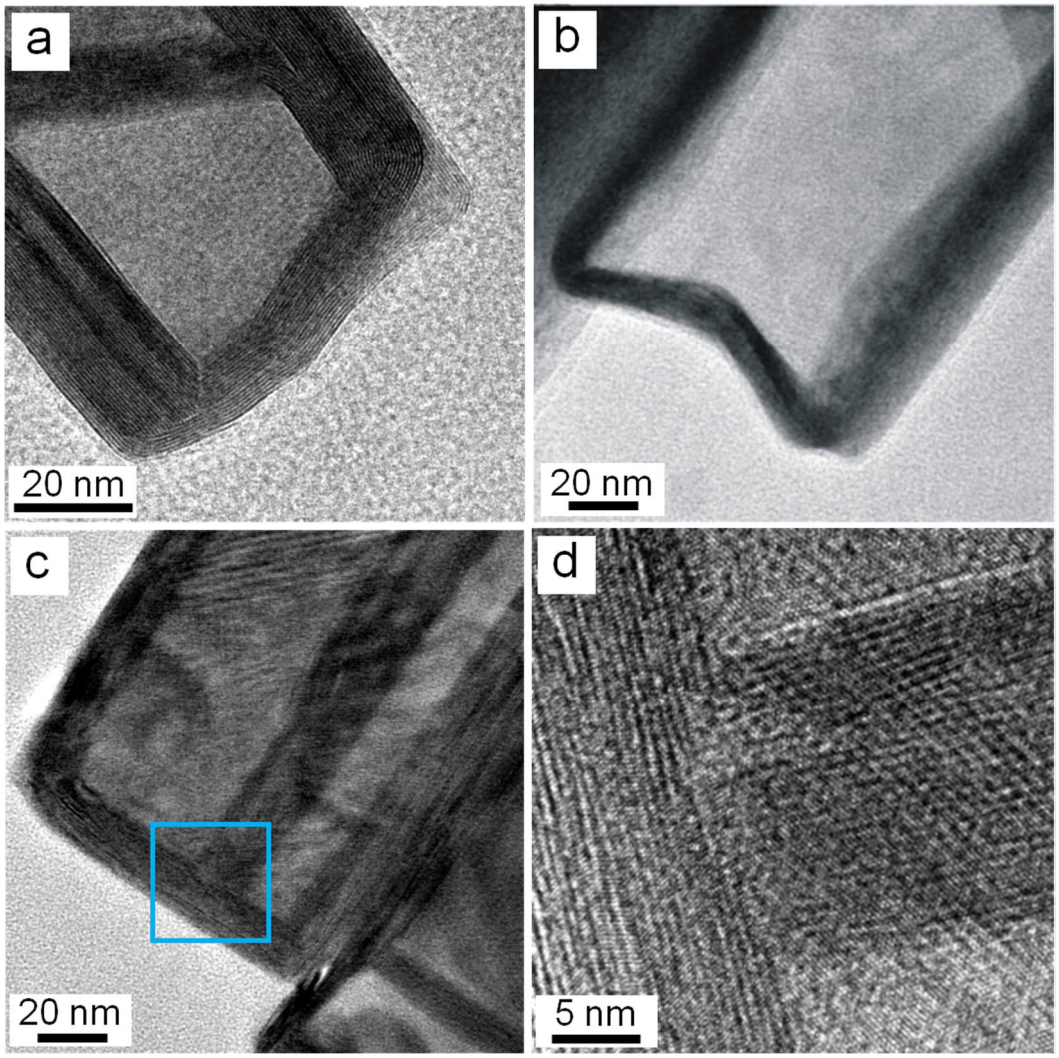

Figure 5-6. HRTEM image of nanocoffin closures. (a) mismatch in the number of sulfide layers forming a kink, (b) a buckled tip, (c) a twin nanocoffin and (d) magnified view of the T-shape junction.

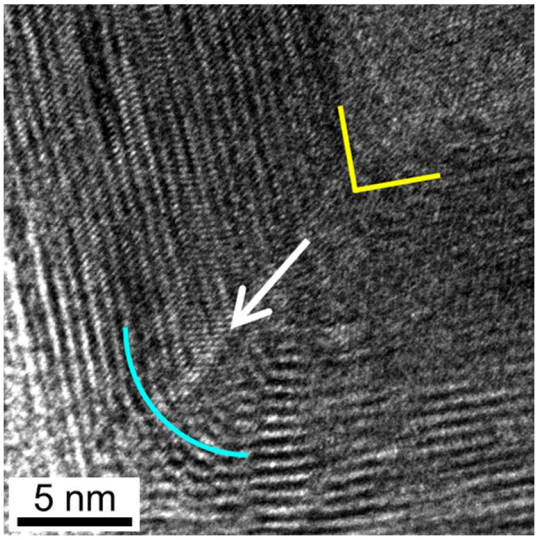

Figure 5-7. Cross section of a nanocoffin at the final steps of sulfidization exhibiting the curved kinks instead of right angles the outer layers.

In order to achieve a better understanding upon the formation mechanism of WS_2 nanocoffins, the sulfidization time was shortened and intermediate products were collected after 10 and 20 min of sulfidization. HRTEM investigations on these intermediate products shows that the wall of the coffins are already present but they are made of few layers and are not continuous around the perimeter (Figure 5-8a). NED and EDX are comparable with the ones obtained for the final product. No diffraction from other phases than WS_2 was detected. EDX spectra show the presence of O, S and W, with W and S signals that grows in correspondence of well-formed coffin walls (Figure 5-8b). These data show that the nanocoffins are on the pathway to form complete rectangular shapes which occurs after about 30 min. Nevertheless, the prolonged sulfidization leads to no significant change in phase purity or morphology of the nanocoffins.

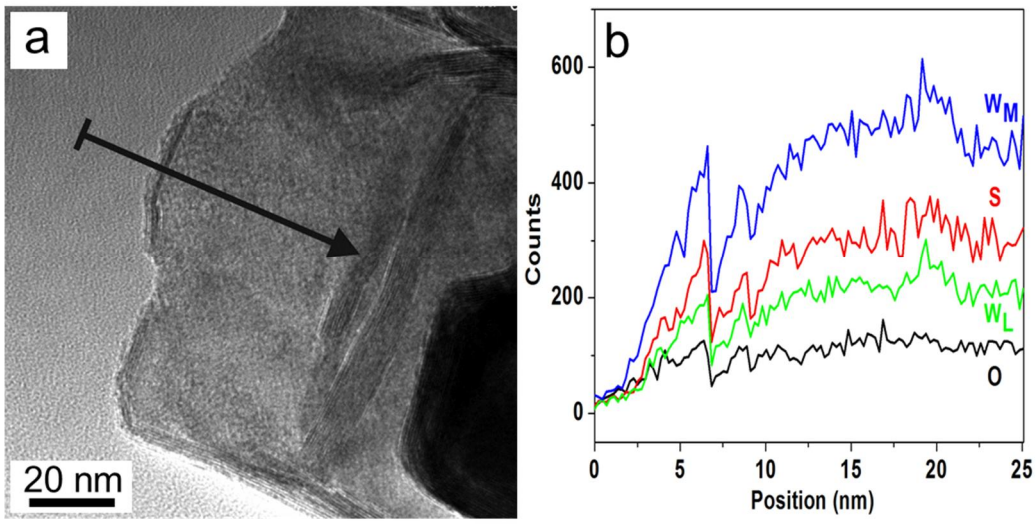

Figure 5-8. Intermediate product during the sulfidization process. (a) HRTEM image showing a thin WS_2 forming around a coffin and track of the EDX profile shown in the next panel, (b) EDX profile showing the increment of S and W signal in correspondence of the WS_2 wall.

The proposed formation mechanism could be as illustrated in Scheme 5-1. Monoclinic WO_3 can be transformed into well crystalline slabs of WS_2 with no crystallographic relation between WS_2 and WO_3 which lead to the (frequently) seen octahedral, onion type fullerenes, giant fullerenes and tubes (that truly are rolls). The intermediate step involves weathering of the monoclinic WO_3 surface in a topotactic reaction to $WO_3 \cdot {}^1/_3H_2O$ and the subsequent topotactic dehydration of $WO_3 \cdot {}^1/_3H_2O$ to hexagonal WO_3 [27] leads to nanorods whose surface allows for the epitaxial induction of WS_2 on these (h-) WO_3 nanorods. Initially formed platelets of WS_2 exhibit a preferred orientation with respect to the nanorod surface, yet they do not wrap the nanorods fully which allows for an ongoing conversion of high density WO_3 cores (0.075 atoms/$Å^3$) into the low density WS_2 (0.055 atoms/$Å^3$). After full conversion, the individual WS_2 platelets coalesce to closed shells to reduce the overall number of dangling bonds. At the tip of the former WO_3 rods this enforces the formation of 90° kinks (arrowed in Figure 5c) finally leading to rectangular WS_2 boxes.

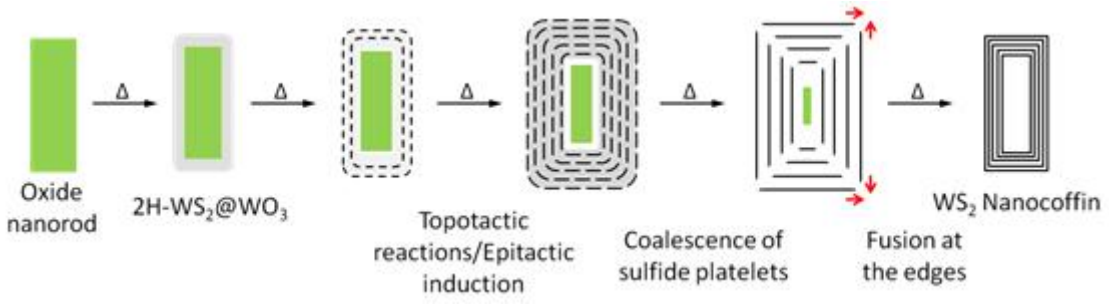

Scheme 5-1. Schematic of the formation mechanism of WS_2 nanocoffins.

5.4. Conclusions

In conclusion, we have demonstrated the formation of tungsten sulfide nanocoffins by sulfidization of tungsten oxide (WO_3) nanorods covered by a hydration crust of $WO_3 \cdot {}^1/_3H_2O$. The conversion of solvothermally-derived tungsten oxide nanorods was carried out in a horizontal furnace to obtain tungsten sulfide nanocoffins in substantial amounts at 850°C. Automated diffraction tomography was used to study the plausible growth mechanism of such unconventional hollow structures. The data acquired by ADT and NED on the tungsten oxide precursor basically shows that the rods mostly grow along *00l* and the hydratation affects (100) and (010), which are normally the larger facets. However, WO_3 and $WO_3 \cdot {}^1/_3H_2O$ crystallites are orientated the same. Thus, the growth of $WO_3 \cdot {}^1/_3H_2O$ on WO_3 seems to be a topotactical reaction. At the initial steps of sulfidization, $WO_3 \cdot {}^1/_3H_2O$ transforms into h-WO_3 whose surface allows for the epitaxial induction of WS_2. Initially formed platelets of WS_2 exhibit a preferred orientation with respect to the nanorod surface. Finally, the individual layers of WS_2 coalesce to form seamless closed shells. In conclusion, a cascade of topotactic reaction leads to epitactic induction and thus the formation of closed rectangular boxes made from hexagonal layers.

5.5. References

[1] R. Tenne, L. Margulis, M. Genut, G. Hodes, *Nature* **1992**, *360*, 444.

[2] L. Rapoport, Y. Feldman, M. Homyonfer, H. Cohen, J. Sloan, J. L. Hutchison, R. Tenne, *Wear* **1999**, *229*, 975.

[3] G. Seifert, H. Terrones, M. Terrones, G. Jungnickel, T. Frauenheim, *Solid State Commun*. **2000**, *114*, 245.

[4] J. Sloan, J. L. Hutchison, R. Tenne, Y. Feldman, T. Tsirlina, M. Homyonfer, *J. Solid State Chem.* **1999**, *144*, 100.

[5] Y. Q. Zhu, W. K. Hsu, H. Terrones, N. Grobert, B. H. Chang, M. Terrones, B. Q. Wei, H. W. Kroto, D. R. M. Walton, C. B. Boothroyd, I. Kinloch, G. Z. Chen, A. H. Windle, D. J. Fray, *J. Mater. Chem.* **2000**, *10*, 2570.

[6] L. Rapoport, Y. Bilik, Y. Feldman, M. Homyonfer, S. R. Cohen, R. Tenne, *Nature* **1997**, 387, 791.

[7] A. Rothschild, S. R. Cohen, R. Tenne, *Appl. Phys. Lett.* **1999**, *75*, 4025.

[8] X.-L. Li, J.-P. Ge, Y.-D. Li, *Chem. Eur. J.* **2004**, *10*, 6163.

[9] (a) B. Radisavljevic, A. Radenovic, J. Brivio, V. Giacometti, A. Kis, *Nature Nanotech.* **2011**, *6*, 147. (b) B. Radisavljevic, M. B. Whitwick, A. Kis, *ACS Nano*, **2011**, *5*, 9934.

[10] A. Rothschild, G. L. Frey, M. Homyonfer, R. Tenne, M. Rappapport, *Mater. Res. Innov*. **1999**, *3*, 145.

[11] M. Homyonfer, B. Alperson, Y. Rosenberg, L. Sapir, S. R. Cohen, G. Hodes, R. Tenne, *J. Am. Chem. Soc*. **1997**, *119*, 2693.

[12] Y. Q. Zhu, W. K. Hsu, N. Grobert, B. H. Chang, M. Terrones, H. Terrones, H. W. Kroto, D. R. M. Walton, B. Q. Wei, *Chem. Mater*. **2000**, 12, 1190.

[13] M. Remskar, Z. Skraba, M. Regula, C. Ballif, R. Sanjines, F. Levy, *Adv. Mater*. **1998**, *10*, 246.

[14] R. Kreizman, S.-Y. Hong, J. Sloan, R. Popovitz-Biro, A. Albu-Yaron, G. Tobias, B. Ballesteros, B. G. Davis, M. L. H. Green, R. Tenne, *Angew. Chem.* **2009**, *121*, 1256; *Angew.Chem. Int. Ed*. **2009**, *48*, 1230.

[15] M. Remskar, A. Mrzel, M. Virsek, A. Jesih, A. *Adv. Mater*. **2007**, *19*, 4276.

[16] Y. Q. Zhu, W. K. Hsu, S. Firth, M. Terrones, R. J. H. Clark, H. W. Kroto, D. R. M. Walton, *Chem. Phys. Lett*. **2001**, *342*, 15.

[17] (a) A. Rothschild, R. Popovitz-Biro, O. Lourie, R. Tenne, *J. Phys. Chem. B* **2000**, *104*, 8976. (b) S. Bastide, D. Duphil, J.-P. Borra, C. Levy-Clement. *Adv. Mater.* **2006**, *18*, 106.

[18] L. Margulis, G. Salitra, R. Tenne, M. Talianker, *Nature* **1993**, *365*, 113.

[19] P. A. Parilla, A. C. Dillon, K. M. Jones, G. Riker, D. L. Schulz, D. S. Ginley, M. J. Heben, *Nature* **1999**, *397*, 114.

[20] U. Kolb, T. Gorelik, C. Kubel, M. T. Otten, D. Hubert, *Ultramicroscopy* **2007**, *107*, 507.

[21] U. Kolb, T. Gorelik, M. T. Otten, *Ultramicroscopy* **2008**, *108*, 763.

[22] U. Heil, S. Schlitt, U. Kolb, T. Gorelik, E. Mugnaioli, E. Schömer, *ADT-3D. A software package for ADT data Visualizing and processing*, Cooperation with the Institute of Computer Science, Johannes Gutenberg University of Mainz: Mainz, Germany, 2009.

[23] B. Loopstra, P. Boldrini, *Acta Crystallogr.* **1966**, *21***,** 158.

[24] B. Gerand, G. Nowogrocki, M. Figlarz, *J. Solid State Chem.* **1981**, *38*, 312.

[25] (a) H. A. Therese, J. Li, U. Kolb, W. Tremel, *Solid State Sciences* **2005**, *7*, 67. (b) A. Yella, E. Mugnaioli, M. Panthöfer, U. Kolb, W. Tremel, *Angew. Chem.* **2010**, *122*, 3373; *Angew. Chem. Int. Ed.* **2010**, *49*, 3301.

[26] W. J. Schutte, J. L. De Boer, F. Jellinek, *J. Solid State Chem.* **1987**, *70*, 207.

[27] B. Gerand, G. Nowogrocki, J. Guenot, M. Figlarz, *J. Solid State Chem.* **1979**, *29*, 429.

Graphene-type Sheets of $Nb_{1-x}W_xS_2$: Synthesis and *in situ* Functionalization

Associated publication: *Dalt. Trans.*, **2012**, *submitted*

6.1. Introduction

Graphene, a single sheet of graphite with two-dimensional (2D) structure, bears exceptional mechanical, thermal and electronic properties [1]. Chemical functionalization of graphene has provided the possibility to tailor these properties in a specific manner. The discovery of graphene by Geim and co-workers in 2004 [2] attracted worldwide attention of scientists to exploit inorganic graphene analogues such as BN [3], MoS_2 [4], WS_2 [5], Bi_2Te_3 [6] and other layered metal chalcogenide nanostructures. Layered metal chalcogenide nanoparticles are the inorganic congeners of carbon nanotubes and nested fullerenes [7]. Inorganic nanotubes (NT) and fullerene-like nanoparticles (IF) form closed hollow structures consisting of two-dimensional slabs formed by two layers of close-packed chalcogenide atoms sandwiching one metal layer between them. These MQ_2 slabs are stacked with just van der Waals contacts between them. The particular architecture of layered metal chalcogenide nanoparticles paved the way for a wide range of applications such as lubrication fluids [8], energy storage [9], medical coatings and drug delivery [10] by displaying high surface area, self-lubricating behavior, *i.e.* low friction and wear, and, in the case of photo-related applications, strong absorption in the solar spectrum.

It was shown that 2D single layers of layered metal chalcogenides display altered or even enhanced properties compared to bulk material highlighting the novelty and advantages of nanostructured materials, i.e. MoS_2 in its bulk form is a semiconductor with an indirect bandgap of 1.2 eV whereas the MoS_2 monolayer is a direct-gap semiconductor with a bandgap of 1.8 eV [11]. Consequently, a strong photoluminescence was observed in single layer MoS_2 due to the direct band transition which is absent for bulk MoS_2 [12]. Recently, Kis and coworkers [13] reported the first field-effect transistor consisting of a 2D single layer of the semiconductor MoS_2 as a conductive channel and HfO_2 as a gate insulator. The device exhibited a current on/off ratio at room temperature with a mobility close to that achieved in thin silicon films or graphene nanoribbons. Therefore, this approach may be useful for the construction of thin transparent semiconductor devices as needed in energy harvesting and optoelectronics.

The synthesis of graphene-type inorganic nanomaterials like BN, MoS_2, WS_2, $NbSe_2$ and Bi_2Te_3 have been well described either by intercalation of alkali metals followed by exfoliation in water [14] or by hydrothermal treatment [14b]. It is interesting to note that these materials can be efficiently dispersed in different solvents and therefore be deposited as individual flakes or formed into films [14a].

The incorporation of metal nanoparticles into the surfaces of semiconductors can enhance their electronic, optical, mechanical and chemical properties. The synthesis of nanocomposites composed of single-layer inorganic sheets decorated with metal nanoparticles like Au, Ag, and Ni may pave the way to explore different new applications. Thesynthesis of such nanocomposite materials is still a challenge and there is an ever growing need to develop synthetic protocols for these hybrid nanocomposites.

6.2. Experimental Section

6.2.1. Materials and Methods

Ammonium niobate (V) oxalate ($C_4H_4NNbO_4.xH_2O$, 99.99%, Sigma Aldrich), citric acid anhydrous ($C_6H_8O_7$, ≥99.5%, Fluka), hexadecylamine ($CH_3(CH_2)_{15}NH_2$, 98%, Sigma Aldrich), ethanol (P.A. VWR), chloroform (99.3%, VWR), tungsten (VI) chloride (WCl_6, 99%, Acros), n-butyllithium (1.6M solution in hexane, Acros), hexane (98.98%, Fisher), sodium borohydride ($NaBH_4$, 99%, Sigma Aldrich), gold (III) chloride hydrate ($AuCl_3.5H_2O$, 99.99%, Sigma Aldrich) were used as received without further purification.

Synthesis of $Nb_{1-x}W_xS_2$ CRNWs The niobium tungsten sulfate nanowires were synthesized by a 3-step reaction as described previously [18].

6.2.2. Synthesis

Synthesis of Nb_2O_5 Nanorods. 1.254 g of ammonium niobium oxalate and 1.814 g of citric acid were weighed in a beaker to which 25 mL of deionized water were added and stirred at room temperature until the precursor was dissolved in water and a clear solution was obtained. The mixture was then heated up to 60˚C under constant low stirring for about 5-6 h which led to the formation of a gel. A solution of hexadecylamine (1.5 g) in 60 mL of ethanol was added and stirred overnight. The resulting mixture was sealed in a 50 mL Teflon lined autoclave, and the autoclave was heated to 180°C and kept at this temperature for 24 h. The autoclave was cooled to room temperature normally and the yellowish white product obtained was washed with ethanol and chloroform to remove the organics. The product was further annealed at 550°C for 1 h under argon for further purification and the white powder was collected.

Synthesis of $WO_x@Nb_2O_5$ Nanorods. 25 mg of annealed Nb_2O_5 were sonicated in 35 mL ethanol for 15 min and then 80 mg tungsten (VI) chloride were added to the solution, and the mixture was sonicated for 20 min until the color of the solution changed from yellow to blue.

The resulting solution was transferred into a 50 mL Teflon lined autoclave and heated to 180°C for 15 h and cooled to room temperature normally. The blue product obtained was washed two times with ethanol and dried in the oven at 60˚C.

Sulfidization of WO_x@Nb_2O_5 Nanorods. The product obtained from the second step was placed in the middle of a corundum boat which was then placed in a small quartz tube and the smaller tube was placed in a bigger glass tube in a way that the corundum boat is located exactly in the middle of the conventional furnace. Before heating up, the setup was flushed with argon for at least half an hour to remove any oxygen and then the furnace was heated up to 850 °C with the rate of 5 °C/min under argon and kept at 850 °C for half an hour. At 780 °C the Argon was switched to H_2S. After half an hour of sulfidization, the furnace was cooled down to ambient temperature by the rate of 5 °C/min under argon and the black product was collected and was subjected to further characterizations.

Li-Intercalation and Exfoliation of CRNWs. Intercalation and exfoliation of $Nb_{1-x}W_xS_2$ were done in two steps. The first step was to intercalate the sulfide with lithium by soaking 1.3 mg of the sulfide in 1.5 mL n-butyllithium (n-BuLi) and 10 mL of hexane under argon for 72 h at 100 °C under constant stirring. For this purpose, the coin rolls were dispersed in hexane and sonicated for 30 min and then n-BuLi was added and the solution was sonicated for 15 min. before starting the reflux, the setup was pre-flushed with argon for at least 30 min. After 72 h the intercalated sample was centrifuged (9000 rpm, 10 minutes) and washed with hexane for three times to remove any unreacted n-BuLi. The intercalated sample was then exfoliated with 20 mL deionized water by ultrasonication for 1 h during which evolution of gas was observed. The product was characterized using TEM, HRTEM, STEM and EDX.

Functionalization of Exfoliated Graphene Sheets. In a typical experimental procedure, 1 mL of as synthesized $Nb_{1-x}W_xS_2$ graphene sheets was taken in a glass vial. To the sheet solution, (100 µl) of 0.1 M NaBH4 was added followed by 50 µl of 25 mM of Gold (III) Chloride solution. The reaction mixture was allowed to stand in room temperature for 15 minutes before washing away unbound gold particles by centrifugation (6000 rpm, 10 minutes). The nanocomposite thus formed was characterized by TEM, HRTEM, STEM and EDX.

6.2.3. Material Characterization

Electron Microscopy. Transmission electron microscopy as well as electron diffraction was performed on a Phillips EM-420 equipped with a slow scan CCD detector (1k x 1k) and a LaB_6 electron gun operated with an acceleration voltage of 120 kV. Transmission electron

microscopy (TEM) images were processed with the Gnu Image Manipulation Program GIMP Version 2.6.8 or with Image J Version 1.43u. High resolution (HR) images were taken with a Philips FEI TECNAI F30 ST electron microscope (field-emission gun, 300 kV extraction voltages) equipped with an Oxford EDX (energy-dispersive X-ray) spectrometer with a Si/Li detector and an ultrathin window for elemental analysis and a STEM detector. STEM images were collected by a high angular annular dark field detector. TEM samples were prepared by dispersion of the sample in ethanol and drop casting on 300 mesh carbon coated copper grids.

Scanning Force Microscopy (SFM). Samples for SFM investigations were prepared by drop casting: One drop from 100 µl syringe of sample solution was deposited on a freshly cleaved mica surface. Subsequently the mica sheet was transferred into a high vacuum chamber and dried overnight. All SFM images were recorded at room temperature under ambient conditions with a commercial SFM (Multimode, NanoscopeIIIa controller, Veeco, California, USA) in tapping mode. This instrument was equipped with a piezoelectric scanner allowing a maximum x,y-scan size of 17 µm and a maximum z-extension of 3.9 µm. Silicon cantilevers (OMCL-AC240TS (Olympus), 240 µm long, 30 µm wide, 2.8 µm thick) with an integrated tip, a nominal spring constant of 2 N/m and 42 N/m, a tip radius <10 nm and nominal resonance frequencies of 70 kHz and 300 kHz were plasma cleaned prior to used. Typically the tip was scanned at velocities from 0.5 to 1 µm s^{-1}. For all samples we have recorded the topography and phase contrast images. Raw data were modified by applying the first order ‘‘flatten’’ filter in order to achieve scan lines at the same average height and average tilt.

Dynamic Light Scattering.

Sample Preparation. A stock solution of $Nb_{1-x}W_xS_2$ (0.05 mg/mL) was diluted with a NaCl solution to give concentrations of [NaCl] = 10 mM and [$Nb_{1-x}W_xS_2$] = 0.007 mg/mL. The addition of NaCl aided screening of eventual electrostatic interactions of the graphene sheets. 2 mL of the solution were filtered through a Millex-GS-filter unit (0.22 µm pore size) into a cylindrical quartz-cuvette (Hellma, 20 mm diameter).

Light Scattering Setup. The DLS setup consisted of an ALV-5000 correlator, equipped with an ALV/SP125 goniometer and avalanche photodiode detector. An argon ion laser (λ= 514.5 nm, *P*= 500 mW output power) served as a coherent light source. Measurements were carried out at 30, 50, 70, 90, 110, 130 and 150° and at a temperature of 20°C. 5 runs were recorded at every angle to increase the signal to noise ratio.

Dynamic Coefficient Measurements for the Fresh Sample. The field correlation g_1 (τ) could be well fitted with the CUMULANT series expansion

$$g_1(\tau) = a + b \cdot exp\left(-\frac{\tau}{c}\right) \cdot [1 + d \cdot \tau^2]$$

With *a* representing the baseline (which was substracted before fitting) and b representing the amplitude. *C*, being the decay time of the correlation function, yields the z-average diffusion coefficient $<D>_{z,app.} = 1/\ c{\cdot}q^2$ of the particles, with q as the scattering vector $q = 4\pi n \sin(\theta/2)/\ \lambda_0$. In cases of a polydisperse sample consisting of larger particles (d > λ/20), a measurement performed at a finite angle only yields an apparent diffusion coefficient $<D>_{z,app}$, which increases with the scattering angle due to the contribution of the particle form factor. The true z-average $<D>_{z.}$ can then be obtained by extrapolating towards $\theta = q^2 = 0$.

Finally, the second cumulant *d* is a quantitative measure for the width of the diffusion coefficient distribution and hence for the dispersity of the sample

$$\sigma^2(D) = (\Delta D)^2 = \langle D^2 \rangle - \langle D \rangle^2 = \frac{2d}{q^4}$$

By applying Stokes-law of diffusion, which assumes spherically shaped particles, the hydrodynamic radius can be obtained from the diffusion coefficient

$$\langle R_H \rangle = \frac{kT}{6\pi\eta\langle D \rangle}$$

Linear extrapolation to $\theta = q^2 = 0$ in Figure 5a yields a z-averaged diffusion coefficient of $<D>_z = 3.20 \times 10^{-8}$ cm^2/s and a hydrodynamic radius of R_H= 67 nm.

The second coefficient of the CUMLANT series expansion represents a quantitative measure for the dispersity of the sample. At 90°, a standard deviation of σ (D) = 0.856 x10^{-8} cm^2/s was obtained, which was used to plot the distribution curve, based on a standard deviation.

Diffusion Coefficient Measurements after 4 Weeks. From the same stock solution ([$Nb_{1-x}W_xS_2$]= 0.05 mg/mL), a new sample was prepared ([NaCl] =10 mM, [$Nb_{1-x}W_xS_2$]= 0.01 mg/mL) 4 weeks later shows the diffusion coefficients measured at different angles and via linear extrapolation a diffusion coefficient of $<D>_z = 2.67{\cdot}10^{-8}$ cm^2/s and a hydrodynamic radius of R_H= 80 nm are obtained. Using the second cumulant, a standard deviation of σ = 1.03·10^{-8} cm^2/s was calculated. The particles increased in size and also the diffusion coefficient distribution became broader, which indicates aggregation over time.

6.3. Results and Discussion

In this communication we report the synthesis and *in situ* functionalization of $Nb_{1-x}W_xS_2$, a new graphene-type inorganic material. The synthetic strategy used for the fabrication of single

layer $Nb_{1-x}W_xS_2$ nanosheets involves lithium (Li) intercalation of $Nb_{1-x}W_xS_2$ coin-roll nanowires (CRNWs) in the first step, followed by exfoliation with water. The obtained $Nb_{1-x}W_xS_2$ nanosheets, displaying a coin-like morphology were *in situ* functionalized with gold nanoparticles [15]. The $Nb_{1-x}W_xS_2$ nanosheets and $Au@Nb_{1-x}W_xS_2$ nanocomposites were characterized by high resolution electron microscopy (HRTEM), energy-dispersive X-ray spectroscopy (EDX), scanning transmission electron microscopy (STEM), dynamic light scattering (DLS) and scanning force microscopy (SFM). Scheme 6-1 depicts the stepwise synthetic route for the preparation of $Nb_{1-x}W_xS_2$ nanosheets and the subsequent *in situ* functionalization with gold nanoparticles. In the first step, Li ions (from n-BuLi) were intercalated between the CRNWs layers leading to an increase in the interlayer space. The second step involves the exfoliation of the Li intercalated-CRNWs in aqueous environment, resulting in '*peeling off*' of the 2D single layers from the stacked CRNWs. The obtained $Nb_{1-x}W_xS_2$ nanosheets were further functionalized (in situ) with gold nanoparticles [16, 17].

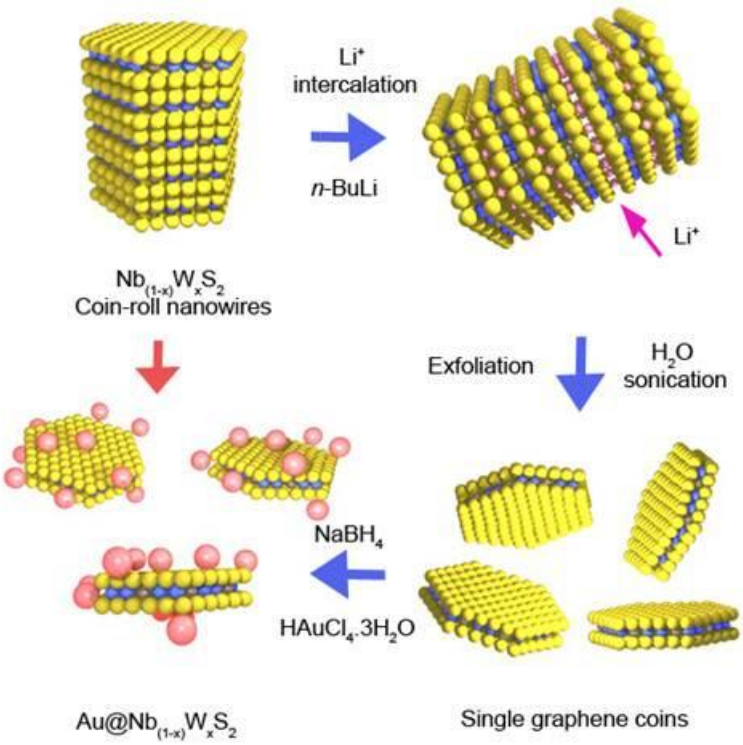

Scheme 6-1. Synthesis of the $Nb_{1-x}W_xS_2$ nanosheets and the *in situ* functionalization with gold nanoparticles.

The $Nb_{1-x}W_xS_2$ CRNWs were synthesized as reported by Yella *et al.* [18] by reductive sulfidization of $Nb_2O_5@W_{18}O_{49}$ core-shell metal oxide nanowires. After sulfidization, the as-synthesized $Nb_{1-x}W_xS_2$ CRNWs contain a mixture of tungsten-rich niobium sulfide and niobium-rich tungsten sulfide. The stacked structure of the as-synthesized $Nb_{1-x}W_xS_2$ CRNWs is shown in Figure 6-1a.

Subsequently, the $Nb_{1-x}W_xS_2$ CRNWs were treated with *n*-BuLi (in hexane) followed by refluxing for 72 h under inert gas atmosphere. Li intercalation between the layers leads to interlayer separation and concomitant weakening of the van der Waals interactions that warrant the structural integrity of the CRNWs. Upon exposition to water, this integrity is compromised leading ultimately to the formation of $Nb_{1-x}W_xS_2$ nanosheets with a coin-like morphology. The $Nb_{1-x}W_xS_2$ nanosheets were further investigated by HRTEM and EDX. HRTEM and EDX show the presence of the phase $Nb_{0.225}W_{0.775}S_2$ with lattice parameters a = 0.31956, b = 0.31956, and c = 1.2226 nm ($P6_3/mmc$) [19]. However, STEM and EDX investigations revealed a locally different elemental composition from almost no Nb up to W:Nb = 1:1 (Figure 6-2a and b).

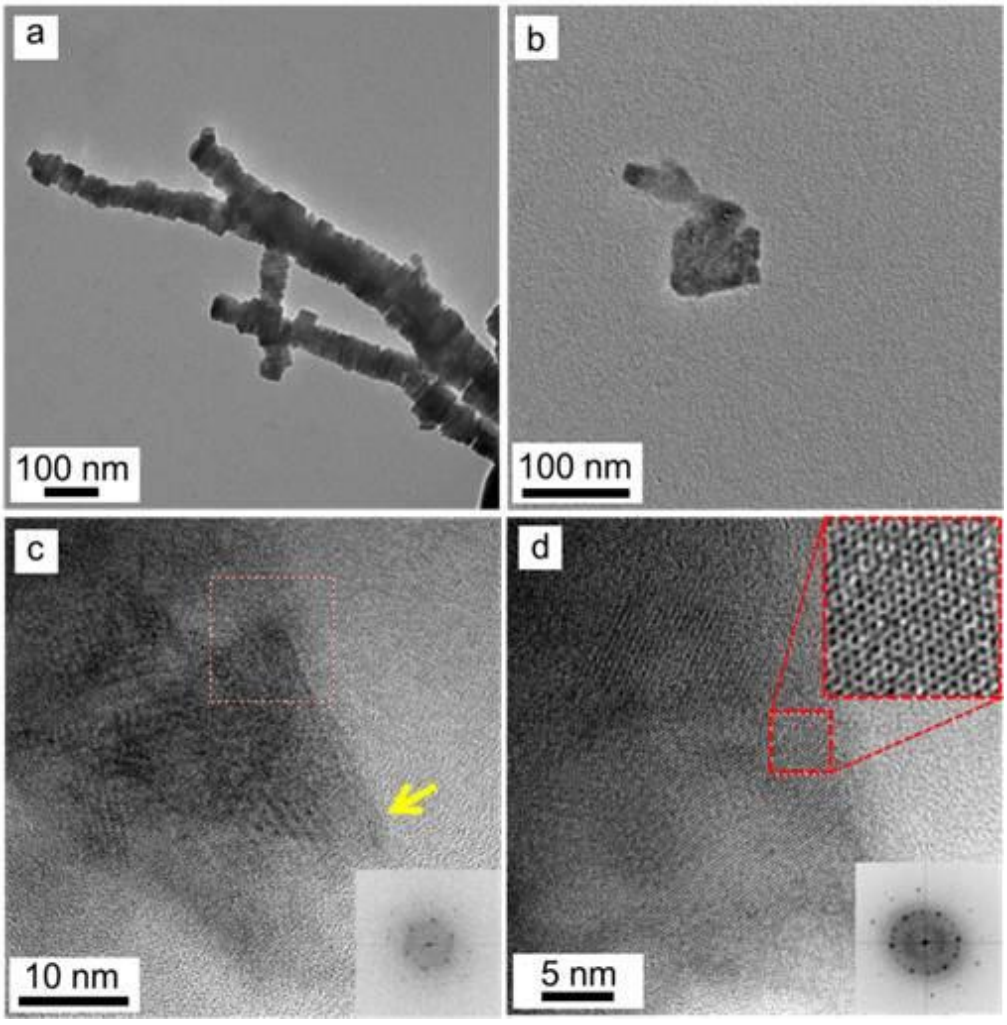

Figure 6-1. (a) TEM images of the as-synthesized $Nb_{1-x}W_xS_2$ coin-roll nanowires (CRNWs), (b) TEM overview of an exfoliated $Nb_{1-x}W_xS_2$ nanosheet, (c) Correspondent high-resolution TEM image of a triangular $Nb_{1-x}W_xS_2$ nanosheet after exfoliation (Inset: Fast Fourier Transform (FFT) on the selected area), (d) The high-resolution image of a nanosheet and the refinement image showing the hexagonal structure formed by Nb, W and S atoms at the rim of the sheet (Inset: FFT on the selected area).

Figure 6-1b shows a TEM image of the $Nb_{1-x}W_xS_2$ nanosheets after exfoliation in water. A HRTEM image of a free-standing nanosheet is provided in Figure 6-1c. A HRTEM image at the edge (shown by a yellow arrow) is shown in Figure 6-3a. Figure 6-1d shows a nanosheet at its rim, highlighting the hexagonal structure of the single $Nb_{1-x}W_xS_2$ nanosheet (top right inset in Figure 6-1d). In some places, there is a superposition of a few sheets with turbostratic disorder. The interlayer separation of approx. 1.2 nm is compatible with a second stage intercalation phase (marked by parallel lines in Figure 6-3b).

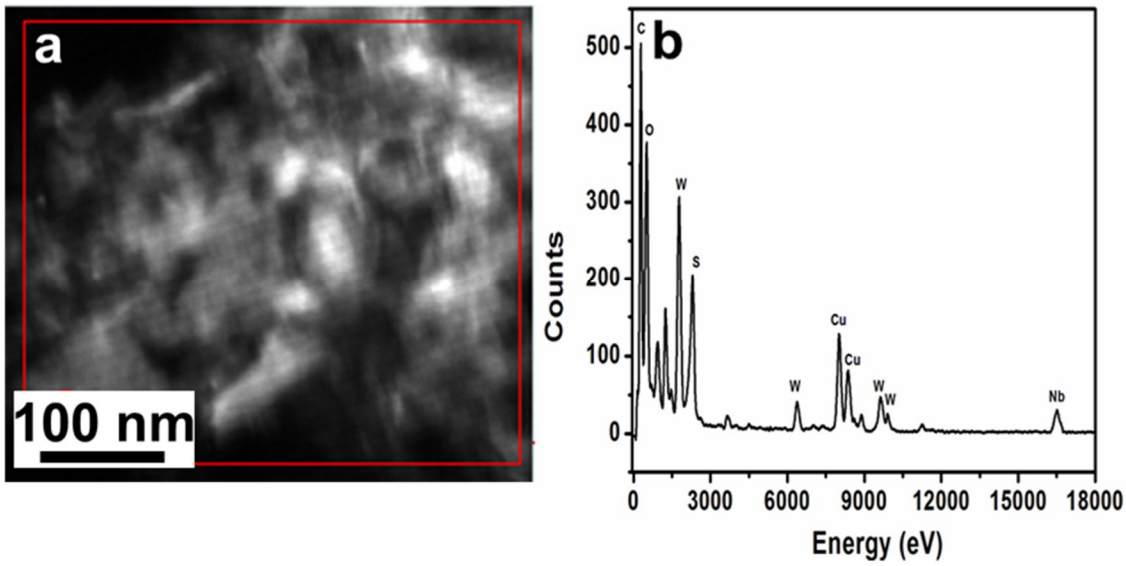

Figure 6-2. (a) STEM image of the exfoliated coin rolls (b) EDX spectrum of the selected area.

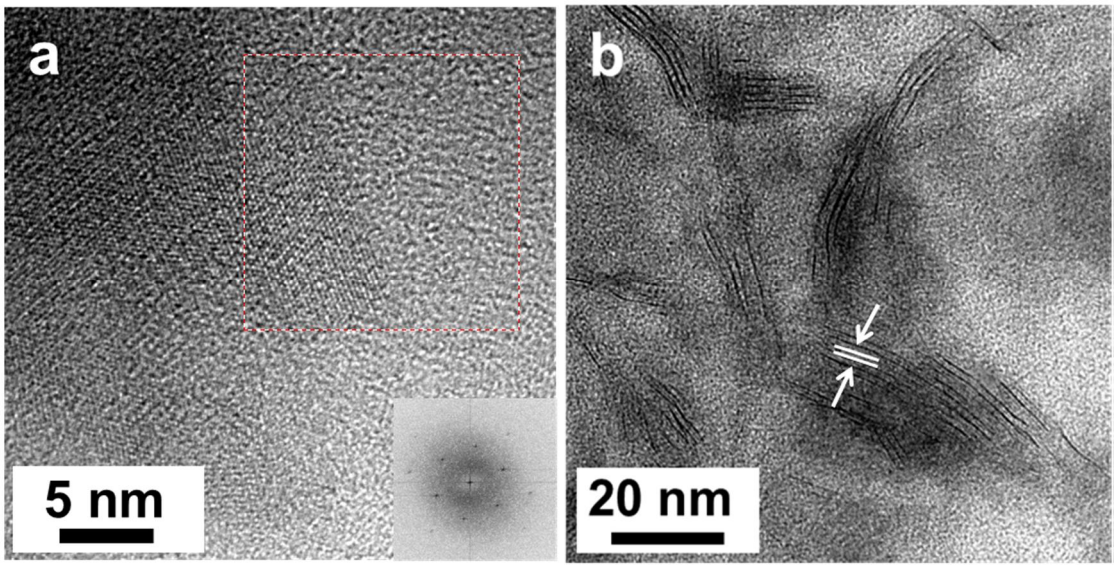

Figure 6-3. (a) HRTEM image on the rim of a sheet (Inset: FFT on the selected area). (b) HRTEM image of few-layer sheets with an interlayer distance of ~ 12Å.

Representative SFM images and the corresponding height profiles of the as-synthesized $Nb_{1-x}W_xS_2$ CRNWs and the nanosheets after exfoliation are shown in Figure 6-4. The SFM height image (Figure 6-4a) of as-synthesized $Nb_{1-x}W_xS_2$ CRNWs and the corresponding height profile (Figure 6-4b) confirm that CRNWs have a thickness of approximately 100 nm. The height images and corresponding height profile of the exfoliated nanosheets (Figure 6-4c and d) show a maximum height of approx. 2.81 nm (marked by a red arrow) which corresponds to sheets consisting of 3-4 layers. The thickness of the sheets at the edges is around 0.69 nm as marked by the blue arrow indicating the presence of a single layer. This result was confirmed by analyzing the height profiles of different structures (Figure 6-5). The data obtained from height profiles from different spots indicated that our sample contains nanosheets ranging from a single layer to 3-4 layers of $Nb_{1-x}W_xS_2$.

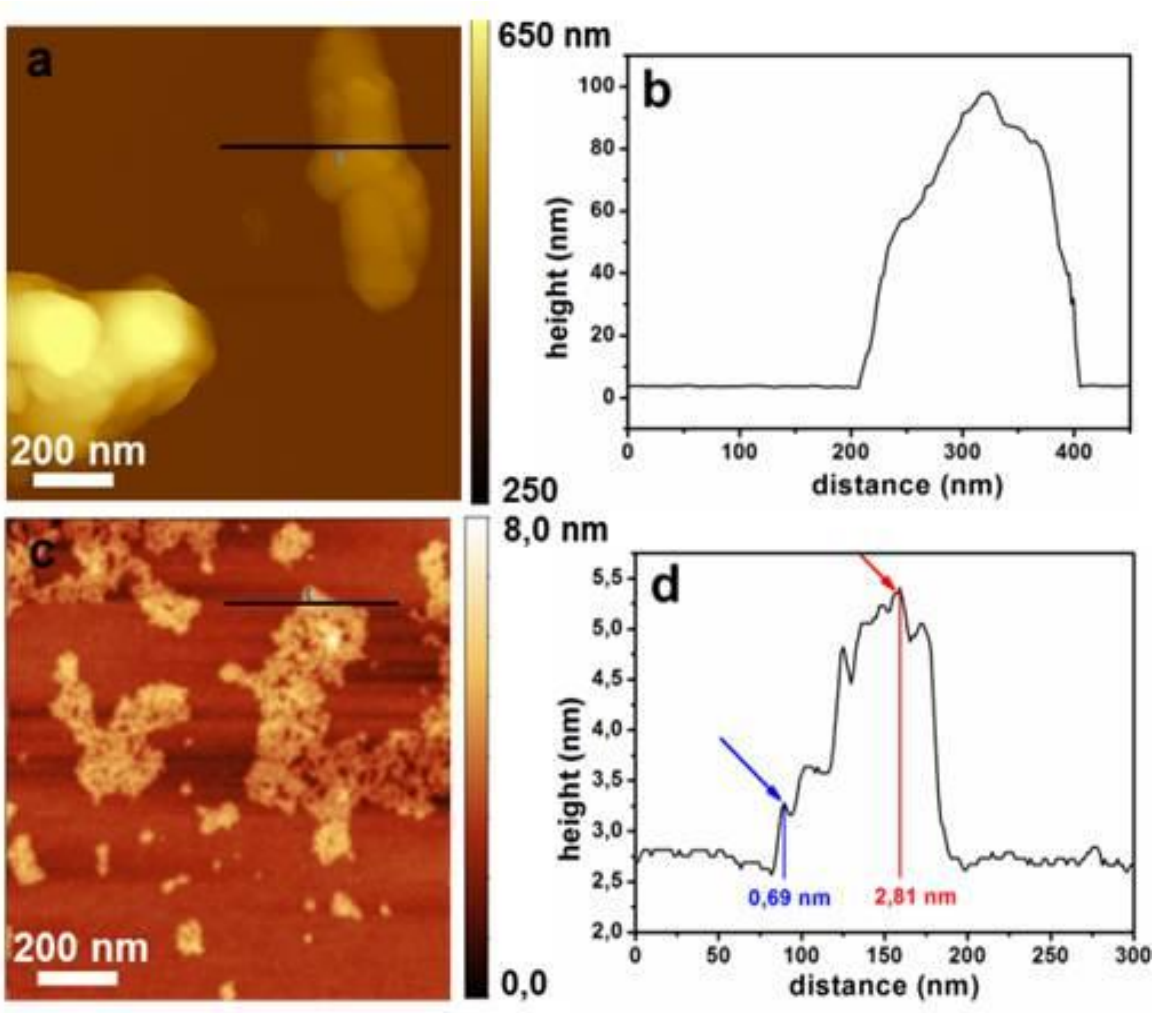

Figure 6-4. (a) SFM image of the as-synthesized $Nb_{1-x}W_xS_2$ CRNWs. (b) Height profile of the naked CRNWs. (c) SFM overview image of as-synthesized $Nb_{1-x}W_xS_2$ nanosheets after exfoliation. (d) Height profile of the graphene sheets showing around 2.7 nm measuring up to 3-4 nanosheets.

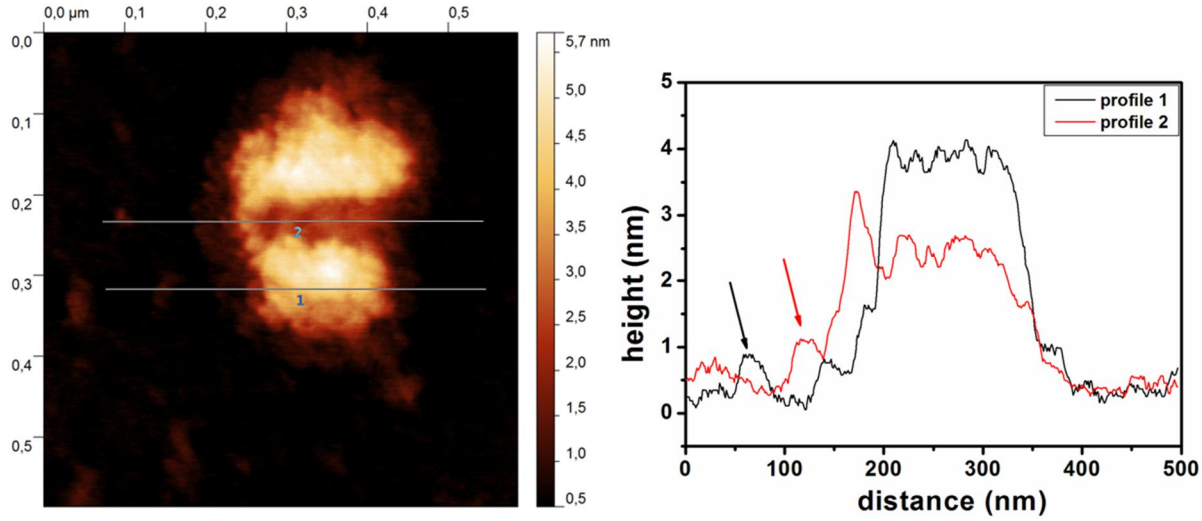

Figure 6-5. SFM height image and corresponding profiles at various points to show the height of sheets.

The pristine coin roll nanowires of $Nb_{1-x}W_xS_2$ precipitate in water or some other solvents even in a couple of hours, but the exfoliated sheets are stable against aggregation over a period of months (Figure 6-6). However, the "true" stability of the exfoliated sheets and their aggregation behavior could be understood with the aid of dynamic light scattering (DLS). DLS studies were carried out to determine the size of the $Nb_{1-x}W_xS_2$ nanosheets in aqueous solution (7 µg/mL). Measurements were carried out at scattering angles of 30, 50, 70, 90, 110, 130 and 150° and at 20°C. Five runs were recorded at each angle to increase the signal to noise ratio. At all angles, the field correlation $g_1(\tau)$ showed a monomodal decay process.

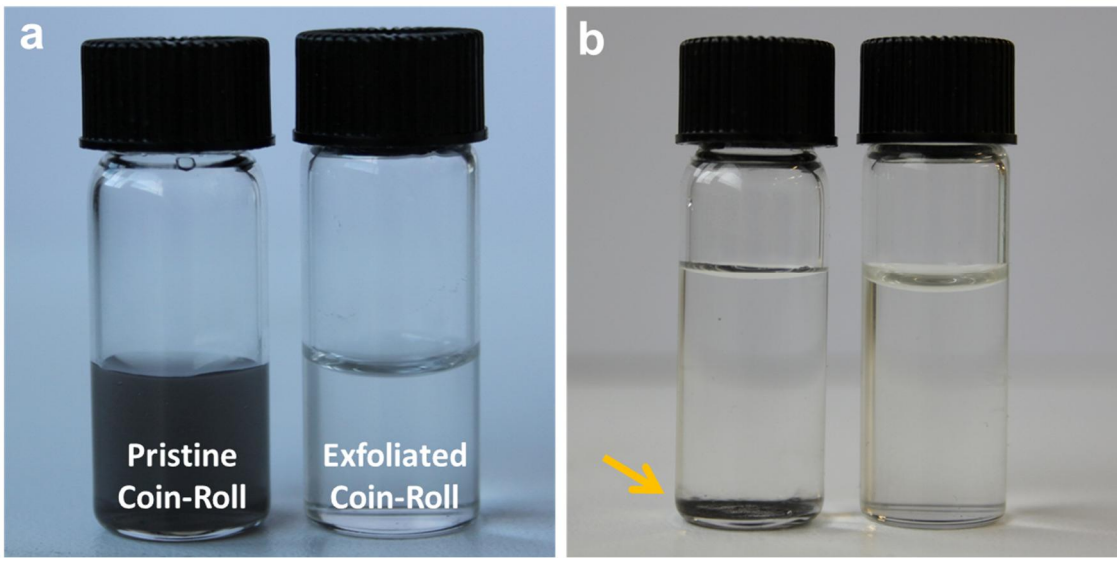

Figure 6-6. (a) Digital micrograph of the coin-roll nanowires before (left) and after (right) exfoliation. (b) The same samples after 3 hours, showing the sedimentation of the dispersed pristine coin-roll nanowires.

Figure 6-7 shows the measured diffusion coefficients at different angles. Linear extrapolation to $q^2=0$ (corresponding to $\theta = 0$) in Figure 6-8a yields a z-averaged diffusion coefficient of $\langle D \rangle_z = 3.20\times10^{-8}$ cm^2/s and a hydrodynamic radius of $R_H = 67$ nm. This indicates a size of the $Nb_{1-x}W_xS_2$ nanosheets to be considerably larger than determined by TEM. While comparing particle sizes obtained via TEM and DLS, one has to consider that TEM statistics yield a number average of the particle diameter, whereas an inverse *z*-average is obtained from a DLS measurement. The latter strongly pronounces the contribution from the larger particle fractions to the mean value. Furthermore, the q^2 dependence of the diffusion coefficients indicates some polydispersity of the sample which could originate from the uncontrolled intercalation-exfoliation of the sheets and the lack of uniformity in the shape and size of the pristine coin rolls (as observed by SFM). The second coefficient of the CUMLANT series expansion represents a quantitative measure for the dispersity of the sample. At 90°, a standard deviation of σ (D) = 0.856×10^{-8} cm^2/s was obtained, which was used to plot the distribution curve, based on a standard deviation. A repetition of the experiment 4 weeks later (the diffusion coefficients of the nanosheets recorded at different angels is shown in Figure 6-8) revealed an averaged hydrodynamic radius of about 80 nm (Figure 6-7b) indicating that the $Nb_{1-x}W_xS_2$ nanosheets slightly agglomerate with time, although the solution is still transparent against visible light. As in all the experiments deionized water was used for the exfoliation, the observed agglomeration is not due to any additional component such as

ions and could be explained by the intrinsic affinity of the layers to "restack" and by solvophobic interactions.

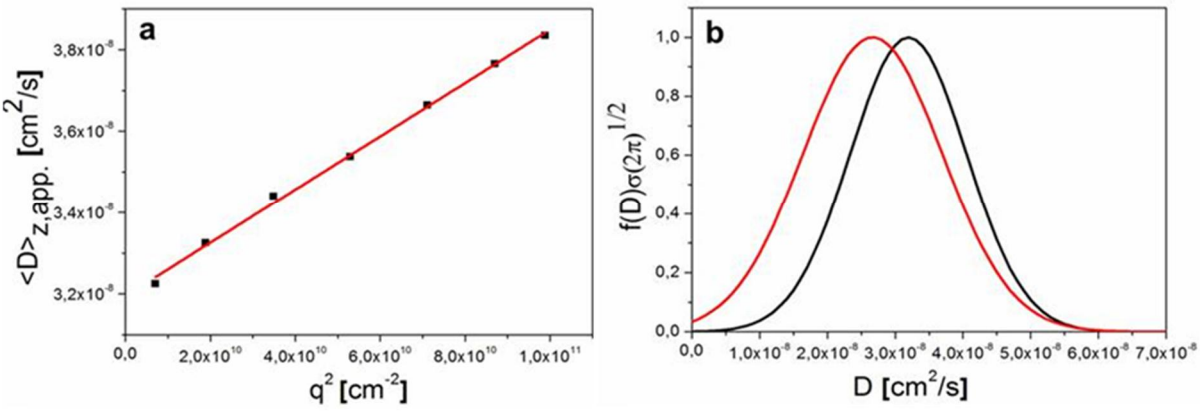

Figure 6-7. (a) Diffusion coefficients of the $Nb_{1-x}W_xS_2$ nanosheets (7 μg/mL in distilled water) recorded at different angles (30, 50, 70, 90, 110, 130 and 150°), (b) Comparison of the diffusion coefficient distribution for the freshly exfoliated $Nb_{1-x}W_xS_2$ nanosheets (7 μg/mL in distilled water) (black line) and the same sample re-measured four weeks later (red line).

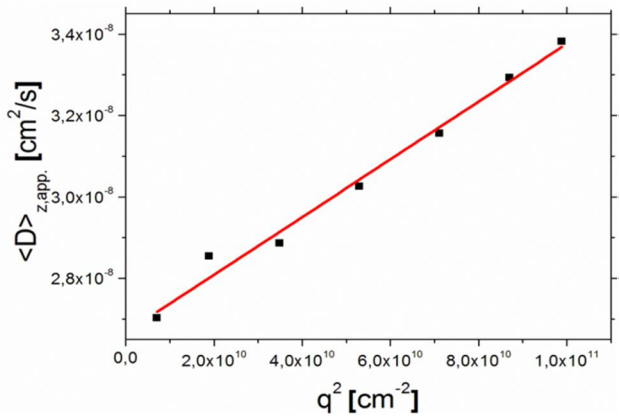

Figure 6-8. Diffusion coefficients of the graphene sheets recorded at different angles after 4 weeks.

The Au@$Nb_{1-x}W_xS_2$ nanocomposite was obtained by *in situ* functionalization of freshly exfoliated $Nb_{1-x}W_xS_2$ nanosheets by mixing them with an $AuCl_4^-$ solution (25 mM) in the presence of a reducing agent ($NaBH_4$). The freshly generated Au nanoparticles (size ~ 4 nm) aggregated on the surface of the $Nb_{1-x}W_xS_2$ nanosheets (Figure 6-9a and b). Gold, being the softest metal (Pearson Hardness 3.5 eV)[17] binds strongly to the sulfur atoms of the $Nb_{1-x}W_xS_2$ nanosheets.[18] The HRTEM image shows the *in situ* generated Au nanoparticles to be bound to the bulk and preferably to the edges of the $Nb_{1-x}W_xS_2$ nanosheets. STEM analysis confirms the presence of Au nanoparticles as Au appears lighter in contrast compared to $Nb_{1-x}W_xS_2$. (Figure 6-9c) The corresponding elemental analysis shows an additional peak of

Au (compared with EDX spectra of $Nb_{1-x}W_xS_2$ nanosheets, Figure 6-2b) confirming the presence and formation of the Au nanoparticles (Figure 6-9d).

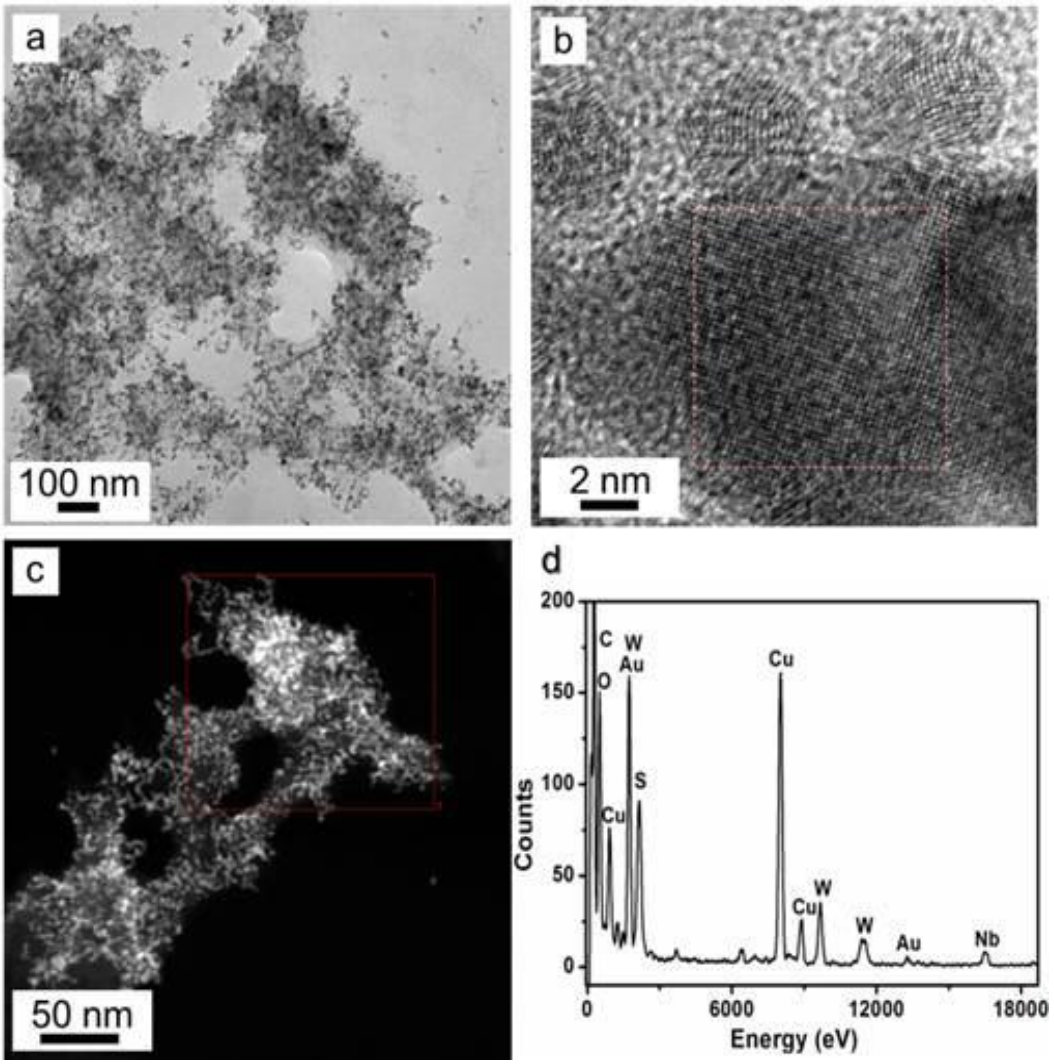

Figure 6-9. (a) TEM overview image showing a Au@$Nb_{1-x}W_xS_2$ nanocomposite. (b) HRTEM image of the nanocomposite showing the presence of Au nanoparticles (ø ~4nm) bound to the rim of the $Nb_{1-x}W_xS_2$ nanosheets. (c) STEM image of the nanocomposite, where the light signals in lighter areas correspond to the Au nanoparticles and the darker signals to the $Nb_{1-x}W_xS_2$ nanosheets. (d) EDX spectrum of the Au@$Nb_{1-x}W_xS_2$ nanocomposites indicating the presence of Nb, W, S and Au.

6.4. Conclusions

In summary, we have demonstrated a general scheme for the selective functionalization of $Nb_{1-x}W_xS_2$ nanosheets using gold nanoparticles. Graphene-type $Nb_{1-x}W_xS_2$ was synthesized by Li intercalation and subsequent exfoliation of "coin roll nanowires" (CRNWs). The $Nb_{1-x}W_xS_2$ nanosheets are not only dispersible in water and polar solvents, they are stable for several weeks and can be functionalized with chalcophilic agents such as gold nanoparticles which in turn may be functionalized with a variety of ligands imparting e.g. optical or catalytic properties to the $Nb_{1-x}W_xS_2$ nanosheets [20,21]. The sheets were characterized by TEM, demonstrating the presence of gold nanoparticles distributed preferably at the sheet rims (where coordinatively unsaturated sulfur atoms expose their donor orbitals). Our results identify exfoliated $Nb_{1-x}W_xS_2$ nanosheets as a more reactive structure than chalcogenide nanotubes and nested fullerenes [15, 17]. The current results are encouraging to elucidate the expected role of conductive $Nb_{1-x}W_xS_2$ nanosheets for building devices such as hybrid graphene-type sensors.

6.5. References

[1] (a) A. K. Geim, *Science*, **2009**, *324*, 1530; (b) M. J. Allen, V. C. Tung, R. B. Kaner, *Chem. Rev.*, **2010**, *110*, 132; (c) A. A. Balandin, *Nat. Mater.*, **2011**, *10*, 569; (d) O. V. Yazyev, S. G. Louie, *Nat. Mater.*, **2010**, *9*, 806.

[2] (a) K. S. Novoselov, A. K. Geim, S. V. Morozov, D. Jiang, Y. Zhang, S. V. Dubonos, I. V. Grigorieva, A. A. Firsov, *Science*, **2004**, *306*, 666; (b) A. K. Geim, K. S. Novoselov, *Nat. Mater.*, **2007**, *6*, 183.

[3] A. Nag, K. Raidongia, K. P. S. S. Hembram, R. Datta, U. V. Waghmare, C. N. R. Rao, *ACS Nano*, **2010**, *4*, 1539.

[4] (a) K. S. Novoselov, D. Jiang, F. Schedin, T. J. Booth, V. V. Khotkevich, S. V. Morozov, A. K. Geim, *Proc. Natl. Acad. Sci. USA*, **2005**, *102*, 10451; (b) P. Joensen, R. F. Frindt, S. R. Morrison, *Mater. Res. Bull*,. **1986**, *21*, 457.

[5] (a) B. K. Miremadi, S. R. Morrison, *J. Appl. Phys.*, **1988**, *63*, 4970; (b) D. Yang, R. F. Frindt, *J. Phys. Chem. Solids*, **1996**, *57*, 1113.

[6] Y. Zhao, R. Hughes, Z. Su, W. Zhou, D. H. Gregory, *Angew. Chem. Int. Ed.*, **2011**, *50*, 10397.

[7] R. Tenne, L. Margulis, M. Genut, G. Hodes, *Nature*, **1992**, *360*, 444.

[8] (a) F. Hulliger, *Structural Chemistry of the Layer-Type Phases* (Ed.: F. Levy), Reidel, Dordrecht, 1976; (b) A. Katz, M. Redlich, L. Rapoport, H. D. Wagner, R. Tenne, *Tribol. Lett.*, **2006**, *21*, 135; (c) J. Tannous, F. Dassenoy, B. Vacher, T. Le Mogne, A. Bruhacs, W. Tremel, *Tribol. Lett.*, **2011**, *41*, 55.

[9] J. Jang, S. Jeong, B. Park, J. Seo, J. Cheon, M.-C.Kim, E. Sim, Y. Oh, S. Nam, *J. Am. Chem. Soc.*, **2011**, *133*, 7636.

[10] A. R. Adini, M. Redlich, R. Tenne, *J. Mater. Chem.*, **2011**, *21*, 15121.

[11] K. F. Mak, C. Lee, J. Hone, J. Shan, T. F. Heinz, *Phys. Rev.Lett.*, **2010**, *105*, 136805.

[12] A. Splendiani, L. Sun, Y. Zhang, T. Li, J. Kim, C.-Y. Chim, G. Galli, F. Wang, *Nano Lett.*, **2010**, *10*, 1271.

[13] (a) B. Radisavljevic, A. Radenovic, J. Brivio, V. Giacometti, A. Kis, *Nat. Nanotech.*, **2011**, *6*, 147. (b) B. Radisavljevic, M. B. Whitwick, A. Kis, *ACS Nano*, **2011**, **5**, 9934.

[14] (a) J. N. Coleman, M. Lotya, A. O'Neill, S. D. Bergin, P. J. King, U. Khan, K. Young, A. Gaucher, S. De, R. J. Smith, I. V. Shvets, S. K. Arora, G. Stanton, H-Y. Kim, K. Lee, G. T. Kim, G. S. Duesberg, T. Hallam, J. J. Boland, J. J. Wang, J. F. Donegan, J. C. Grunlan, G. Moriatry, A. Shmeliov, R. J. Nicholls, J. M. Perkins, E. M. Grieveson,

K. Theuwissen, D. W. McComb, P. D. Nellist, V. Nicolosi, *Science*, **2011**, *331*, 568; (b) H. S. S. R. Matte, A. Gomati, A. K. Manna, D. J. Late, R. Datta, S. K. Pati, C. N. R. Rao, *Angew. Chem. Int. Ed.*, **2010**, *49*, 4059.

[15] J. K. Sahoo, M. N. Tahir, A. Yella, T. D. Schladt, E. Mugnaioli, U. Kolb, W. Tremel, *Angew. Chem. Int. Ed.*, 2010, *49*, 7578; *Angew. Chem.*, **2010**, *120*, 7741.

[16] (a) R. G. Pearson, *J. Am. Chem.Soc.*, 1963, *85*, 3533; (b) R. G. Pearson, *J. Chem. Educ.*, **1968**, *45*, 581; (c) R. G. Pearson, *J. Chem. Educ.*, **1968**, *45*, 643; (d) R. G. Parr, R. G. Pearson, *J. Am. Chem. Soc.*, **1983**, *105*, 7512; (e) R. G. Pearson, *Chemical Hardness.Applications from Molecules to Solids*, Wiley-VCH, Weinheim 1997.

[17] (a) J. K. Sahoo, M. N. Tahir, F. Hoshyargar, B. Nakhjavan, R. Bran-scheid, U. Kolb, W. Tremel, *Angew. Chem.*, **2011**, *123*, 12479; *Angew. Chem.Int. Ed.*, **2011**, *50*, 12271. (b) J. K. Sahoo, M. N. Tahir, A. Yella, T. D. Schladt, S. Pfeifer. B. Nakhjavan, E. Mugnaioli, U. Kolb, W. Tremel, *Chem. Mater.*, **2011**, *23*, 3534.

[18] A. Yella, E. Mugnaioli, M. Panthöfer, U. Kolb, W. Tremel, *Angew. Chem.*, **2010**, *122*, 3373; *Angew. Chem. Int. Ed.*, **2010**, *49*, 3301.

[19] P. Villars, K. Cenzual, Pearson's Crystal data – Crystal Structure Database for Inorganic Compounds (on CD-Rom), Release 2009/10, ASM International, Materials Park, Ohio, USA.

[20] (a) T. D. Schladt, M. I. Shukoor, M. N. Tahir, F. Natalio, K. Schneider, I. Ament, J. Becker, F. Jochum, S. Weber, P. Theato, L. M. Schreiber, C. Sönnichsen, H. C. Schröder, W. E. G. Müller, W. Tremel, *Angew. Chem.*, **2010**, *122*, 4068; *Angew. Chem. Int. Ed.*, **2010**, *49*, 3976. (b) M. Bartz, R.Seshadri, J. Küther, W. Knoll, W. Tremel, *Angew. Chem.*, **1998**, *110*, 2646; *Angew. Chem. Int. Ed.*, **1998**, *37*, 2466.

[21] C. Shahar, R. Levi, S. R. Cohen, R. Tenne, *J. Phys. Chem. Lett.*, **2010**, *1*, 540.

CONCLUSIONS AND OUTLOOK

In this work, effective approaches to synthesize **0D**, **1D** and **2D** nanostructures of layered TMDs were adapted and optimized and probable mechanism for the formation of these nanostructures were proposed. The synthetic protocols involve (i) a modified method being a combination of the MOCVD and the chemical vapor transport approach, (ii) sulfidization of oxide precursors and (iii) intercalation/exfoliation.

The characterization of the samples was carried out using X-ray diffraction (XRD), scanning electron microscopy (SEM) combined with focused ion beam (FIB), atomic force microscopy (AFM), scanning tunneling electron microscopy (STEM) and transmission electron microscopy (TEM) in conjunction with energy dispersive X-ray spectroscopy (EDX), dynamic light scattering (DLS) and automated electron diffraction tomography (ADT).

It has been already shown that iodine enhances the solid state diffusion of the used precursors in the induction furnace where the solid state diffusion can be excluded as the rate determining step by the help of fast heating/cooling. Here, in this work, iodine was used as a mineralizing agent to find out if it could enhance the solid state diffusion in case of slow heating/cooling. For this purpose, a horizontal tube furnace was used instead of an induction furnace to study the Mo-S-I system. In this case, the solid state diffusion leads to the formation of MoS_2 nanotube bundles emanating from a common origin in a radial manner. It was observed that the iodine content of the precursors led to the formation of a surface film that made the molybdenum and sulfur atoms mobile by isothermal chemical transport. The enhanced mobility of the Mo and S constituents aided in the formation of point defects within the MoS_2 layers that are needed to scroll up the inherently instable 2D MoS_2 sheets. In the resulting tubular structures the number of dangling bonds and thus the total surface energy are reduced. The diffusion flow of the volatile reaction intermediates from the inside to the outside of the microsphere precursor particles led to the formation of nanotube bundles that proved stable upon sonification. When the reaction was performed in the absence of iodine, no nanotubes were formed. This observation proves the role of iodine in the formation of MoS_2 nanotube bundles. Therefore, this new and easy method could be a potential route towards the synthesis of chalcogenide nanoparticles. Following the successful synthesis of MoS_2 nanotube bundles, this method was extended to synthesize other chacogenide nanoparticles. Using the same protocol and by changing the molecular precursor from $Mo(CO)_6$ to $W(CO)_6$, WS_2 nested fullerenes were obtained. The formation of 2H-WS_2@IF-WS_2 intermediate nanostructures was studied using different electron microscopy techniques. Here, the growth of fullerenes was monitored by taking TEM snapshots of intermediate products. For the first time, the internal volume of the nested

fullerenes was studied using a combined SEM/FIB technique. Cutting cross sections of core-shell nanoparticles revealed the internal structure of these nanostructures. Lamellar reaction intermediates were found occluded in the fullerene particles. The role of the reaction and annealing temperature on the composition and morphology of the final product were also investigated. As the nested fullerenes obtained by this method are larger than the IF-WS_2 obtained by conventional MOCVD, it is anticipated that the shells are less stiff and more vulnerable toward deflections when an external force is applied onto them. The strength of the WS_2 shell was measured using contact-mode AFM. According to the force curve obtained from intermittent contact AFM, the rupture on the surface of IF-WS_2 particles happens at 25 nN which agrees well with the values already reported for MoS_2 bubbles (18 nN). Further work in this project includes the extension of this new synthesis approach to other layer-structure metal chalcogenides.

In the next part of the project, a novel route to synthesize tungsten sulfide nanotubes in a massive quantity was developed. According to this method, tungsten oxide nanowires were synthesized by a solvothermal synthetic approach using tungsten chloride and different alcohols as solvent. The effect of reaction temperature and concentration of starting precursor on the morphpology and dispersity was described. The oxide nanostructures were observed to serve as versatile precursor material to form defect-rich multiwalled tungsten sulfide nanotubes with a good virtue to be functionalized by controlled reductive sulfidization by H_2S. The nanotubes were suspendiable in various solvents over days. Owing to the massive defect densityon the surface of these nanotubes, they were successfully functionalized by metal and metal oxide nanoparticles such as gold, manganese oxide and Pt@Fe_3O_4 Janus nanoparticles. The enhanced functionalization of these nanotubes opens new fields of application for this class of materials such as electronic devices, hybrid composites, thin films and solar cell applications.

As observed in the case of spherical nanoparticles (which form fullerenes and the other onion-like morphologies) and also nanowires and high aspect ratio nanorods (which form nanotubes), the direct transfer of the initial morphology to the end product during the sulfidization has been discussed for a long time. In order to investigate whether the preservation of the morphology applies for any other structures, the oxide to sulfide conversion method could be utilized to convert WO_3 low aspect ratio nanorods to corresponding sulfides. The ADT technique was used to investigate the effect of the oxide precursor crystal structure on the final morphology of the sulfide product. In this case, nested tungsten sulfide “nanocoffins” were obtained by sulfidization of solvothermally-derived

tungsten trioxide (hydrate) nanorods at 850°C. The data acquired by ADT on the tungsten oxide precursor showed that the rods mostly grow along *00l* and the hydratation affects (100) and (010), which are normally the larger facets. However, WO_3 and $WO_3 \cdot {}^1/_3H_2O$ crystallites are orientated the same. Thus, the growth of $WO_3 \cdot {}^1/_3H_2O$ on WO_3 seems to be a topotactical reaction. It was also demonstrated that at the initial steps of sulfidization, $WO_3 \cdot {}^1/_3H_2O$ transforms into h-WO_3 whose surface allows for the epitaxial induction of WS_2. Initially formed platelets of WS_2 exhibit a preferred orientation with respect to the nanorod surface. Finally, the individual layers of WS_2 coalesce to form seamless closed shells. In conclusion, a cascade of topotactic reactions leads to epitactic induction and thus the formation of closed rectangular boxes made from hexagonal layers.

Since the walls of the nanotubes and fullerene-like nanoparticles are chemically very inert and quite impermeable, the diffusion of the guest moiety depends on the availability of weak links, *i.e.* surface defects or open tips at the nanotube edges. However, when the nanotube is not fully crystalline and its walls are made of small crystallites, the fast intercalation becomes possible leading to rapid charge/discharge cycles and high capacity for the guest atoms.

The restriction of convenient layered chalcogenide nanoparticles toward the intercalation could be overwhelmed by selecting an appropriate intercalation host. Attempts to intercalate the $Nb_{1-x}W_xS_2$ coin-roll nanowires (CRNWs) using n-BuLi in an inert atmosphere for 72 hrs at 100°C and further exfoliation of the Li-intercalated CRNWs using H_2O led to the formation of graphene-type sheets of $Nb_{1-x}W_xS_2$. In fact, the miniaturization of 2D structures by lateral confinements, made them potential candidates not only for modulation of electron-transport phenomena, but also enhanced their host capabilities arising from the enlarged surface area and improved diffusion properties upon the intercalation of guest molecules due to the finite lateral size and enhanced open-edge morphology of the 2D nanosheets. The stabilization of the as-synthesized graphene-type sheets in the aquatic solution and other solvents could be enhanced by *in situ* functionalization of the graphene-type sheets using gold nanoparticles. It is shown that the exfoliated nanosheets have more reactive structures compared to chalcogenide nanotubes and nested fullerenes which can lead to their potential application in building devices such as hybrid graphene-type sensors.

APPENDIX

8.1. List of Figures

curving of the layers along the segments. (g,h) Periodic alternation along the stack.

Figure 1-20. (a) and (b) the TEM images of MoS_2 layers obtained by Methods 2 and 3, (c) is the high resolution TEM image of layered MoS_2 from Method 3, (d) and (e) images of WS_2 layers from Methods 1 and 2 respectively. The bends in the layers can arise from defects.

Figure 1-21. Raman spectra of (a) bulk MoS_2 and MoS_2 layers obtained by Methods 1 and 2 and (b) bulk WS_2 and WS_2 layers obtained by Methods 1 and 2.

Figure 1-22. TEM images of few-layer BN prepared with (a) 1:12, (b) 1:24, and (c) 1:48 boric acid/urea mixture.

Figure 1-23. TEM of nanosheets. (A to C) Low resolution TEM images of flakes of BN, MoS_2, and WS_2, respectively. (D to F) High-resolution TEM images of BN, MoS_2 and WS_2 monolayers. Insets: Fast Fourier transforms of the images. (G to I) Butterworth-filtered images of sections of the images in (D) to (F).

Figure 1-24. Deposition of nanosheets onto surfaces. (A and B) An SEM and an AFM image of MoS_2 flakes deposited on SiO_2 by spraying. (C) A Raman map of the same region. (D) Typical Raman spectrum of an individual flake. The Raman map plots the integral of the spectrum between 390 and 410 cm^{-1}. (E to G) A very thin flake, a multilayer, and a cluster of aggregated multilayers. The dashed line in (E) has been inserted to illustrate the straightness of the flake edge. (H and I) SEM and AFM images of an individual flake. (J) An STM image of an individual flake. The flakes in (I) and (J) have heights of 5 and 10 nm, respectively (25). (K) An SEM image of a MoS_2 flake on Si/SiO_2 with electrodes deposited on top. (L) Drain-source conductance (GDS) as a function of gate voltage (VGS) for the flake shown in (K). VDS is the applied drain-source voltage.

Figure 1-25. TEM image of an individual IF-WS_2 nanoparticle partially intercalated with Rubiduim atoms. Due to the significant strain, the intercalation which is indicated by lattice expansion (0.64 nm) of the closed shells is limited to the outermost 15 layers. The innermost layers of the nanoparticle exhibit the regular lattice spacing (0.62 nm).

Figure 2-1. (a) Powder X-ray diffraction (XRD) pattern of the primary product obtained from the reaction of $Mo(CO)_6$, I_2, and H_2S/Ar at 550 ºC; the red trace line indicates I_2 (PDF-2 File Card No. 43-0304). (b) Powder XRD pattern of the

primary product after annealing at 850 ºC; the red line corresponds to 2H-MoS_2 (PDF-2 File Card No. 37-1492), and the asterisks indicate reflections from $Mo_2S_5I_3$ (PDF-2 File Card No. 39-0717).

Figure 2-2. SEM images of the product obtained after the first step. (a) Overview SEM image of the product. The 2D branched nanostructures are marked by a red rectangle. (b) Magnified image of the microspheres showing branched MoS_2 nanowires emanating from the center. (c) High-resolution (HR) image showing the branched nanowires in a top view. (d) HR image of the branched 2D nanostructures with open-ended tips and porous walls.

Figure 2-3. TEM images of the product obtained after the first step. (a) a single bundle which is stable after long ultrasonic treatment, (b) 2D branched nanostructures after the ultrasonic treatment.

Figure 2-4. TEM images of the product obtained after annealing ((a) TEM image of a single microsphere, showing the nanotubes emanating from the center in a radial manner; (b) TEM image showing the ends of the microsphere with a peapod-like structure). HRTEM images of the product obtained after annealing ((c) closed-end nanotube, (d) openended nanotube, (e) peapod-like structure with nested fullerenes inside the nanotubes, and (f) a “burst” fullerene under the beam).

Figure 2-5. SEM images of the product obtained after the annealing at 850°C in Ar for 1 h. (a) SEM Overview of MoS_2 nanotube bundle aggregates and (b) HRSEM image of a single nanotube bundle.

Figure 2-6. (a) TEM overview image of the product obtained at the annealing temperature of 750°C. (b), (c) HRTEM image of as-synthesized nanotubes (The tubes were found to have more defects compared to those obtained at 850°C), (d) TEM image of the product obtained at the annealing temperature of 800°C and (e) 900°C.

Figure 2-7. TEM image of the product obtained at the reaction temperature of (a) 350°C and (b), (c) 450°C.

Figure 2-8. SEM images of the product obtained without using iodine in the process ((a) overview SEM image showing that the product consists of spherical particles; (b) magnified image showing that the surface is not uniform but rather consists of smaller aggregates).

Figure 2-9. TEM image of the product obtained after omitting iodine as precursor.

8.2. List of Schemes and Tables

8.3. Supplementary Information

Chapter 3

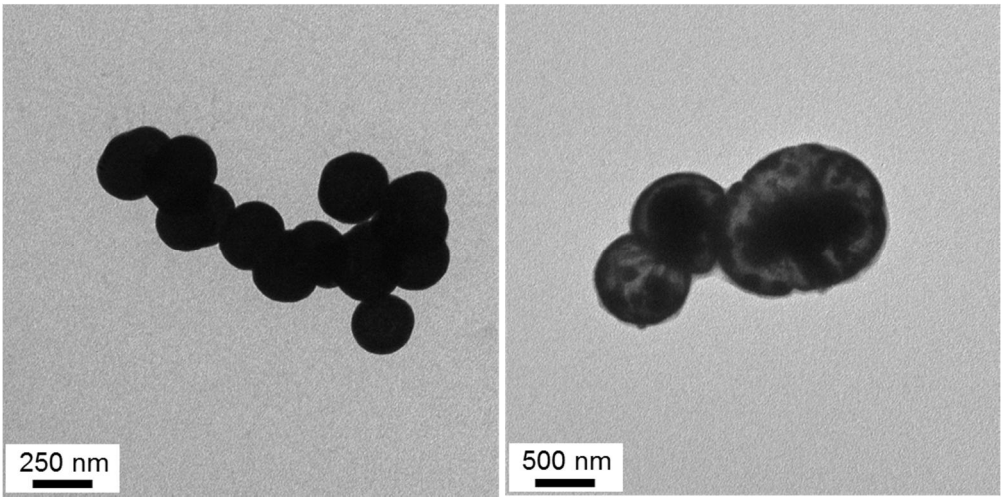

Figure S1. TEM overview image of the product obtained at the annealing temperature of 750°C.

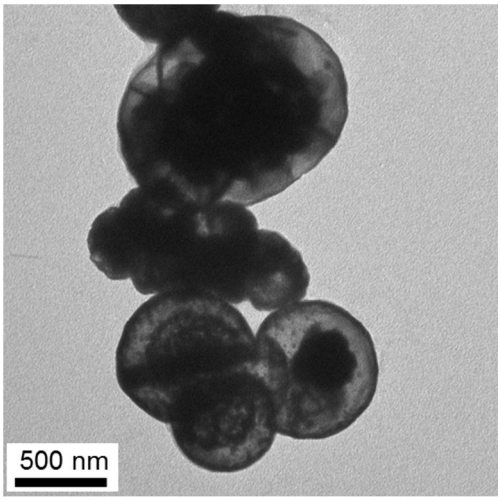

Figure S2. TEM overview image of the product obtained at the annealing temperature of 800°C.

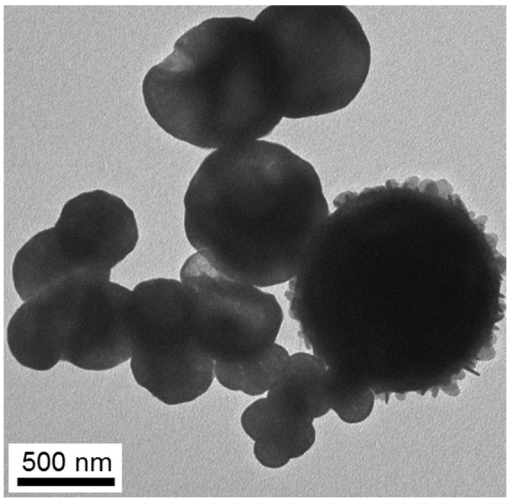

Figure S3. TEM overview image of the product obtained at the annealing temperature of 900°C.

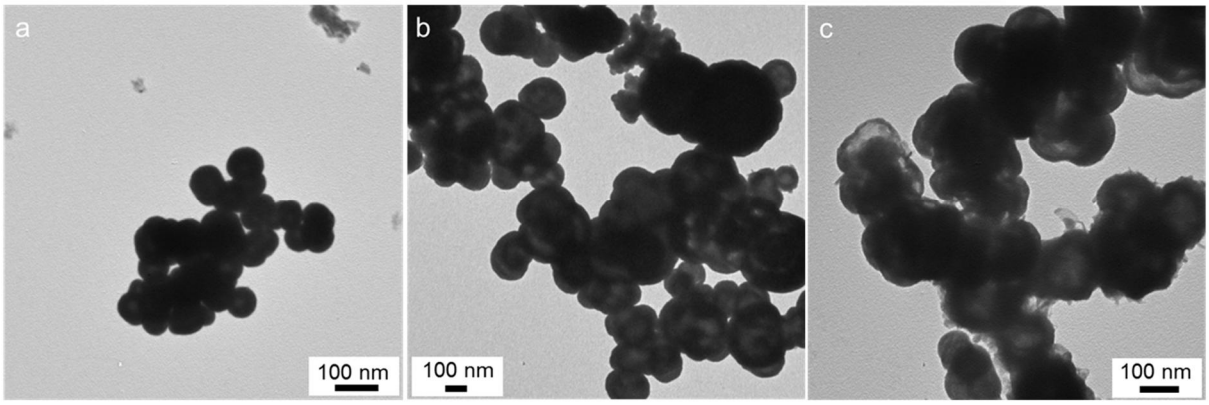

Figure S4. TEM images of the products obtained from reactions at (a) 300°C, (b) 400°C and (c) 500°C.

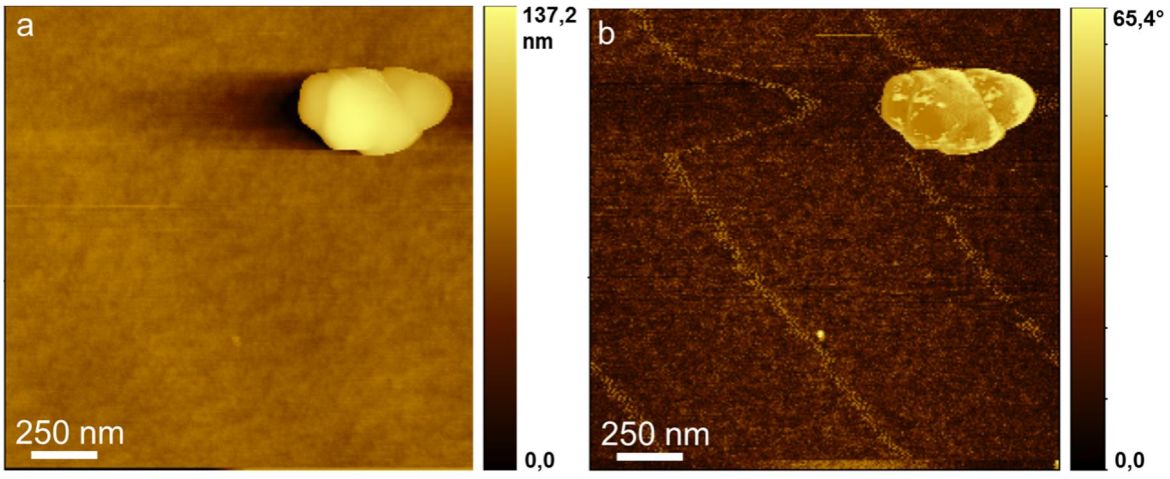

Figure S5. (a) AFM height profile of as-synthesized IF-WS_2 particle. (b) Phase profile of IF-WS_2 particles.